ABSTRACT

Title of dissertation: GLOBAL SCALE AEROSOL PROPERTIES: IMPLICATIONS FOR SURFACE SHORTWAVE RADIATION BUDGET

Hongqing Liu, Doctor of Philosophy, 2005

Dissertation directed by: Professor, Rachel T. Pinker, Department of Atmospheric and Oceanic Science

Aerosols are known to affect the shortwave radiation budget of the Earth-atmosphere system. Using truncated Empirical Orthogonal Functions (EOF) fitting, we derive monthly mean aerosol optical depth (AOD) at 0.55 μm using information from: the Goddard Global Ozone Chemistry Aerosol Radiation and Transport (GOCART) model; the MODerate resolution Imaging Spectro-radiometer (MODIS); and the AErosol RObotic NETwork (AERONET). The single scattering albedo, the asymmetry parameter and the normalized extinction coefficient over the solar spectrum are estimated from GOCART data, MODIS Ångström exponent and AERONET almucantar retrievals.

The University of Maryland (UMD) Global Energy and Water Cycle Experiment (GEWEX) shortwave Surface Radiation Budget (SRB) model is updated to allow the treatment of complex aerosol properties. The modified model is implemented with the International Satellite Cloud Climatology Project (ISCCP) D1

for a one year period. From the evaluation of the improvements against ground measurements we find that the bias in retrieved AOD at 0.55 μm is reduced from 0.20 to 0.05. The overall bias in the estimated surface SW fluxes is reduced by about 7 Wm^{-2} for the total irradiance and 11 and 4 Wm^{-2} for the direct and diffuse parts, respectively. The new version of the UMD SRB model has now the capability to address the issue of aerosol direct radiative effects. Annually averaged global clear-sky direct radiative aerosol forcing is estimated to be -1.31 Wm^{-2} at the top of atmosphere and -2.71 Wm^{-2} at the surface. This indicates that the effect of aerosols on the SW energy absorption is comparable with their effect on the reflection at the TOA. At regional scales, aerosol effects can be much larger. In a case study preformed at a sub-Sahel site in Africa, the depletion of the daily surface irradiance can be as large as 120 Wm^{-2}. Compared with other methods used to estimate aerosol direct effects, the advantage of our scheme is that it preserves closure with TOA satellite measurements. With anticipated progresses in aerosol research and satellite observations, the UMD SRB model has the potential to address aerosol radiative effects in a realistic and coherent way.

GLOBAL SCALE AEROSOL PROPERTIES: IMPLICATIONS FOR SURFACE SHORTWAVE RADIATION BUDGET

By

Hongqing Liu

Dissertation submitted to the Faculty of the Graduate School of the
University of Maryland, College Park, in partial fulfillment
of the requirements for the degree of
Doctor of Philosophy
2005

Advisory Committee:
Professor Rachel T. Pinker, Chair
Dr. Mian Chin
Professor Russell R. Dickerson
Professor Ralph Dubayah, Dean's Representative
Professor Robert Hudson
Professor Eugenia Kalnay
Professor Owen E. Thompson

Acknowledgements

I am deeply indebted to my advisor, Professor Rachel T. Pinker, for her constant guidance, support and patience. Without her help, this work would not be possible. I would also like to express my sincere thanks to Dr. Istvan Laszlo and Dr. Mian Chin for their invaluable advice and many fruitful discussions; to Dr. Joaquim Ballabrera for his inspiring class that was of great help to this study; to all faculty members for their excellent lectures and instruction; and to all the committee members for their guidance.

Support by the NASA Earth System Science Fellowship grant NGT530450 and research grants awarded to Professor Rachel T. Pinker are greatly appreciated.

Finally, I would like to express my deepest gratitude for the constant support, understanding and love that I received from my family.

Table of Contents

This Table of Contents is automatically generated by MS Word, linked to the Heading formats used within the Chapter text.

List of Tables

List of Figures

Chapter 1: Introduction

Quantifying shortwave radiation budgets has been a key issue in climate, biological productivity and solar power research. Satellites play an important role in this activity since large-scale measurements of reflected radiance can be used for estimating the solar radiation budget at the top of atmosphere (TOA) [*Jacobowitz et al.*, 1984; *Schiffer and Rossow*, 1983; 1985; *Barkstrom*, 1984; *Wielicki et al.*, 1996]. Satellites are also valuable for providing information about the atmosphere and the surface which in turn is needed for linking the TOA and surface budgets.

Over last several decades, numerous satellite-based algorithms have been developed to infer the surface radiation budget [*Tarpley*, 1979; *Gautier et al*.,1980; *Diak and Gautier* 1982, *Moser and Raschke,* 1984; *Raschke et al*., 1987; *Dedieu et al*., 1987; *Darnell et al.,* 1988; 1992; *Gupta,* 1989; *Stuhlmann et al*., 1990; *Bishop and Rossow,* 1991; *Pinker and Laszlo*, 1992; *Li et al.,* 1993a; *Breon et al*., 1994; *Rossow and Zhang*; 1995; *Zhang et al.;* 1995; *Gautier and Landsfeld,* 1997; and *Cebalos et al.,* 2004]. However, estimation of surface SW radiation budgets from satellites remains a challenge due to the spatial and temporal variations associated with certain atmospheric components and surface properties. Of particular interest to this thesis are atmospheric aerosols.

Aerosols have a largely uncertain effect on the radiation balance [*Intergovernmental Panel on Climate Change (IPCC)*, 2001]. Natural as well as anthropogenic aerosols affect the global radiation balance directly and indirectly. The direct effects are attributable to scattering and absorption of radiation with a subsequent influence on the planetary albedo and surface radiative fluxes [*Coakley et*

al., 1983; *Charlson et al*., 1992; *Kiehl and Briegleb*, 1993; *Boucher and Anderson*, 1995; *Schwartz,* 1996]. Examples of indirect effects are: possible changes of the number and size of cloud droplets [*Twomey*, 1977; *Twomey et al*., 1984; *Coakley et al*., 1987] or effects on precipitation efficiency [*Albrecht,* 1989]. Reduction in cloud cover caused by solar absorption in haze layers has been considered as a semi-direct effect [*Hansen et al*., 1997; *Ackerman et al*., 2000]. The potential of aerososls to increase reflected solar radiation and the resultant offset of greenhouse gas warming has raised concern in the climate and radiation research communities [*Charlson et al.,* 1992; *Kiehl and Briegleb*, 1993; *Boucher and Anderson*, 1995; *Schwartz*, 1996; *Twomey,* 1977; *Albrecht*, 1989; *Hansen et al*., 1997; *Ackerman et al*., 2000]. Recent observations revealed a significant decrease in surface solar heating due to the presence of absorbing aerosols, which might slow down the hydrological cycle and affect atmospheric dynamics [*Satheesh and Ramanathan*, 2000; *Russell et al.*, 1999; *Bush and Valero*, 2003]. In view of their significant surface cooling effect and the lack of their adequate consideration in previous satellite-based algorithms, there is a need to account for such effects to improve estimation methods of surface SW fluxes. Specifically, there is a need in improved global scale information on aerosol concentrations and their radiative properties, as well as in flexible and efficient inference schemes that incorporate aerosol variability.

Background information about ambient aerosols and satellite algorithms of surface SW flux estimation is introduced in Chapter 2. Sensitivity tests on direct surface effects of aerosols and their impact on the relationship between TOA and surface radiation budgets are performed in Chapter 3. Global monthly mean aerosol

properties are derived using information from improved satellite retrievals of specifically designed space borne sensors; global chemical transport model simulations; and ground observing networks. A detailed explanation will be presented in Chapter 4. University of Maryland (UMD) Global Energy and Water Cycle Experiment (GEWEX) shortwave surface radiation budget (SRB) model is expanded to adapt to the improved information and to allow a more comprehensive consideration of aerosol direct radiative effects. Updates to the model clear-sky aerosol scheme are introduced in Chapter 5. The updated model is implemented with ISCCP data for one year period. Simulation results are evaluated against ground measurements. Aerosol direct radiative effects are assessed and compared with available results. Summary and discussion is presented in Chapter 6.

In what follows, aerosol radiative effects refer to clear sky direct effects only. Scattering and absorption of aerosols under cloudy conditions and interaction between aerosols and clouds are not investigated in this study. Flux density or irradiance (Wm^{-2}) is frequently termed "flux".

Chapter 2: Background

2.1 Characterization of aerosol radiative properties

There is considerable evidence that the concentration of aerosols in the troposphere has increased over the last 150 years due to human activity [*Fischer et al.,* 1998; *Lavanchy et al.,* 1999, IPCC, 2001], and may increase further as developing countries grow in population and industrialization. However, large uncertainties remain in the determination of aerosol effects due to the complexities associated with their properties and difficulties related to measurements and simulations.

2.1.1 Aerosol radiative properties

Ambient aerosols can be efficient scatters and absorbers of SW radiation. Their representation in radiative transfer models is complicated due to the fact that multiple parameters are needed for a "radiatively complete" description of their properties. Generally, three parameters/functions are the fundamental inputs to radiative transfer models:

1) *Aeorosol optical depth* (τ): an extensive state parameter associated with aerosol concentration. Total extinction of the incoming solar radiation can be specified by τ using Beer-Bouguer-Lambert's law:

$$F_{ext} = 1 - F_0 e^{(-\tau)} \qquad (2.1)$$

Spectral variation of τ is usually characterized by Ångström exponent (α), which describes the slope of $\log\tau$ versus $\log\lambda$:

$$\alpha = -\frac{\log(\tau_1) - \log(\tau_2)}{\log(\lambda_1) - \log(\lambda_2)} \qquad (2.2)$$

2) *Single scattering albedo* (ω_0): defined as the ratio of scattering optical depth to total optical depth (scattering plus absorption).

$$\omega_0 = \frac{\tau_{sca}}{\tau_{sca} + \tau_{abs}} \qquad (2.3)$$

It determines the partitioning of the aerosol solar extinction into scattering and absorption; value of 1 corresponds to conservative scattering and 0 to complete absorption.

3) *Scattering phase function*: describes the angular distribution of scattered radiation. Usually, asymmetry parameter (g), the first moment of the phase function, is employed to characterize the aerosol scattering properties in flux calculations due to the extensive use in the two-stream radiative transfer schemes [*Meador and Weaver*, 1980]; and explicit incorporation in the Henyey-Greenstein function [*Henyey and Greenstein*, 1941], which is an acceptable approximation of aerosol phase function [*Hansen*, 1969]. This parameter gives a measure of the anisotropy of the scattering with 0 for isotropic and 1 for total forward scattering. The asymmetry parameter and single scattering albedo are regarded as intensive state parameters which are independent on the amount of aerosol present.

Further complexity results from spatial, temporal and spectral variability associated with these parameters. Based on multi-year AERONET Sun photometer measurements, *Holben et al.* [2001] identified a large variation in aerosol optical depth (AOD) and its wavelength dependence (Ångström exponent) over a wide range

of aerosol regimes. To illustrate the variation in the other two aerosol parameters, we created scatter plots of ω_0 versus g at four wavelengths (0.44, 0.67, 0.87 and 1.02 μm) as shown in Figure 2.1. Data used are more than 6000 instantaneous almucantar retrievals from the global AERONET network during 1993-2003 [*Dubovik et al.*, 2002]. As evident, variations associated with absorption and scattering properties are widely spread; this hinders an unambiguous classification of ambient aerosols into several radiatively distinctive types and therefore, the limited number of aerosol models usually used in remote sensing retrievals may not be sufficient to describe the complexity of global aerosol properties.

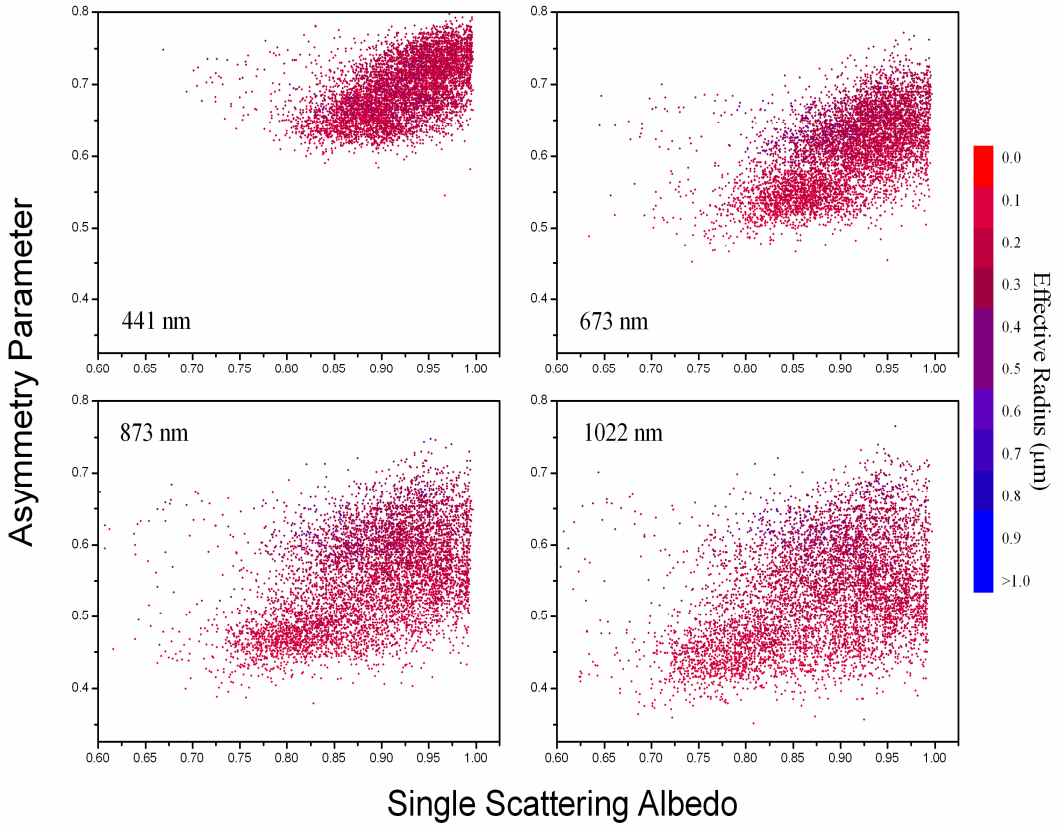

Figure 2.1 Scatter plots of aerosol single scattering albedo and asymmetry parameter for four wavelengths. Data used are derived from AERONET almucantar measurements over more than 10 years (1993-2003).

Numerous efforts have been made to improve our understandings of aerosol properties. Significant progress has been achieved recently by means of computer models, remote sensing and dedicated field observations.

2.1.2 Model simulations

Aerosol radiative characteristics are determined by their microphysical (size distribution and shape) and chemical (composition) properties. Therefore, models have been developed to simulate the physical and chemical processes involved in the short yet complicated aerosol life cycles. Figure 2.2 presents a schematic illustration of the basic mechanisms associated with aerosol formation, evolution, and deposition, as well as the corresponding idealized size distribution. In addition, lateral and vertical transport by the atmospheric circulation; hygroscopic growth by uptake of water vapor; heterogeneous chemistry on particle surface and interactions with other aerosols and clouds need to be incorporated.

Using the simulated aerosol concentrations and microphysical/chemical properties, radiative properties can be estimated based on suitable electromagnetic or optical models [*Mie*, 1908; *Mishchenko et al*., 2000]. Knowledge of the optical constant (spectral complex refractive index) pertinent to each chemical compound and mixing structure are necessary for this process. In summary, a model-based approach is a multidisciplinary and integrative endeavor based on comprehensive understanding of aerosol properties and behavior. Our knowledge is still limited as reflected by the inaccurate description of the non-uniformly distributed aerosol sources and sinks [*Kinne et al.*, 2003]; uncertainties associated with the optical constants [*Haywood et al.*, 2003; *Bond and Bergstrom*, 2004]; lack of reliable theory

for modeling the mixture structure and optical constants of the multi-component aggregates [*Sokolik and Toon*, 1999]; and difficulties related to non-spherical particles [*Mishchenko et al*., 2000]. Systematic measurements of the microphysical, chemical and radiative properties of aerosols are required to improve the highly parameterized schemes and validate the model results at multiple levels.

Present model simulations of the full spectrum of aerosol components (sulfate, organic carbon, black carbon, mineral dust and sea-salt) have been achieved either from Chemical Transport Models (CTMs) driven by off-line meteorological data, or from Global Circulation Models (GCMs) with specific aerosol modules built in. Table 2.1 lists several available global models. Inter-comparison of satellite retrievals with ground observations was reported on by *Penner et al*. [2002] and *Kinne et al*. [2001, 2003, 2005].

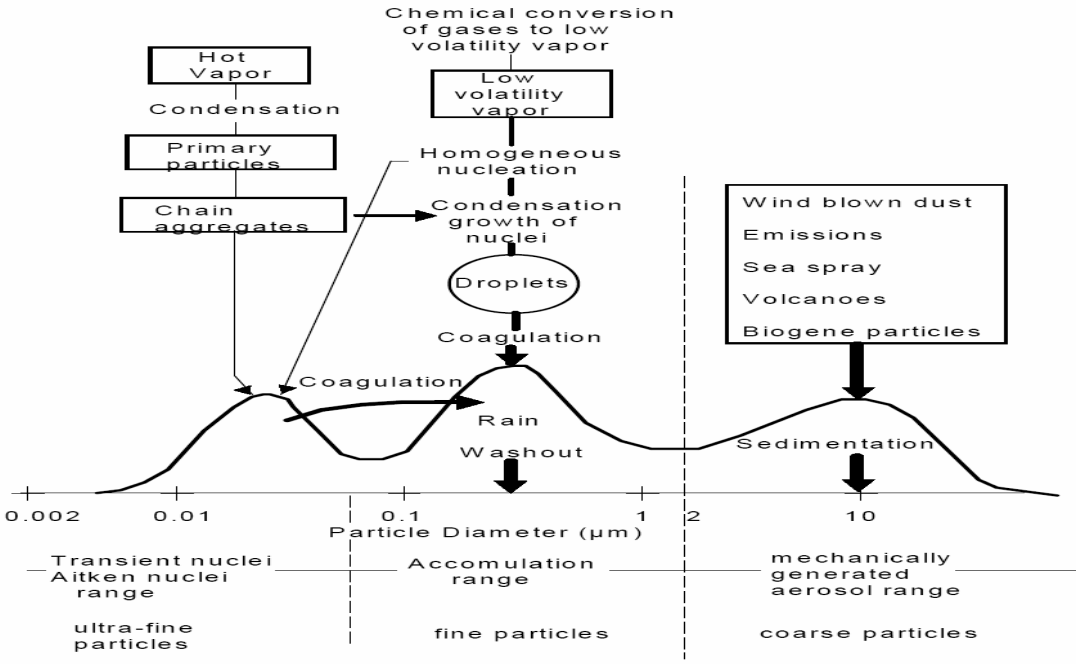

Figure 2.2 Aerosol formation, removal, primary physical/chemical processes and the resulting size distribution (*Whitby and Cantrell* [1975]).

Table 2.1 Available global aerosol models/modules.

Model Acronym	Name/Affiliation	Reference
	CTMs	
GOCART	Global Ozone Chemistry Aerosol Radiation and Transport model NASA Goddard, USA	*Chin et al.* [2000, 2002]*; Ginoux et al.* [2001]
UIO-CTM2	Oslo Chemistry Transport Model 2; Univ. of Oslo, Oslo, Norway	*Myhre et al.* [2003a, 2003b]
SPRINTARS	Spectral Radiation-Transport Model for Aerosol Species Kyushu University, Kyushu, Japan	*Takemura et al.* [2003]
MATCH	Model of Atmospheric Transport and Chemistry NCAR, Boulder, USA	*Fillmore and Collins* [2002]
IMPACT	Integrated Massively Parallel Atmospheric Chemical Transport model Livermore National Laboratory; Livermore, USA	*Chuang et al*. [2001]
TM5	global chemistry Transport Model, version 5 Institute for Marine and Atmospheric Research Utrecht, The Netherlands	*Krol et al*. [2004]
MOZART-GFDL-NCAR (MOZGN)	Model for OZone And Related chemical Tracers with modifications by GFDL and NCAR scientists: Larry Horowitz (NOAA-GFDL, Princeton, NJ), Xuexi Tie (NCAR, Boulder, CO), Jean-Francois Lamarque (NCAR, Boulder, CO), and Paul Ginoux (NOAA_GFDL, Princeton, NJ) NOAA-GFDL&NCAR, USA	*Horowitz et al.* [2003]
	GCMs	
GISS	Goddard Institute for Space Studies (GISS) general circulation model GISS, New York, USA	*Koch et al*. [1999, 2005]
ECHAM5-HAM	European Centre/Hamburg Model MPI-Meterology, Hamburg, Germany	*Stier et al*. [2005]
ECHAM-MADE	Aerosol Dynamics module for Europe DLR Institute of atmospheric physics Oberpfaffenhofen, Wessling, Germany	*Lauer et al*. [2005]
LMDZ-INCA	Laboratoire de Météorologie Dynamique general circulation model (LMDz) and the Interaction with Chemistry and Aerosols (INCA) model Lab Science Climat et de l'Enivonnement (LSCE), Paris, France	*Hauglustaine et al*. [2004]
GCM/CAM	Canadian Aerosol Module Air Quality Research Branch Met Service, Toronto, Canada	*Gong et al.* [2003]
MIRAGE	Model for Integrated Research on Atmospheric Global Exchange Pacific Northwest National Laboratory (PNNL) Richland, USA	*Ghan et al.* [2001a, 2001b, 2001c]
ULAQ-CCM	Universita degli Studi L'Aquila (ULAQ) L'Aquila, Italy	*Pitari et al.* [2000, 2002]

2.1.3 Remote sensing

Given the large variability of aerosol properties, satellites are most suitable for their continuous and large-scale observations. Over the last two decades, numerous satellite sensors have been utilized or designed to retrieve aerosol optical depths [*King et al.*, 1999]. Operational products have been obtained from[1]: AVHRR [*Rao et al*., 1989; *Stowe et al.*, 1997; *Husar et al*., 1997; *Higurashi and Nakajima*, 1999; *Mishchenko et al.*, 1999; *Stowe et al*., 2002; *Ignatov and Nalli,* 2002; *Geogdzhayev et al*., 2002]; TOMS/OMI [*Herman et al*., 1997; *Torres et al.*, 1998, 2002, 2003]; MODIS [*Kaufman et al.,* 1997; *Tanré et al*, 1997; *Remer et al.*, 2005], MISR [*Diner et al.*, 1998; *Martonchik et al.*, 1998, 2002; *Kahn et al.*, 2005] and POLDER [*Déuzé et al.*, 2001]. Similar activity has been extended to other polar-orbiting sensors, such as SeaWiFS [*Gordon and Wang*, 1994], GLI [*Nakajima et al.*, 1998], OCTS [*Nakajima et al.*, 1999], ASTR-2 [*Veefkind et al*., 1998, 1999], VIRS [*Ignatov and Stowe*, 2000], MERIS [*Ramon and Santer*, 2001], AATSR [*Holzer-Popp et al.*, 2002], ETM+ [*Lyapustin et al.*, 2004], as well as to geostationary satellites, such as GOES-8 [*Knapp et al.*, 2002; *Wang et al.*, 2003a, 2003b]. In addition, several new instruments (CNES-PARASOL/POLDER, NASA/CNES-CALIPSO/CALIOP, EUMETSAT-MSG/SEVIRI, NOAA-NPOESS/VIIRS and NOAA-GOES-R/ABI) have been or will be launched. Such enrichment of space platforms and capabilities will open great opportunities to enhance our understanding and description of ambient aerosols.

The principle of satellite retrievals is to relate the observed TOA signals with certain aerosol properties. Common passive path radiance method relies on the

[1] Acronyms are defined in Appendix C.

extraction and interpretation of aerosol contribution from SW spectral/angular reflectance. Major factors affecting retrieval accuracy are:

1) *Calibration*

Inaccurate radiometric calibration will lead to a systematic bias in retrieved aerosol properties. Experiments have shown that variation of one digital count in the AVHRR radiance can cause a relative error of derived AOD as large as 40% over open oceans [*Geogdzhayev et al.*, 2002].

2) *Cloud screening*

In terms of aerosol retrievals, unambiguous identification of cloud-free pixels is a key requirement. Applying a conservative criterion might miss the episodes of thick aerosol plumes, while a less stringent threshold increases the possibility of cloud contamination. New generation of satellite sensors (e.g., MODIS, MISR) have been specially designed to meet these challenges through the incorporation of onboard calibration, expansion of spectral coverage and increase of spatial resolution.

3) *Surface effects*

Radiance detected by a satellite radiometer is a collective quantity consisting of contributions from atmospheric scattering and surface reflection. It is not uncommon that aerosol signal might be a small residual from two large terms; therefore, surface reflectance needs to be estimated at high accuracy before a successful AOD retrieval can be made. *Kaufman et al.* [1997] found that an uncertainty of 0.005-0.01 for surface reflectance can translate to an error as about 0.05-0.1 in the retrieved AOD. Due to the large variation and insufficient knowledge of surface bidirectional

reflectance distribution functions (BRDF), the quality and spatial coverage of aerosol retrievals over land is still limited.

4) *Assumptions associated with aerosol properties*

The TOA aerosol signal is determined by multiple parameters (e.g., τ , ω_0, scattering phase function) and satellite aerosol retrieval is ill-posed in nature: there are more unknowns than equations. As a consequence, retrieved will be the most dominant properties (usually optical depth); remaining parameters need to be assumed at various levels of uncertainty. Algorithms that use a single channel and single angle depend on a complete prescription of aerosol intensive properties [*Stowe et al.*, 1997]; multi-channel and multi-angle measurements could facilitate a dynamical selection or combination of prescribed aerosol models [*Kaufman et al.,* 1997; *Tanré et al*., 1997; *Martonchik et al.*, 1998]. Yet, an increase in the number of observations does not convert to the same number of degrees of freedom. A principal component analysis (PCA) by *Tanré et al.* [1996] illustrates that due to intercorrelation among radiances observed at seven wavelengths (simulated MODIS channels) only one to two parameters of size distribution can be retrieved. Assumptions about aerosol vertical location are also important for remote sensing application at the UV spectrum [*Torres et al.*, 1998]. Sensitivity tests and evaluation of satellite retrievals have demonstrated that inaccurate assumptions on aerosol properties could lead to significant errors in estimation of AOD [*Jeong et al*., 2005; *Levy et al*, 2003, 2005, *Torres et al*., 2005].

Other techniques (e.g., polarimeter [*Déuzé et al.*, 2001]; spaceborne lidar [*Winker et al.*, 2002; *Léon et al*., 2003]) have been explored to augment satellite

capabilities. Studies have been extended to derive other fundamental parameters (e.g., single scattering albedo [*Kaufman et al.*, 2001; *Torres et al.*, 2005; *Chowdhary et al.*, 2005; *Satheesh and Srinivasan*, 2005]; size distribution and real refractive index [*Deuzé et al*., 2000, 2001; *Chowdhary et al.*, 2002]). Consequently, remote sensing from space plays a key role in aerosol research.

From the ground, aerosol optical depth can be derived at a high accuracy due to minimal surface effects and the straightforwardness of the retrieval algorithm (Beer's law) [*Holben et al*., 1998; *Eck et al.*, 1999]. Capabilities have been developed to estimate columnar aerosol physical and optical properties [*Nakajima et al.*, 1983, 1996; *Dubovik and King*, 2000] as well as the aerosol profiles based on surface lidar observations. Numerous global and regional observation networks have been established such as AERONET [*Holben et al*., 1998, 2001]; SKYNET [*Nakajima et al.*, 1996]; MPLNET [*Welton et al*., 2001] and EARLINET [*Matthias et al.*, 2004] to study aerosol properties and to serve in validation efforts of satellite retrievals.

2.1.4 Intensive field campaigns

The goal of extensive measurements is to 1) study aerosol microphysical, chemical and optical properties, as well as the processes controlling the formation, transport, evolution and removal of the major aerosol types; 2) perform "closure" tests to assess the mutual consistence of measurements, retrievals and theoretical calculations over a wide range of aerosol properties and effects. Table 2.2 summarizes recent major aerosol campaigns and related findings.

Table 2.2 Major aerosol field campaigns conducted in the past decade.

Name & Time	Selected Findings
	North America
SCAR-A July,1993	1. Sulfate light scattering efficiency is in the range 2.2-3.2 m^2/g and decrease with increasing altitude [*Hegg et al.*, 1996] 2. Size distribution measured from airborne instruments and derived from surface sky-radiance is in agreement in the range of 0.05-2μm, however, drawbacks associated with each method result in discrepancies at large radius end [Remer et al., 1997].
TARFOX July, 1996	1. On average, carbonaceous aerosols comprised 50% of the dry aerosol mass; contribute about two thirds to the total dry aerosol scattering; with a dry aerosol SSA being 0.9 [*Hegg et al.*, 1997]. 2. Light scattering coefficient is a function of relative humidity, at 0.55μm, mean value of the ratio of the coefficient at RH=80% to that at RH=30% is 2.3±0.24 [*Kotchenruther et al.*, 1999]. 3. SSA showed an approximate λ^{-1} variation between 0.40 and 1.0μm [*Bergstrom et al.*, 2002] 4. Calculated instantaneous changes of daytime upwelling flux are in the range of 14 to 48Wm^{-2} for midvisible optical depths between 0.2 and 0.55 [*Russell et al.*, 1999]. 5. Instantaneous SW aerosol radiative forcing is about -36Wm^{-2} at the TOA and -56Wm^{-2} at the surface for two cases [*Redemann et al.*, 2000]. 6. Remarkable year-to-year consistency was observed in the characteristics of the aerosol in the TARFOX region during episodes of heavy haze. [*Remer et al.*, 1999].
CLAMS July-August, 2001	1. Chemical compositions of fine mode aerosol mass were estimated as sulfate (55±9%); black carbon (3±1%); dust (6±8%); nitrates and organic carbon (36±10%). Episodic events of dust and pollution could dramatically change the composition [*Castanho et al.*, 2005]. 2. Averaged boundary aerosol SSA is 0.96±0.03 at 0.55μm. Mean percentage contributions to the AOD from sulfate, total carbon, condensed water, and absorbing aerosols are 38±8%, 26±9%, 32±9%, and 4±2%. Values for the mass scattering efficiencies of sulfate and total carbon (organic and black carbon) are 6.0±1.0 m^2 (g $SO_4^{=}$)$^{-1}$ and 2.6±0.9 m^2 (g C)$^{-1}$ [*Magi et al.*, 2005]. 3. It is necessary to update surface albedo and aerosol model assumptions in order to improve MODIS AOD retrievals over land [*Levy et al.*, 2005]
	Atlantic Ocean
ACE-2 June-July, 1997	1. Identification of entrainment, in-cloud scavenging and coagulation as the major processes transforming a pollution aerosol into a background marine aerosol [*Johnson et al.*, 2000; *Hoell et al.*, 2000; *Van Dingenen et al*., 2000]. 2. Transport of a polluted air mass from the continent to the ocean involves the development of a new MBL within the polluted air mass, with a residual continental layer aloft [*Johnson et al.*, 2000; *Wood et al.*, 2000] 3. In the MBL, physical, chemical and optical aerosol properties were dominated by sub-micron aerosols related to pollution aerosols advecting from the Europe [*Quinn et al.*, 2000] 4. Contribution of organic material is in a wide range to the sub-micron aerosol mass [*Putaud et al.*, 2000].
Aerosol 99 January–February, 1999	1. Aerosols in MBL exhibited distinct properties associated different air mass. Various types of aerosols originated from North America, African and Southern Hemisphere were transported over Atlantic Ocean [*Bates et al.*, 2001; *Quinn et al*., 2001]. 2. Observed averaged AOD at 0.5μm (and Angstrom Exponent) were: 0.1±0.03 (0.3±0.3) for maritime regime; 0.29±0.05 (0.36±0.13) for African dust; 0.36±0.13 (0.88±0.30) for biomass burning aerosols [*Voss et al.*, 2001a]. 3. Vertical distributions associated with various types of aerosols were observed: confined in bottom 1km for maritime aerosols; extended above 2km for dust; as high as above 4km for biomass burning [*Voss et al.*, 2001b]

Table 2.2 (Continued)

Name & Time	Selected Findings
	Europe
LACE 98 July-August, 1998	1. Aerosol properties were derived for two cases: biomass burning (real refractive index: 1.56-1.66; imaginary part: 0.05-0.07; effective radius: 0.25μm; SSA at 0.532μm: 0.78-0.83); industrial pollution (imaginary refractive index: 0.03; effective radius: 0.1-0.2μm; SSA at 0.532μm: 0.87-0.95) [*Wandinger et al*., 2002]. 2. Average complex refractive index at 0.55μm was derived: real part 1.52-1.57; imaginary part 0031-0.057 [*Ebert et al*, 2002]. 3. When RH=60%, measured average hygroscopic growth factors were in the range of 1.15–1.22, the estimated water-soluble volume fractions were in the range of 0.41–0.59 [*Busch et al.*, 2002]. 4. Agreement between measured and calculated values is on the order of ±20% for scattering and backscattering coefficients. Measured absorption coefficients were significantly smaller than the corresponding calculated values [*Wex et al.*, 2002]. 5. Daily averaged solar radiative forcing due to aerosol particles reveal cooling of the total Earth/atmosphere system ranging from -4 to -13 Wm^{-2} in cloud-free conditions [*Wendling et al.*, 2002]. 6. In most cases, ground-based aerosol data are not in consistent agreement with aircraft and lidar measurements even in cases of a well-mixed boundary layer. Significant differences in the extensive quantities were usually found [*Ansmann et al.*, 2002]]
	Dust Outflow Area
PRIDE June – July, 2000	1. During the campaign period, averaged midvisible AOD in Puerto Rico was 0.25 with maximum larger than 0.5 and clean marine periods of 0.08. Vertical distribution of dust was much complicated than the predicted scenario by Saharan Air Layer theory [*Reid et al.*, 2003b, *Maring et al*., 2003b]. 2. Dust size distributions do not appear lognormal; stokes gravitational settling overestimates losses of large dust particles during atmospheric transport [*Maring et al.*, 2003a] 3. Dust particles increase their geometric diameter <6% for a RH change from 25 to 95%. Optical properties of dust should not change for RH <95% [*Maring et al*., 2003b]. 4. Diurnal SW aerosol forcing of dust was estimated as: -12.34±9.62Wm^{-2} at TOA and -18.13±15.81Wm^{-2} at the surface [*Christopher et al*., 2003]. 5. Discrepancies exist among the derived dust size distribution from various techniques [*Reid et al.*, 2003a]
SHADE September, 2000	1. Aircraft measurements over Atlantic Ocean showed that dusts exist between 0.5 and 4.5 km; mixing of dust with sulfate was observed in the fine mode aerosols. Diminution of O3 in anticorrelation with the dust layer suggests removal of O3 by dust particles [*Formenti et al*., 2003a]. 2. At 0.55μm, averaged AOD was 1.48±0.05 during heavy dust outbreaks; SSA was 0.97±0.02; corresponding to an instantaneous direct radiative effect of -129±5 Wm^{-2}. Measurements suggest an imaginary part of the refractive index of 0.0015i for dust at 0.55μm, significant less than the standard value 0.008i [*Haywood et al*., 2003]. 3. A distinct spectral signature in infrared spectra was observed with high resolution ARIES. Longwave radiation effects due to one dust outbreak were estimated as -6.5 Wm^{-2} at TOA and 11.5 Wm^{-2} at the surface [*Highwood et al.*, 2003] 4. Spherical assumption about dust aerosol model degrade the quality of MODIS AOD retrievals [*Levy et al.*, 2003]

Table 2.2 (Continued)

Name & Time	Selected Findings
	Asia
INDOEX January - April, 1998 and 1999	1. Direct chemical measurements showed that anthropogenic sources contribute as much as 75% to the observed haze. The sub micrometer anthropogenic aerosol typically has a chemical composition (by mass) of 10-15% black carbon, 26% organic, 32% sulfate, 10% mineral dust, 5% fly ash, and smaller fractions of various other chemicals. Aerosol optical depth in visible wavelengths varies from about 0.05 in the Southern Indian Ocean (typical of unpolluted air) to between 0.4 and 0.7 (very polluted) north of the equator over the Arabian Sea and the Bay of Bengal. The aerosol layer extended as high as 3 km. The single-scattering albedo estimated by several independent methods was consistently around 0.9 both inland and over the open ocean. The most direct effect is a large negative forcing (-20±4 Wm^{-2}) at the surface and a 50 to 100% increase in solar heating of the lower atmosphere [*Ramanathan et al.*, 2001a, 2001b; *Collins et al.*, 2002; *Satheesh and Ramanathan*, 2000]. 2. Significant variability remains in platform averages of aerosol extensive properties but less in intensive properties and the ratios of constituents. Cross-platform comparisons indicate that achieving "closures" of aerosol properties within 20% will require significant improvements in techniques, calibration procedures, and comparison efforts [*Clark et al*., 2002]. 3. Cloud effective radius is observed to decrease along with the increased degree of pollution [*McFarquhar and Heymsfield*, 2001].
ACE-ASIA April, 2001	1.Regional mean midvisible AOD is about 0.4 [*Conant et al*., 2003]. Pollution aerosols, mostly confined to the boundary layer, are mixed with dust due to heterogeneous reactions and coagulation [*Anderson et al*., 2003; *Alfaro et al.*, 2003; *Chin et al.*, 2003]; which leads to the large variation of SSA (0.81-0.97) [*D.-H. Kim et al.*, 2003; *Anderson et al*., 2003]. 2.Measurements revealed multiple layers of dust and or pollution separated by clean layers *[Redemann et al*., 2003; *Bahreini et al*., 2003], and strong variation of aerosol hygroscopicity [*Carrico et al*., 2003]. 3.SW aerosol radiative forcing were estimated as: at TOA: -12 Wm^{-2} [*Conant et al*., 2003], about -10 Wm^{-2} [*Nakajima et al*. 2003]; at surface: -30.5 Wm^{-2} [*Bush and Valero*, 2003], -26 Wm^{-2} [*Markowicz et al*. 2003a], -22 Wm^{-2} [*Conant et al*., 2003] and about -23 Wm^{-2} [*Nakajima et al*. 2003] at various stations and regions. 4.The IR aerosol radiative forcing is ranging from a few Wm^{-2} and up to 10 Wm^{-2}, which can be 10–25% of the shortwave aerosol forcing at the surface, and up to 19% at TOA [*Markowicz et al.*, 2003b].
TRACE-P February -April, 2001	1. Observations showed that cold fronts sweeping across East Asia and the associated warm conveyor belts are the dominant pathway for Asian outflow to the Pacific in spring. Large fractions of sulfate and nitrate were found to be present in dust aerosols. Photochemical activity in the Asian outflow was strongly reduced by aerosol attenuation of UV radiation [*Jacob et al.*, 2003] 2. For Asian dust aerosols measured in the campaign, black carbon was internally mixed with volatile aerosol in ~85% of accumulation mode particles and constituted ~5–15% of their mass, size-integrated campaign average SSA at 0.55μm is near 0.97±0.01[*Clark et al.*, 2004].

Table 2.2 (Continued)

Name & Time	Selected Findings
	South America and Africa
SCAR-B August - September, 1995	1. Aircraft measurements showed five aerosol components (with factions of mass loading) were revealed: biomass burning (54%); soil dust (15.6%); natural biogenic component (18.7%), second soil dust (5.7%) and NaCl (59%). Fine mode aerosols account for 78% of aerosol mass; and coarse mode account for 22% [*Artaxo et al*., 1998]. Inorganic ions and black carbon together account for 15-20% of the aerosol mass load. As smoke particles aged, the median diameter (Angstrom Exponent) increased (decreased) from 0.1-0.13μm (2.5-2.9) to 0.11-0.18μm (1.8-2.3) due to condensation [*Reid and Hobbs*, 1998; *Reid et al.*, 1998a]. Smoke particles can be reasonably approximated as spherical one hour after emission [*Martins et al*, 1998]. Relative low hygroscopicity was associated with smoke particles in Brazil [*Kotchenruther and Hobbs*, 1998]. For regional haze, SSA varied between 0.8 and 0.9 with an uncertainty of ±0.04 to ±0.08 for different optical methods [*Reid et al*., 1998b] 2. Ground-based remote sensing documented that SSA at 0.55μm ranged from 0.82 to 0.94 and decreased with increasing wavelengths [*Eck et al.*, 1998]. A dynamic smoke aerosol model was derived based on AERONET measurements, which is built into MODIS aerosol retrieval scheme [*Remer et al.*, 1998]. 3. Radiative effects of biomass burning aerosols were estimated as: -20±7 Wm^{-2} per unit optical depth at TOA for a typical forest burning aerosol; -8±9 Wm^{-2} over the cerrado. A positive forcing efficiency (+25±12 Wm^{-2}) was calculated over bright surface [*Ross et al*., 1998]. Ruction of PAR at surface ranged from 20 to 45% [*Eck et al*., 1998].
SAFARI-2000 August - September, 2000	1. The regional haze aerosol was composed mostly of carbonaceous aerosols (on the average, 81% of the submicron mass), with secondary inorganic aerosols (sulfate, ammonium, and nitrate) accounting for another 14% [*Formenti et al*., 2003b]. Carbohydrate comprised 36% and 27% of the total aerosol mass in haze and smoke aerosols [*Gao et al*., 2003] 2. The submicron size distribution of aged regional haze was fitted with three lognormal distributions with geometric mean radii of 0.12, 0.26 and 0.80μm. For aged regional haze, asymmetry factor was 0.59±0.02 and SSA was 0.91 ± 0.04 at 0.55μm [*Haywood et al*., 2003]. Based no surface fluxes measurements, aerosol SSA was estimated as being between 0.85 and 0.90 at 350 nm, decreasing to 0.6 in the near infrared [*Bergstrom et al*., 2003]. Retrieved midvisible SSA from PAR flux measurements and AERONET yielded an average value of 0.84 [*Eck et al*., 2003]. 3. Over land, aerosols become well mixed in the vertical from the surface to approximately 500 hPa [*Haywood et al*., 2003]. Observed also a clear separation between an elevated biomass aerosol layer (1.8–3.7 km altitude) and low-level stratiform clouds [*Keil and Haywood*, 2003] 4. Based on analysis of two days data, aerosol radiative effects were estimated as about -15 W m^{-2} at TOA and reduction of surface downward fluxes can be as large as 200 W m^{-2} [*Bergstrom et al*., 2003]. Over the ocean part of the campaign region, a forcing of −10 W/m^2 at TOA and approximately −26 W/m^2 at the surface was estimated for Sep. 2003 [*Ichoku et al*., 2003]. Presence of clouds converted the negative TOA forcing by the biomass aerosol in clear skies into a positive one (from −13.0 Wm^{-2} to +11.5 Wm^{-2} for average optical properties of the biomass aerosol and a solar zenith angle of 60°) [*Keil and Haywood*, 2003]. Local cooling effects over -50 Wm^{-2} was also reported [*Myhre et al*., 2003].

Table 2.2 (Continued)

Name & Time	Selected Findings
	Southwest Pacific Ocean
ACE-1 Nov.15–Dec.14, 1995	1. Chemical composition of submicron aerosol: sea salt (80±10%); sulfate (16±8%) and methanesulfonate (4±3%); sea salt compose 99±0.7% of supermicor aerosol. Averaged SSA is about 0.99 [Quinn et al., 1998]. 2. Background MBL aerosol was composed of four distinct modes: ultrafine (5-20nm), Aitken (20-80nm), accumulation (80-300nm) and coarse modes (>300nm) [*Bates et al*., 1998]. 3. Layers containing continent aged biomass burning aerosols were observed above 3km over the remote southern Pacific and near New Zealand [*Blake et al.*, 1999]. 4. Discrepancies exist in the model calculated and measured scattering coefficients in the supermicron size range due to the inadequacy of measuring technique [*Quinn and Coffman.*, 1998]

Detailed aerosol physical, chemical and optical properties can be explored by in situ methods, but they are limited by the spatial and temporal coverage, as well as uncertainties due to sampling and measurement technique issues [*Remer et al.*, 1997; *Reid et al.*, 1998b; *Quinn and Coffman.*, 1998; IPCC, 2001; *Ansmann et al.*, 2002; *Reid et al.*, 2003a; *Moore et al.*, 2004]. As such, a single approach is not sufficient to address global scale aerosol issues and an integrative approach is needed togenerate a complete description of aerosol properties [*Charlson,* 2001; *Kaufman et al*., 2002a; *Diner et al*., 2004].

2.2 Relationship between SW surface fluxes and TOA reflection

Driven by the TOA reflection, satellite-based SRB estimation is a comprehensive activity since all the processes that impact the SW radiative transfer (i.e., molecular scattering; gases absorption; surface reflection; aerosol extinction and cloud effect) play a role. The complex interactions between incoming solar radiation and the Earth-atmosphere system can be decomposed into two fundamental

components: 1) extinction within the atmosphere (characterized by the atmospheric scattering, absorption and transmission); 2) reflection and absorption by the earth surface (determined by surface bidirectional reflectance, or approximately, surface albedo). Based on the adding equation of radiative transfer in a vertical inhomogeneous atmosphere over a "semi-lambertian"[2] surface, planetary albedo (r), fractional surface downward flux (t) and fractional surface net solar radiation (absorption at the surface) (n) for a specified solar zenith angle μ_0 can be expressed as:

$$r = R_a(\mu_0) + \frac{\left(R_s(\mu_0)T_a^{dir}(\mu_0) + \tilde{R}_s\, T_a^{dif}(\mu_0)\right)\tilde{T}_a}{1 - \tilde{R}_s\,\tilde{R}_a} \tag{2.4}$$

$$t = T_a^{dir}(\mu_0) + \left(T_a^{dif}(\mu_0) + \frac{\left(R_s(\mu_0)T_a^{dir}(\mu_0) + \tilde{R}_s\, T_a^{dif}(\mu_0)\right)\tilde{R}_a}{1 - \tilde{R}_s\,\tilde{R}_a} \right) \tag{2.5}$$

$$n = \left(1 - R_s(\mu_0)\right)T_a^{dir}(\mu_0) + \left(1 - \tilde{R}_s\right)\left(T_a^{dif}(\mu_0) + \frac{\left(R_s(\mu_0)T_a^{dir}(\mu_0) + \tilde{R}_s\, T_a^{dif}(\mu_0)\right)\tilde{R}_a}{1 - \tilde{R}_s\,\tilde{R}_a} \right) \tag{2.6}$$

where $R_s(\mu_0)$ and $\tilde{R}_s$ is the black-sky and white-sky surface albedo; $R_a(\mu_0)$, $T_a^{dir}(\mu_0)$ and $T_a^{dif}(\mu_0)$ are the reflectance, direct and diffuse transmittance of the atmosphere over a nonreflecting surface, respectively; $\tilde{R}_a$ and $\tilde{T}_a$ are the atmosphere spherical

[2] For the semi-lambertian surface approximation, surface reflectance is described by two variables: directional hemispherical reflectance (black-sky albedo) and bi-hemispherical reflectance (white-sky albedo).

albedo and transmittance (for the surface reflected radiation). All the parameters can be treated either as monochromatic or effective values over any solar spectral band.

Planetary albedo (r) can be derived from satellite measurements through anisotropic correction and possible narrow to broadband conversion depending on the spectral bandwidth of the sensors. The essence of SRB satellite algorithms is to relate r to t and n. Generally, there are two types of algorithms: physical methods based on the radiative transfer Eqs. (2.4-2.6); they aim to estimate optical parameters ($T_a^{dir}(\mu_0)$, $T_a^{dif}(\mu_0)$, $\tilde{R}_a$, $\tilde{T}_a$, $R_s(\mu_0)$ and $\tilde{R}_s$) that are used in surface flux calculations; the other scheme uses simple relationships that directly link TOA reflection with surface fluxes [*Tarpley*, 1979; *Klink and Dollhopf, 1986; Li et al.,* 1993a]. In the following, we will explore the relationship between TOA and surface fluxes in terms of analytical expressions. Combined with the sensitivity tests of the next Chapter, addressed will be the issue of incorporating aerosol effects into satellite algorithms in a complete and efficient way.

In Eqs. (2.4-2.6), simple substitution and elimination method can be applied to analytically study the relationships between surface fluxes and TOA albedo. *Laszlo and Pinker* [1994] presented the coefficients of a linear relationship between SW net radiative fluxes at the TOA and surface in terms of atmospheric optical functions. Similarly, we can get[3]:

$$t = \left(1 - A_a(\mu_0) - \frac{1-\tilde{A}_a}{\tilde{T}_a} R_a(\mu_0)\right) + \frac{\tilde{R}_a}{\tilde{T}_a} r \qquad (2.7)$$

[3] Derivation of Eqs. (2.7-2.10) can be found in Appendix A.

$$n = \left(1 - A_a(\mu_0) + \frac{\tilde{A}_a}{\tilde{T}_a} R_a(\mu_0)\right) - \left(1 + \frac{\tilde{A}_a}{\tilde{T}_a}\right) r \qquad (2.8)$$

where $A_a(\mu_0)$ is the atmospheric absorption over a nonreflecting surface; $\tilde{A}_a$ is the atmospheric spherical absorption (for the surface reflected radiation). Eliminated in these equations is the explicit dependence on surface albedo. If surface reflectance is further simplified as being lambertian (independent on the solar position, characterized by surface albedo R_s), another set of linear equations that require the representation of atmospheric absorption and surface albedo, can be derived as:

$$t = \frac{1}{1 - R_s\left(1 - \tilde{A}_a\right)}\left(1 - A_a(\mu_0)\right) - \frac{1}{1 - R_s\left(1 - \tilde{A}_a\right)} r \qquad (2.9)$$

$$n = \frac{1 - R_s}{1 - R_s\left(1 - \tilde{A}_a\right)}\left(1 - A_a(\mu_0)\right) - \frac{1 - R_s}{1 - R_s\left(1 - \tilde{A}_a\right)} r \qquad (2.10)$$

The above seemingly different formulations are not in contradiction since the dependence on the eliminated variables remains implicitly in the planetary albedo term.

It should be noted that these linear relationships (i.e., $t = A + Br$ and $n = C + Dr$) are derived only for instantaneous conditions, thus, coefficients (A, B, C and D) might change from one scenario to the other. Of interest is to determine if such coefficients can be assumed constant or can be parameterized in terms of predetermined variables to facilitate a simple transformation from TOA reflection to surface fluxes. An example of such an approach to derive the net surface solar fluxes is given in *Li et al*. [1993a]. Applicability of this linear transformation

can be explained by Eq. (2.8). For clear-sky cases without absorbing aerosols, due to the small magnitude of $\frac{\tilde{A}_a}{\tilde{T}_a}$ (around 0.1) and $R_a(\mu_0)$, the intercept $1 - A_a(\mu_0) + \frac{\tilde{A}_a}{\tilde{T}_a} R_a(\mu_0)$ is primarily determined by $A_a(\mu_0)$, and the slope $-\left(1 + \frac{\tilde{A}_a}{\tilde{T}_a}\right)$ is relatively invariant. Therefore, both terms can be adequately parameterized in terms of the solar zenith angle and water vapor. For the cloudy cases; $\frac{\tilde{A}_a}{\tilde{T}_a} R_a(\mu_0)$ and $-\frac{\tilde{A}_a}{\tilde{T}_a} r$ are non-negligible due to enhanced reflection. Yet, the opposite signs and closeness of $R_a(\mu_0)$ and r lead to the cancellation of these two terms. Therefore, if clouds do not significantly increase SW atmospheric absorption, small corrections to the clear-sky coefficients might yield satisfactory results.

For the radiative transfer-based satellite algorithms, one can derive parameters of choice from Eq. (2.4) and use them in Eqs. (2.5) and (2.6) to calculate the surface fluxes. These fundamental steps match the substitution and elimination procedures used in the analytical derivation, therefore, the linear relationships of Eqs. (2.7-2.10) are implicitly incorporated in the estimation results. This explains the agreement between the estimated net surface SW radiation from these two schemes [*Li,* 1995a].

Chapter 3: Aerosol sensitivity tests

3.1 Aerosol radiative effects on surface SW irradiance

For a cloudless atmosphere, extinction of incoming solar radiation is determined by the molecular (Rayleigh) scattering, gaseous absorption (predominantly by H_2O and O_3) and aerosol interactions. To explore the aerosol effect relative to the others, we perform a radiative transfer calculation with high spectral resolution. The profile of the US standard atmosphere (USSA1976) is used as input to the DISORT radiative transfer model [*Stamnes et al*., 1988]. Total column amount of water vapor and O_3 are 1.42 cm and 0.34 atm-cm, respectively. Parameterization schemes adopted by MODTRAN [*Kneizys et al*., 1996] are used to calculate Rayleigh scattering and molecular absorptions, where band model parameters (absorption coefficient, line density and line width) are derived from the HITRAN 1992 line atlas [*Anderson et al.*, 1993] for a bin width of one wave-number ($\Delta\nu = 1 \ \ cm^{-1}$) between 2500 and 22600 cm^{-1}. Calculation at the short end of wavelength ($> 22600\, cm^{-1}$) is based on the band model and parameters developed by *Pierluissi and Maragoudakis* [1986] with a resolution of $5\, cm^{-1}$. Aerosols, with assumed spectrally independent optical depth (τ) of 0.2, single scattering albedo (ω_0) of 0.9, and asymmetry parameter (g) of 0.7, are uniformly located in the bottom 2 km of the atmosphere over a nonreflecting surface. Model simulations are carried out sequentially by adding O_3, H_2O, Rayleigh scattering, other minor absorbing gases (O_2, CO_2, CH_4, N_2O, SO_2, CO, N_2, NH_3, NO_2, NO, HNO_3) and aerosols. The

resulting differential decrease of the surface downward SW flux is taken as an approximated estimation of the individual effects. Reported are the diurnally averaged values, which are calculated following *Cess* [1985]:

$$\overline{F} = \frac{1}{2}\int_0^1 F(\mu_0)d\mu_0 \qquad (3.1)$$

8-point Gaussian quadrature is used to perform the integral. Figure 3.1 shows the simulation results over the solar spectrum. As seen, the depletion of solar irradiance by an AOD of 0.2 of relatively absorbing aerosols is larger than the ozone absorption and comparable to Rayleigh scattering, which indicates the relative importance of aerosol effects.

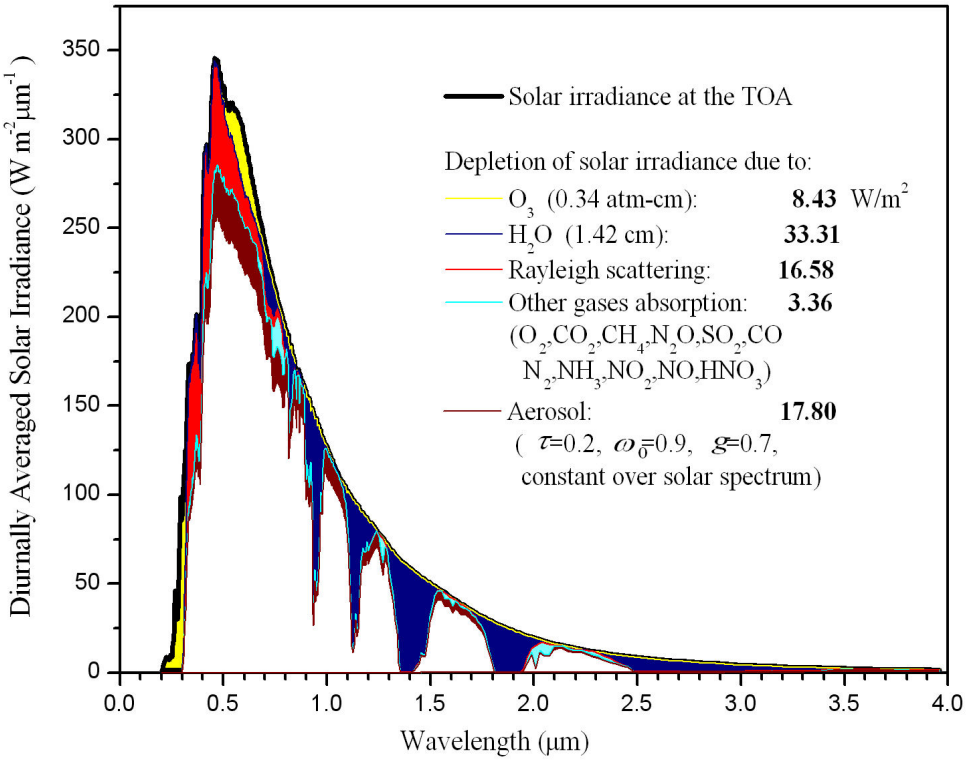

Figure 3.1 Diurnally averaged solar irradiance curve at TOA and surface for a US standard atmosphere (1976) profile with user-assumed aerosols over a nonreflecting surface. Shaded areas are the depletions of SW radiation due to various radiatively active agents.

In order to incorporate the diverse radiative properties of ambient aerosols for a more realistic simulation, five aerosol models are selected to represent key aerosol types: two types of urban pollution (differing by their absorbing strength and possible mixture with dust particles), biomass burning (e.g., African savanna) and dust (e.g., Persian Gulf) aerosols are obtained from the AERONET almucantar retrievals [*Dubovik et al*., 2002]. Properties of maritime aerosols are taken from the OPAC model [*Hess et al.,* 1998] and their assumed vertical distribution is described in Table 3.1.

Table 3.1 General information of five aerosol models used in the sensitivity tests.

Aerosol Type	Measurements Taken at	Altitude (uniformly distributed within)	Optical Data Source and Reference
Industrial (a)	GSFC, US	0-3 km [*Hignett et al.*, 1999]	AERONET [*Dubovik et al*., 2002]
Industrial (b)	Maldives	0-2 km [*Ramanathan et al*., 2001]	
Biomass Burning	Zambia	0-5 km [*Haywood et al.*, 2003]	
Dust	Bahrain-Persian Gulf	0-5 km [*Formenti et al*., 2003a]	
Maritime		0-2 km	OPAC [Hess *et al*., 1998]

Aerosol radiative properties resulting from Mie calculations are displayed in Figure 3.2. Due to the limitation of wavelength coverage from AERONET sky radiance measurements (available at 0.44, 0.67, 0.87 and 1.02 μm), complex refractive indices at wavelengths within 0.20-0.44 μm and 1.02-4.00 μm are assumed to be constant. Such approximations affect the estimation of absorption of dust (significant and variable over the short end of the solar spectrum [*Patterson et al.*,

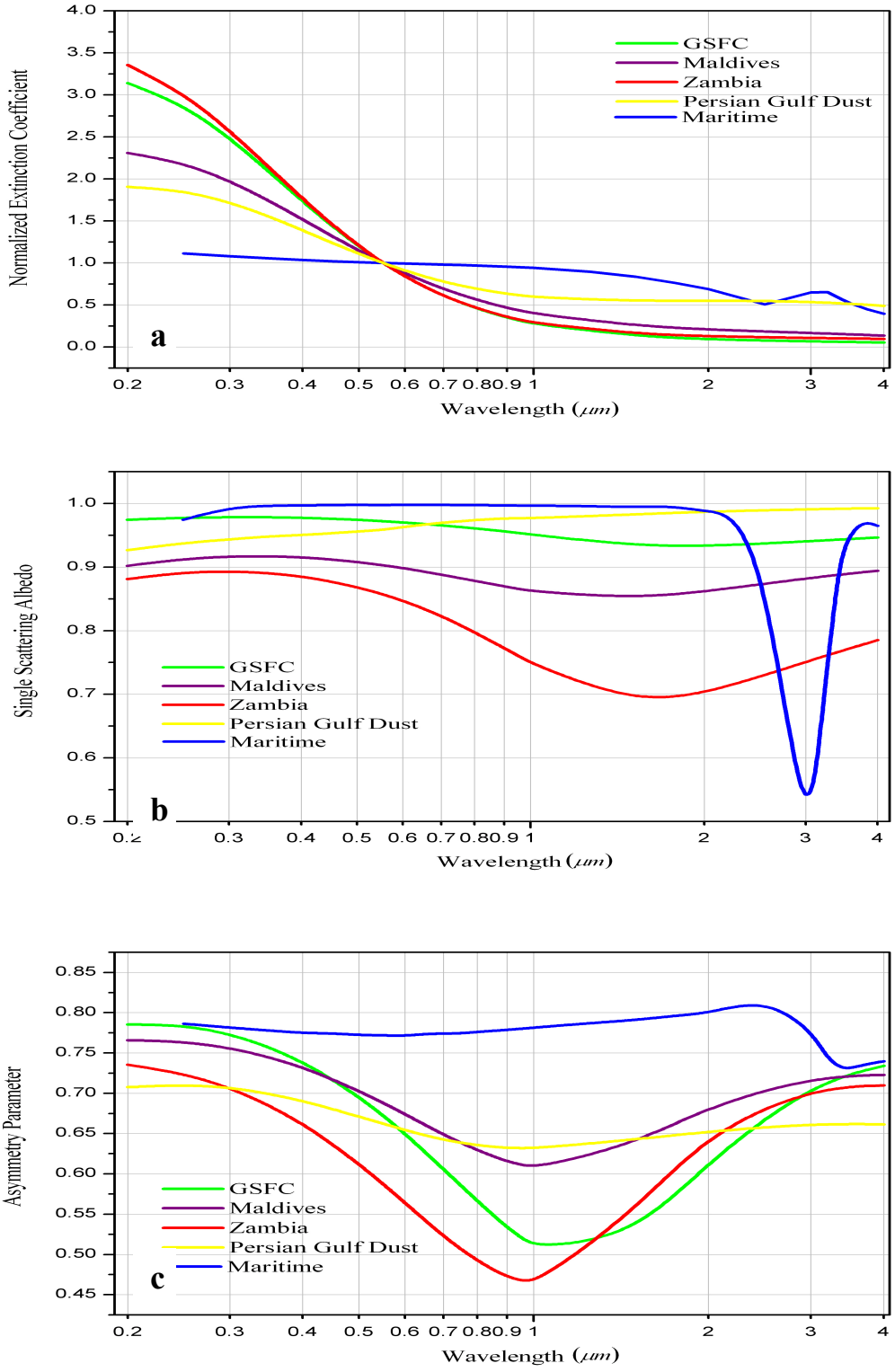

Figure 3.2 (a) Extinction coefficients (normalized to the value at 0.55 μm); (b) Single scattering albedo and (c) Asymmetry parameter of five aerosol types used for model simulations.

1977]) and of hygroscopic aerosols around 3μm (strong water absorption). Due to their overlap with strong ozone and water vapor absorption bands, and the relatively small fraction of incoming solar energy within the shortwave infrared (SWIR) range (Figure 3.1), this uncertainty will not have a significant impact on the estimation of the surface SW fluxes.

Daily averaged reduction in surface downward SW fluxes is displayed in Figure 3.3 for various concentrations of five aerosol models. For one unit of aerosol optical depth at 0.55 μm, depletion of solar irradiance ranges from 35 to 62 W/m^2, with the strongest effect coming from soot-rich biomass burning and the weakest from maritime aerosols. The spectral behavior of aerosol effects associated with each type also differ (stronger SWIR effects are associated with large particles). In terms of observation-based estimations, diurnal aerosol surface forcing efficiency (reduction of 24 hour averaged clear-sky surface SW absorption per unit AOD at 500nm) from the various field campaigns is reported as -75 Wm^{-2} for INDOEX [*Ramanathan et al.*, 2001]; -70 Wm^{-2} for TARFOX [*Russell et al.*, 1999]; -74 Wm^{-2} for the Gosan site [*Bush and Valero*, 2003], -60 Wm^{-2} for the Sea of Japan [*Markowicz et al*, 2003], and -55 Wm^{-2} for the east Asian area [*Conant et al.*, 2003] during ACE-Asia. In SAFARI 2000, *Bergstrom et al*. [2003] estimated the instantaneous reduction of surface downward fluxes for two cases with different aerosol types and loadings as being 57 Wm^{-2} and 208 Wm^{-2}; *Myhre et al* [2003] reported the surface impact normalized to unit AOD between -50 and -90 Wm^{-2}. *Pandithurai et al.* [2004] calculated the aerosol surface forcing as -31 Wm^{-2} at a tropical urban site in India. *Nakajima et al.* [2003] conclude that aerosol surface

direct forcing can be comparable to cloud radiative effects (SW + IR) over the East China Sea region.

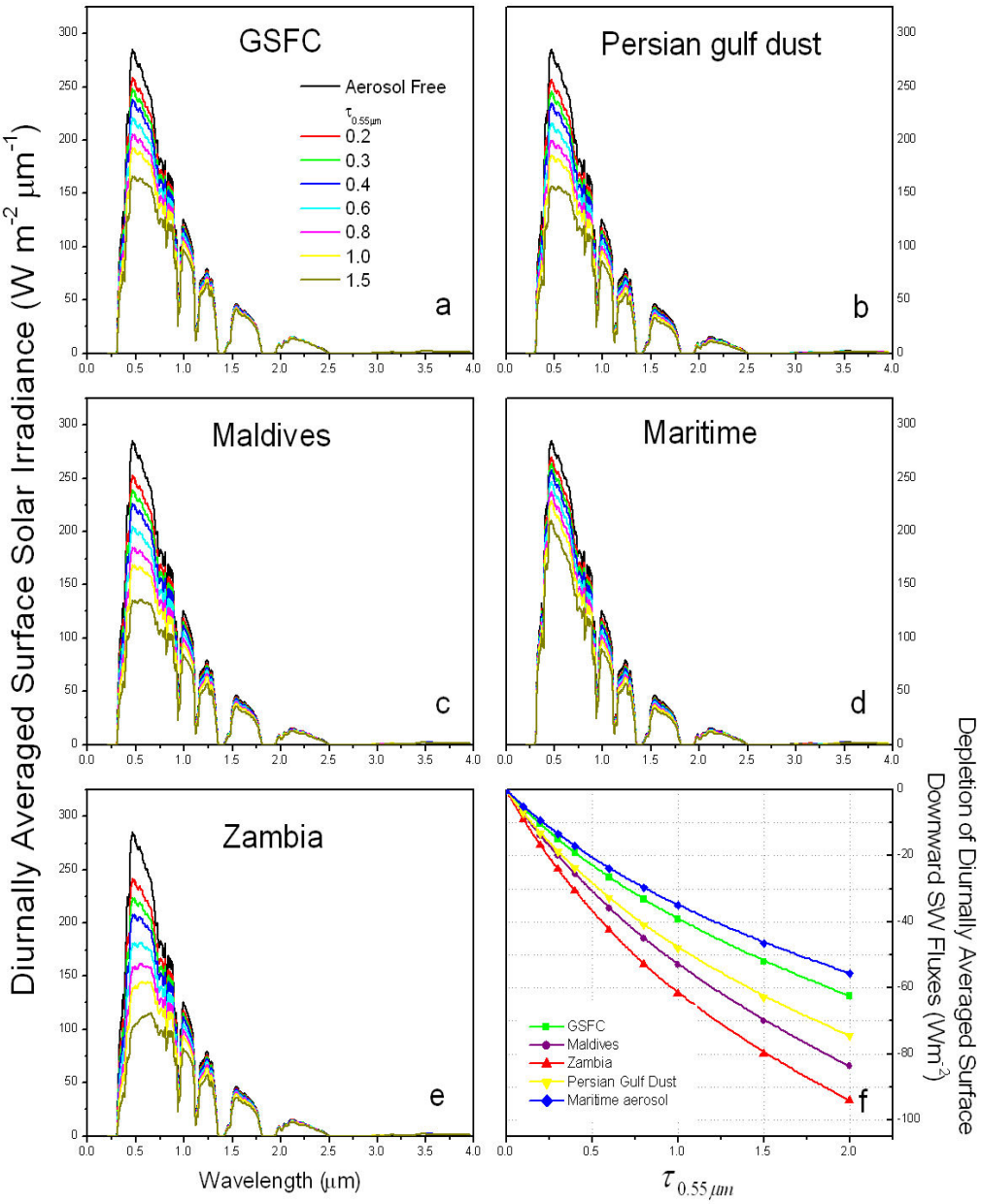

Figure 3.3 Diurnally averaged surface solar irradiance curve for a US standard atmosphere (1976) profile over a nonreflecting surface with five types of aerosols: a) Urban/industrial over GSFC; b) Persian Gulf dust; c) Urban/industrial over Maldives; d) Maritime; e) biomass burning of African savanna; f) Depletion of surface irradiance for various loading of different types of aerosols.

We performed a case study on aerosol surface radiative effects at Ilorin, Nigeria, where large aerosol concentrations from biomass burning and dust outbreaks were reported from the AERONET and from satellite retrievals during the dry season (roughly from December to February). Figure 3.4 shows that time series of daily averaged aerosol optical depth at 0.50 μm (from AERONET) and surface insolation measurements during three dry seasons are generally in opposite phase, which clearly signals the impact of aerosols. To assess the reduction in surface SW fluxes due to ambient aerosols, the SBDART model [*Ricchiazzi et al*., 1998] was used to simulate aerosol-free conditions over a vegetative surface. Input atmospheric profiles were taken from NCEP-DOE Reanalysis 2 dataset [*Kanamitsu et al*., 2002; *Kalnay et al*., 1996], and daily column O_3 amount from TOMS retrievals (http://toms.gsfc.nasa.gov/ozone/ozone_v8.html). Ninety-two days were identified as cloud-free based on the visual examination of the smoothness of one-minute flux data. Daily averaged depletion of surface insolation, calculated as the difference between pyranometer-measured and model-simulated irradiance, is displayed in Figure 3.5 as functions of AOD and Ångström exponent (α). At Ilorin, one unit of AOD at 0.5 μm corresponds to a decrease of surface insolation as about 90 Wm^{-2}. Larger Ångström exponent cases, most likely associated with local pollution with strong aerosol absorption tend to have a larger effect than dust dominated conditions (smaller α) with the same optical depths. Therefore, quantifying anthropogenic aerosol effects is of great importance.

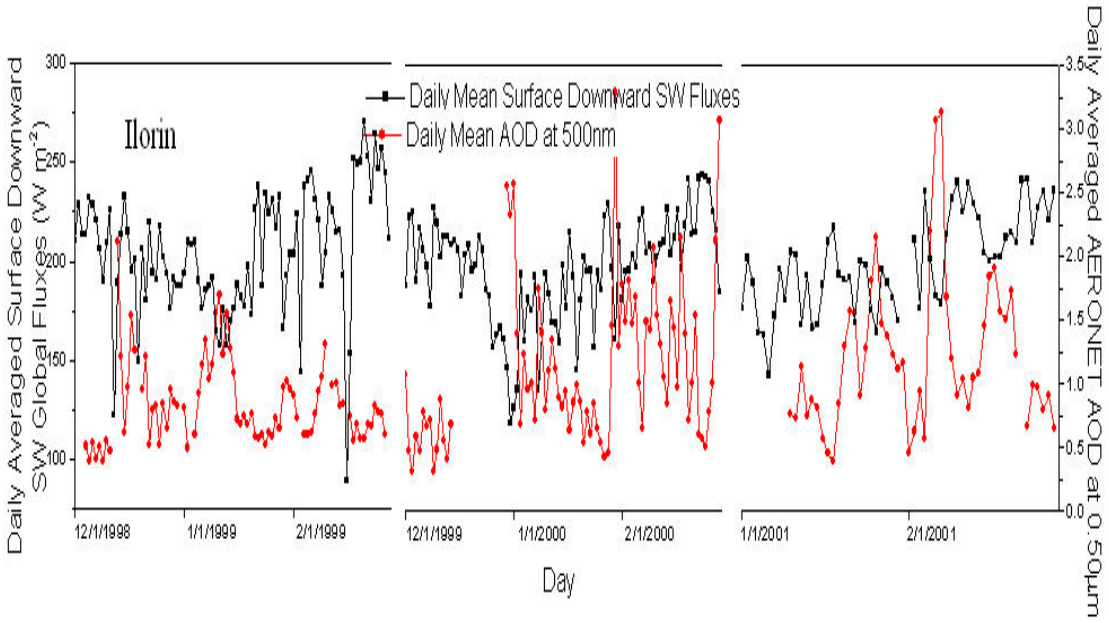

Figure 3.4 Diurnally averaged surface downward SW fluxes and aerosol optical depth (500 nm) for three dry seasons (Dec 1998-Feb 1999; Dec 1999-Feb 2000; Jan-Feb 2001) at Ilorin, Nigeria (08°32' N; 04°34' E).

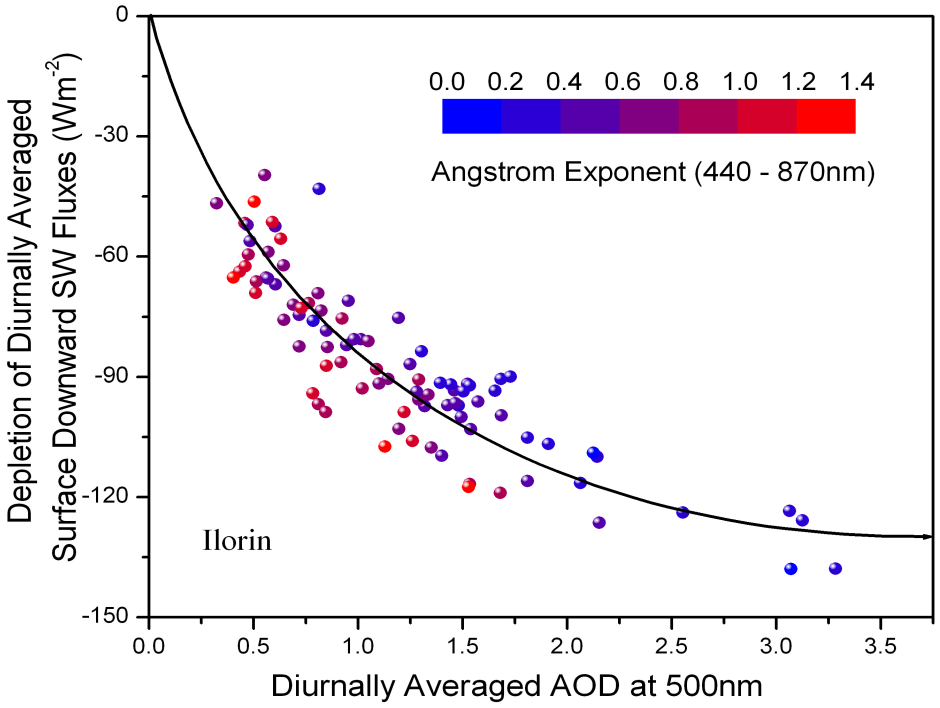

Figure 3.5 Depletion of diurnally averaged surface downward SW fluxes as the functions of AOD (500 nm) and Angstrom Exponent (440-870 nm) at Ilorin (Nigeria) for three dry seasons (1998-2001).

To assess the global annual aerosol direct surface radiative effect, we follow the methodology used for estimation of aerosol top-of-atmosphere (TOA) radiative forcing [*Charlson et al*., 1991, 1992; *Penner et al.*, 1992*; Chylek and Wong*, 1995; *Hobbs et al.*, 1997]; simple radiative transfer calculations are performed with an aerosol layer inserted between the aerosol-free atmosphere and the surface. We denote the average spherical transmittance and reflectance of the Rayleigh sky above the aerosol layer as T_{atm} and R_{atm}; for the aerosol layer as T_{aer} and R_{aer}; if α is the underlying surface albedo, utilizing the adding equation [*Hansen and Travis*, 1974], for the combined atmosphere and aerosol column will yield:

$$T_{tot} = T_{atm}T_{aer} \Big/ \left(1 - R_{atm}R_{aer}\right) \tag{3.2}$$

$$R_{tot}^{\Uparrow} = R_{aer} + R_{atm}T_{aer}^2 \Big/ \left(1 - R_{atm}R_{aer}\right) \tag{3.3}$$

where T_{tot} is the total columnar transmittance and $R_{tot}^{\Uparrow}$ is the combined (atmosphere and aerosol layers) reflectance for the bottom illumination. Aerosol-induced change of the normalized surface SW downward flux can be represented as:

$$\begin{aligned} \Delta F_{suf} &= \frac{T_{tot}}{1 - R_{tot}^{\Uparrow}\alpha} - \frac{T_{atm}}{1 - R_{atm}\alpha} \\ &= \frac{T_{atm}T_{aer}}{\left(1 - R_{atm}R_{aer}\right)\left(1 - R_{aer}\alpha\right) - R_{atm}T_{aer}^2\alpha} - \frac{T_{atm}}{1 - R_{atm}\alpha} \end{aligned} \tag{3.4}$$

For a clear-sky aerosol-free atmospheric layer, the values of optical functions (R_{atm} and T_{atm}) are taken from a global average, namely, $R_{atm} = 0.06$, $T_{atm} = 0.77$ (with about 4% and 13% solar radiation being absorbed by O_3 and water vapor), and global averaged surface albedo of 0.15 is assumed [*Charlson et al*.,1992]. For the

aerosol layer, two-stream formulations are used to estimate T_{aer} and R_{aer} [*Coakley and Chylek*, 1975]:

$$R_{aer} = \frac{(U+1)(U-1)\left[\exp(2\alpha'\tau) - \exp(-2\alpha'\tau)\right]}{(U+1)^2 \exp(2\alpha'\tau) - (U-1)^2 \exp(-2\alpha'\tau)} \tag{3.5}$$

$$T_{aer} = \frac{4U}{(U+1)^2 \exp(2\alpha'\tau) - (U-1)^2 \exp(-2\alpha'\tau)} \tag{3.6}$$

where:

$$U = \sqrt{\left(1 - \omega_0 + 2\omega_0 \overline{\beta}\right) \Big/ \left(1 - \omega_0\right)} \tag{3.7}$$

$$\alpha' = \sqrt{\left(1 - \omega_0 + 2\omega_0 \overline{\beta}\right)\left(1 - \omega_0\right)} \tag{3.8}$$

ω_0 is single scattering albedo, $\overline{\beta}$ is the backscattered fraction of isotropically incident radiation. Both aerosol optical parameters are the solar broadband average. $\overline{\beta}$ is calculated from the asymmetry parameter (g) based on the formulation derived by *Wiscombe and Grams* [1976] for the Henyey-Greenstein phase function:

$$\overline{\beta_{HG}} = \frac{1-g}{2g}\left[\frac{2}{\pi}(1+g)K(g^2) - 1\right] \tag{3.9}$$

$$K(g^2) = \int_0^{\pi/2} \left(1 - g^2 \sin^2\theta\right)^{-\frac{1}{2}} d\theta \tag{3.10}$$

Simulations are carried out for five aerosol models (Table 3.1) with $\tau_{0.55\mu m}$ varying from 0.1 to 0.6. The SW broadband optical parameters τ (corresponding to unit $\tau_{0.55\mu m}$), ω_0 and g are weighted-averaged by:

$$\tau = \int \sigma_{ext}(\lambda) S(\lambda) d\lambda \Big/ \int S(\lambda) d\lambda \tag{3.11}$$

$$\omega_0 = \int \omega_0(\lambda)\sigma_{ext}(\lambda)S(\lambda)d\lambda \Big/ \int \sigma_{ext}(\lambda)S(\lambda)d\lambda \tag{3.12}$$

$$g = \int g(\lambda)\omega_0(\lambda)\sigma_{ext}(\lambda)S(\lambda)d\lambda \Big/ \int \omega_0(\lambda)\sigma_{ext}(\lambda)S(\lambda)d\lambda \tag{3.13}$$

$\sigma_{ext}(\lambda)$, $\omega_0(\lambda)$, $g(\lambda)$ and $S(\lambda)$ are aerosol spectral normalized extinction coefficient (normalized to 0.55 μm), single scattering albedo, asymmetry parameter and solar constant, respectively. In Table 3.2 listed are the derived broadband optical parameters.

Table 3.2 SW broadband aerosol optical parameters of five aerosol models used in simulation.

Aerosol Type	SW broadband aerosol optical parameters			
	τ	ω_0	g	$\overline{\beta}$
Industrial (a)	0.745534	0.970766	0.677821	0.224644
Industrial (b)	0.763716	0.897712	0.688620	0.219372
Biomass Burning	0.760559	0.850330	0.607242	0.257809
Dust	0.858370	0.963917	0.661138	0.232677
Maritime	0.943716	0.992554	0.778430	0.172862

Global annual averaged reduction of surface insolation is calculated as follows:

$$\overline{\Delta SWF_{surf}} = \frac{1}{4} S_0 \left(1 - \overline{A_c}\right) \Delta F_{suf} \tag{3.14}$$

where $\frac{1}{4} S_0$ is the global average of incoming solar radiation (343 Wm^{-2}) and $\overline{A_c}$ is the global average fraction of cloud cover (60%). The simulation results shown in Figure 3.6 reveal substantial reduction in surface SW downward flux (between -5 and

-15Wm^{-2} for an assumed global average $\tau_{0.55\mu m}$ of 0.15), and large differences are associated with various types of aerosols.

In terms of surface SW radiation budget, results from above sensitivity tests and observations suggest that 1) high aerosols concentration could significantly reduce the SW radiation reaching the ground; 2) spectral variation of extinction, absorption and scattering properties also need to be taken into consideration; 3) linearity of aerosol effect is valid only for small to medium AODs (Figure 3.3f and 3.5), and therefore, regression based forcing efficiency should be used with caution.

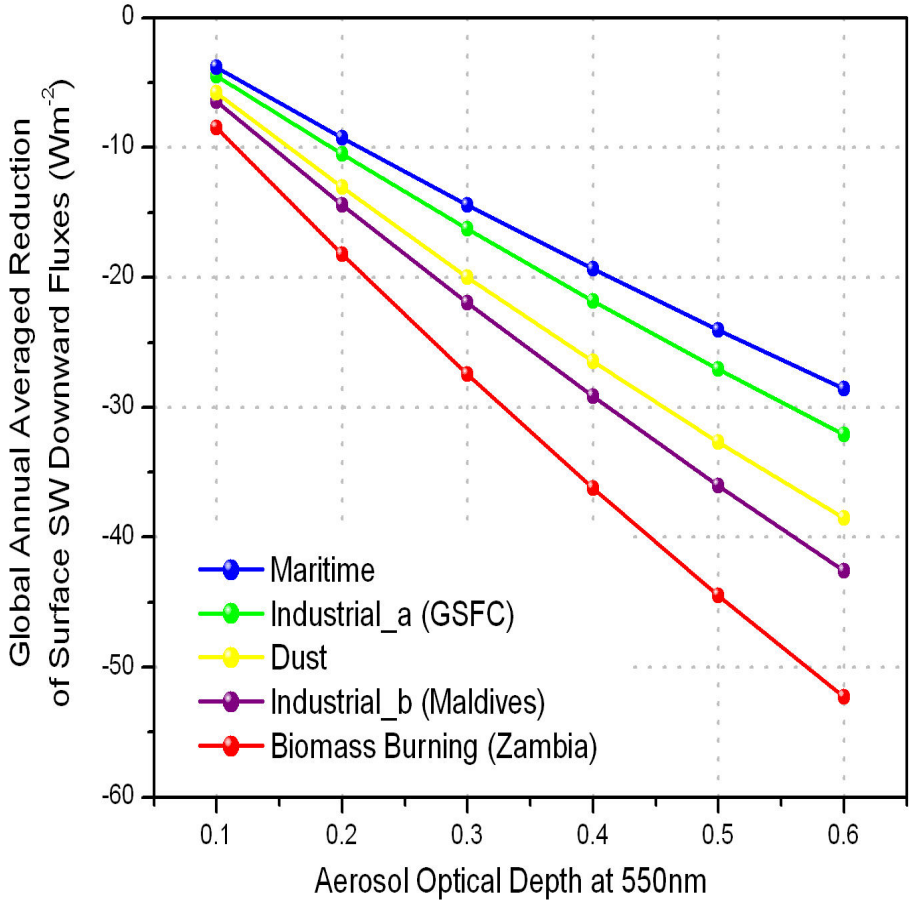

Figure 3.6 Global annually averaged reduction of surface SW downward fluxes as a function of aerosol type and concentration.

3.2 Aerosol effects on the relationship between surface SW fluxes and TOA reflection

In the previous section, depletion of surface irradiance due to aerosols is studied as a forward problem. Regarding the inverse problem of satellite-based surface flux estimation, of interest is how aerosol uncertainties impact the estimates of surface fluxes given a measured TOA reflection. In Figure 3.7 shown are the simulated surface downward SW fluxes versus TOA reflection for a solar zenith angle of 60º and various combinations of aerosol types, aerosol concentrations ($\tau_{0.55\mu m}$) and surface albedo. Solid lines follow the variation of aerosol optical depth; along the dotted lines changed is only surface albedo. As seen, for a given TOA reflection, different types of aerosols will greatly impact the estimate of surface irradiance. For example, for a surface albedo of 0.1 and TOA upward SW flux of 120 Wm^{-2}, the difference in the estimated surface downward flux can be as large as 80 W/m^{-2} between biomass burning (Zambia) and industrial (GSFC) aerosols.

Further findings from Figure 3.7 are:

1) Aerosol impact depends on surface albedo (solid lines).

Most apparent are the cases where strong absorbing aerosols dominate (Zambia and Maldives). Over a dark surface, an increase of TOA reflection is associated with a decrease of surface downward flux. Such relationship can be reversed when the surface becomes brighter. This imposes difficulties on satellite algorithms since both aerosols and surface properties are unknown and need to be determined from the observed TOA albedo.

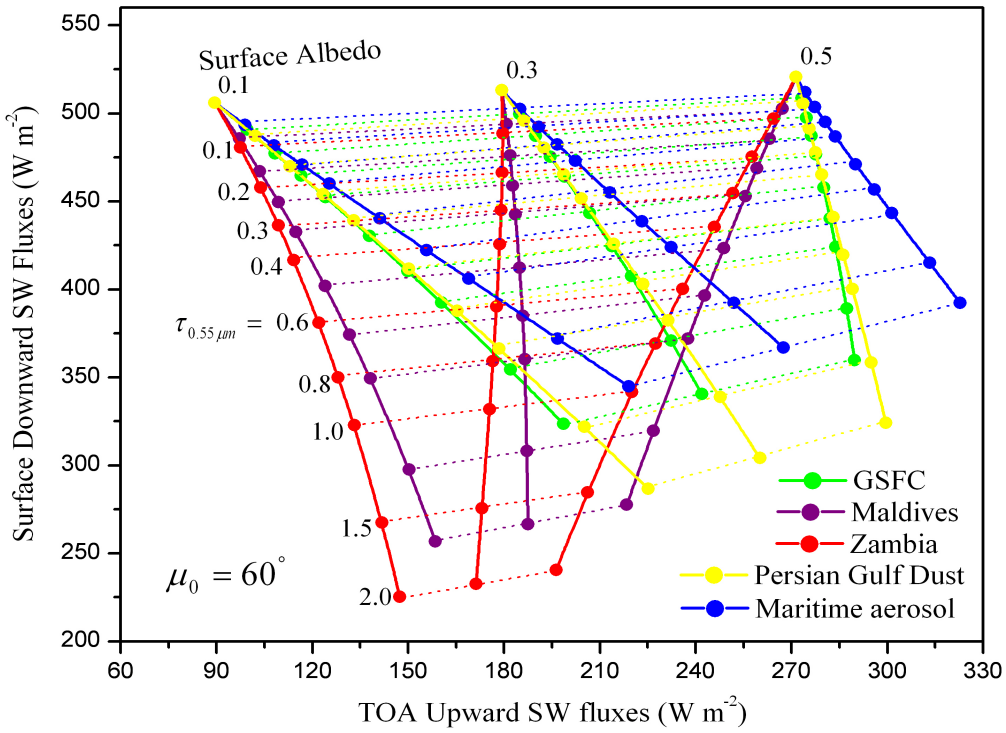

Figure 3.7 Simulated surface downward SW fluxes versus TOA reflection for various combinations of aerosol types, aerosol aerosol optical depth at 0.55 μm and surface albedo. The solar zenith angle is set to be 60º and US standard atmosphere (1976) profile is used as the model input. Dotted lines represent the derived linear relationship (Eq. (2.4)) between TOA reflection and surface insolation.

2) Small errors in surface albedo will affect the aerosol retrieval and corresponding surface flux estimation.

For example, for less absorbing industrial aerosol (GSFC), an uncertainty of 0.02 in surface albedo will lead to large errors of retrieved $\tau_{0.55\mu m}$ (0.15) and surface SW flux (17 Wm^{-2}). Under certain combination of surface reflection and aerosol properties, an unambiguous determination of aerosol optical depth is not possible (e. g., the almost perpendicular solid line for the Maldives aerosols when surface albedo is 0.3). The smaller TOA aerosol signal is due to the fact that increased

atmospheric backscattering from aerosols is largely offset by the reduced atmospheric transmission of surface reflection.

3) Surface irradiance is more sensitive to the variation of aerosol concentration than surface albedo.

The above effect is demonstrated by the steep solid and flat dotted lines in Figure 3.7. Due to the sensitivity of retrieving AOD under uncertain surface condition, putting a constraint on aerosol concentration rather than on the albedo is preferred when solving this inverse ill-posed problem.

In Figure 3.7, straight dotted lines represent the linear Eq. (2.7) which relates surface irradiance to the TOA reflection without dependence on the surface albedo. A large variation in the linear relationship coefficients (intercept and slope) is shown in Figure 3.8 for different aerosol types and concentrations. Similarly, for the net surface flux estimation, variation of the linear coefficients of Eq. (2.8) is shown in Figure 3.9. Due to the predominant dependence on atmospheric absorption, the coefficients exhibit large variability for absorbing aerosols. Results from these sensitivity tests indicate that incorporation of aerosol effects using a linear parameterization scheme should be used with caution since multiple aerosol parameters need to be included. A radiative transfer based satellite algorithm is preferred since a) lookup table technique is flexible and efficient to deal with large variation of aerosol properties; b) a complete estimate of surface SW fluxes (including spectrally resolved downward/upward/net total/direct/diffuse fluxes) can be provided by this approach. More details of this approach (UMD SRB model) will be presented in section 5.1.

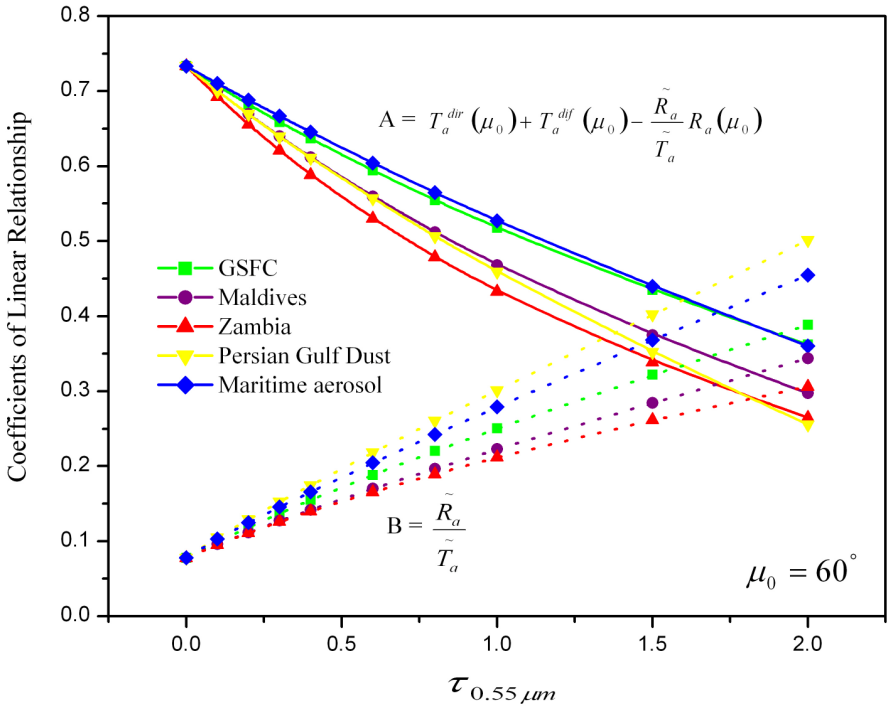

Figure 3.8 Variation of the coefficients of the linear relationship $t = A + Br$ (Eq. (2.4)) corresponding to different aerosol type and loading (aerosol optical depth at 0.55 μm).

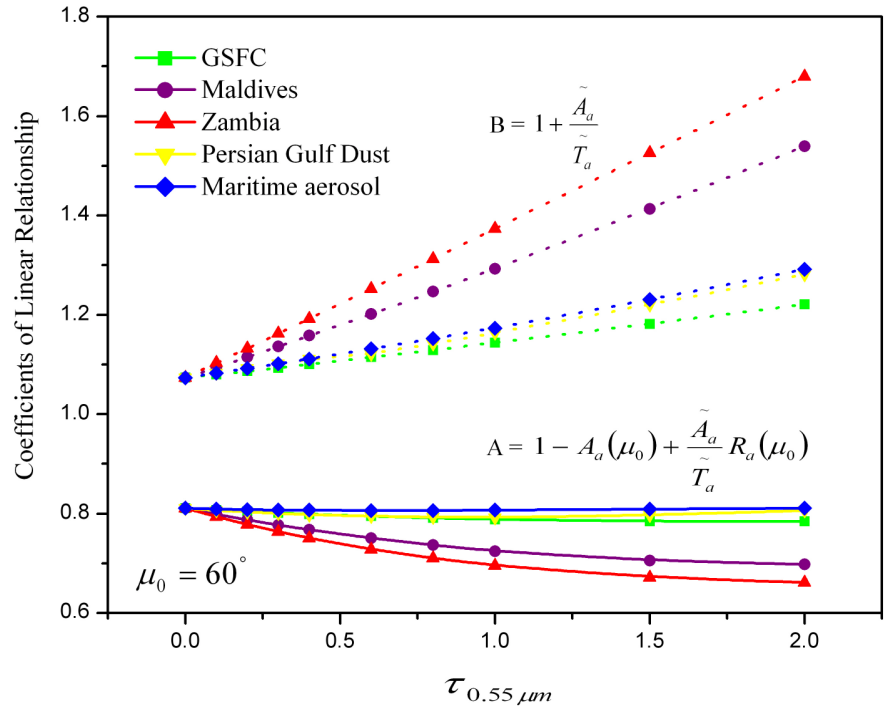

Figure 3.9 Variation of the coefficients of linear relationship $n = A - Br$ (Eq. (2.5)) corresponding to different aerosol type and loading (aerosol optical depth at 0.55 μm).

3.3 Summary

The major conclusions from the sensitivity tests of aerosol surface effects and their impacts on the relationship between TOA and surface radiation budget are:

1) Ambient aerosols could impose significant surface cooling effects, which have large variations associated with different aerosol concentrations, absorbing and scattering properties and need to be considered in surface SW radiation budget estimation.

2) Variation of aerosol properties affects the relationship between TOA and surface radiation budget. Uncertainties associated with aerosol and surface properties impose a great challenge for the derivation of surface fluxes from TOA reflection. Constraints on the aerosol properties are considered to be important for addressing this ill-posed problem due to larger sensitivity of surface downward fluxes to atmospheric conditions than to surface condition.

3) Linear relationships exist between TOA reflection and surface SW fluxes. However, given the difficulties related with the development of parameterization schemes, the radiative transfer method based on the lookup table technique is more suitable to incorporate the complex aerosol properties into the satellite-based SRB estimation.

Chapter 4: Description of global aerosol properties

In this chapter we develop a novel approach for obtaining global scale information on: monthly mean aerosol optical depth at 0.55 μm; single scattering albedo; asymmetry parameter, and the normalized extinction coefficient.

4.1 Aerosol optical depth at 0.55 μm

4.1.1 Introduction

Available observations of aerosol optical depth give accurate point information, but are limited in spatial extent. Satellites retrievals and model simulations have large-scale geographical coverage, but their accuracy has some limitations (section 2.1). A merged product from several sources could provide a better characterization of global AOD.

Optimal assimilation of AOD from multiple data sources requires reliable error statistics. Because of the limited scope of "ground truth", derivation of accurate estimates of error variance and covariance still remains a challenge. In this section, we develop a method for obtaining representative monthly grid area averaged clear-sky daytime AOD that capitalizes on the merits of several datasets [*Liu et al.*, 2005].

To derive the improved product, we use collocated monthly mean $\tau_{0.55\mu m}$ from MODIS retrievals, GOCART model simulations and AERONET ground measurements for a two-year period (March 2000 to February 2002).[4]. In the following section we discuss, sampling issues of the datasets; analyze the large-scale

[4] More detailed introduction of used data sets can be found in Appendix B.

variability of GOCART results and MODIS retrievals; introduce empirical combination schemes, and implement them.

4.1.2 Quality check and data preparation

(a) MODIS data

In this study we use Level-3 version 4 $1^\circ \times 1^\circ$ monthly mean AOD data derived from MODIS observations on Terra. MODIS retrievals are restricted by surface conditions and cloud presence. Therefore, daily count of "pixels" (spatial resolution of 10 km) within each grid cell varies from several to near two thousand. Most grids with limited retrievals are found in arid areas (bright surfaces), high latitudes (snow/ice cover) and the "roaring forties" of the Southern Hemisphere Ocean (glint effects). Temporal and spatial averages derived from low numbers of retrievals can have a sampling error. Yet, filtering of MODIS data based solely on a threshold of minimum daily pixel count can result in loss of valuable information.

Unfiltered MODIS data show large variation among adjacent grid points. We checked whether this variation is the consequence of under sampling. To this purpose, a discontinuity index was defined for each grid point as follows: local average and standard deviation were determined from a 3 by 3 array of points centered on the target grid; absolute difference between the target grid value and the local mean was calculated. The discontinuity index was set to be the absolute value of this difference minus the local standard deviation. Accordingly, a large discontinuity index indicates large variations around the central point. Subsequently, MODIS data were grouped based on the discontinuity index at a 0.1 bin-size, and average pixel daily count was calculated for each bin. Results of this analysis are

shown in Figure 4.1. It can be seen that a higher index is related to small number of pixel counts, namely, large discontinuity is associated with under-sampling. More than 97% of the grids have an index lower than 0.2, which implies that the discontinuity index could be used to improve the quality of the MODIS monthly mean AOD with minimum loss of data.

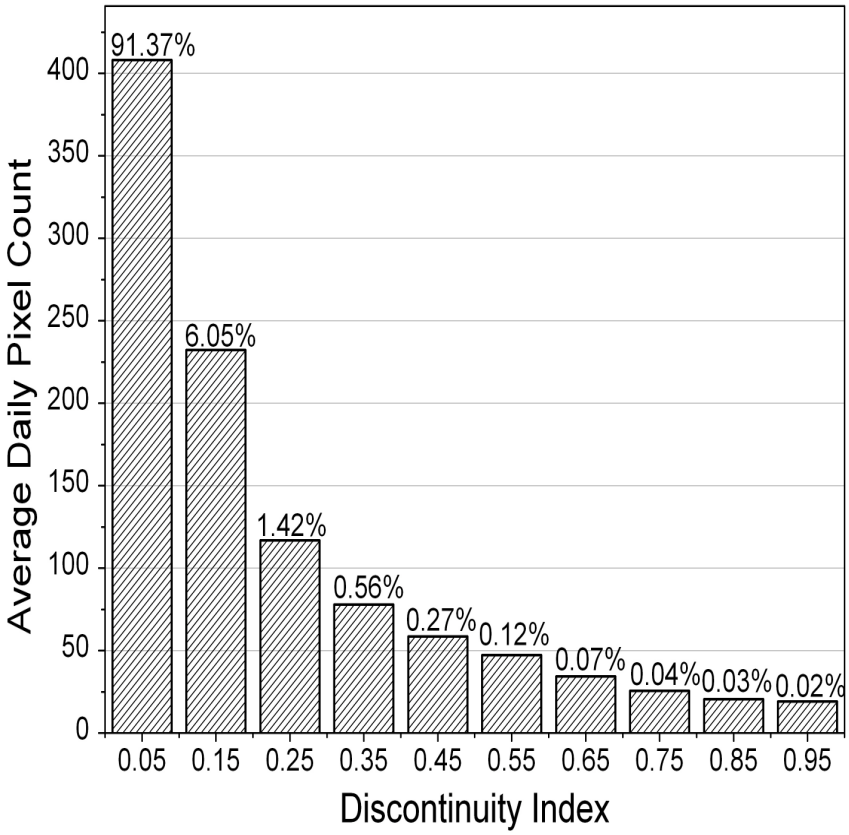

Figure 4.1 Average daily pixel count as a function of the discontinuity index for MODIS $1^\circ \times 1^\circ$ monthly mean AOD data. Percentage of grid points falling into each bin is labeled on the top of each column.

Table 4.1 Correlation (shaded) between the $1^{\circ} \times 1^{\circ}$ MODIS monthly mean AOD from Terra and Aqua (Jul. 2002 – Nov. 2003) at different combinations of minimum daily pixel count (MINDP: rows) and maximum discontinuity index (MAXDI: columns). Also shown is percentage of grids (un-shaded) that satisfy the requirement.

MINDP \ *MAXDI*	0.1	0.2	0.3	0.4	0.5	0.8	1.0	∞
0	0.919	0.897	0.873	0.857	0.846	0.822	0.814	0.791
	94.70%	98.29%	99.21%	99.57%	99.74%	99.90%	99.93%	100%
10	0.932	0.912	0.895	0.882	0.873	0.858	0.853	0.850
	92.21%	95.29%	96.03%	96.31%	96.44%	96.54%	96.56%	96.59%
20	0.935	0.917	0.900	0.888	0.880	0.869	0.865	0.850
	90.77%	93.64%	94.32%	94.57%	94.68%	94.76%	94.77%	94.79%
30	0.937	0.921	0.905	0.894	0.886	0.877	0.875	0.874
	89.45%	92.15%	92.79%	93.02%	93.11%	93.18%	93.19%	93.20%
50	0.941	0.926	0.913	0.903	0.898	0.892	0.891	0.890
	86.74%	89.17%	89.74%	89.92%	90.00%	90.04%	90.05%	90.05%
100	0.949	0.938	0.928	0.922	0.919	0.917	0.917	0.917
	79.55%	81.46%	81.86%	81.97%	82.00%	82.01%	82.02%	82.02%

Availability of overlapping MODIS retrievals from Terra and Aqua provides an opportunity for testing the applicability of this discontinuity index for data filtering. Since the local overpass time of Terra and Aqua (10:30 am and 1:30 pm) are within three hours, the monthly mean values from these two satellites should be consistent. If a large discrepancy exists, it could be attributed to sampling errors [*Kaufman et al.,* 2000]. Seventeen months (July 2002 to November 2003) AOD data are taken from both platforms and a linear correlation between the two datasets is calculated at different combinations of two thresholds (minimum pixel daily count and maximum discontinuity index) (Table 4.1). If all data are used (right-top corner of table), the correlation is only 0.79. The correlation is improved as the lower limit of pixel count increases (bottom of table) and upper limit of discontinuity index decreases (left of table). It is evident that a combination of these two criteria could

result in higher correlation while eliminating only a small amount of data. When the minimum pixel count is chosen to be 10 and maximum discontinuity index as 0.2, the correlation increases to 0.91 (less than five-percent of data being filtered out). After implementation of these criteria to the two-year Terra MODIS monthly mean AOD used in this study, more than 96.7 percent of the data remained.

To be compatible with the GOCART model output ($2.5^\circ \times 2^\circ$), MODIS data ($1^\circ \times 1^\circ$) are degraded to the same resolution using an area-weighted average. Data void grids (bright surface areas and high latitudes) are assigned interpolated/extrapolated values of AOD from neighboring grids based on the Poisson technique [*Oort and Rasmusson,* 1971; *Reynolds,* 1988]. The Poisson equation

$$\nabla^2 \phi = \rho \tag{4.1}$$

describes an equilibrium solution of a field (ϕ) which is balanced by the external forcing (ρ) and the diffusion process. Utilized is the characteristic that spatial distribution information (locations of the local minima and maxima and the rate of change) of a field could be prescribed in terms of ρ. The forcing terms for the data void grids are calculated from GOCART model results and MODIS data are taken as boundary values. In order to fill in gaps at high latitudes, GOCART data serve as external boundaries. Finite differences in the spherical coordinates and Successive OverRelaxing (SOR) method [*Press et al.,* 1995] are implemented to solve this second-order differential equation iteratively. The rationale behind this filling process is to preserve the magnitudes of AOD from MODIS and to utilize the spatial distribution information from GOCART. As an example of the effect of quality check and void-filling, one month (August 2000) of data from GOCART simulation

results, $1^\circ \times 1^\circ$ MODIS level-3 data, and error-filtered, void-filled, remapped global $2.5^\circ \times 2^\circ$ MODIS monthly mean AOD are shown in Figure 4.2.

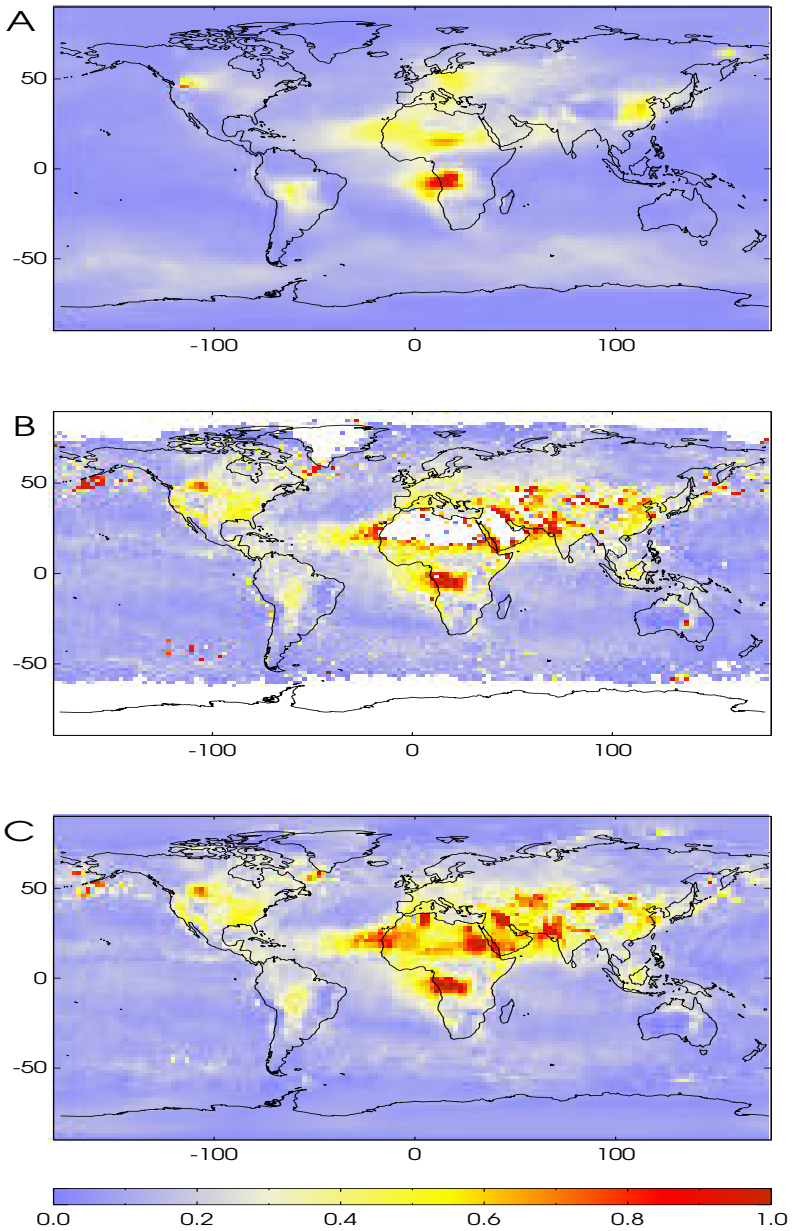

Figure 4.2 Monthly mean AOD at 0.55μm for August 2000. A) GOCART simulation results; B) MODIS Level-3 $1^\circ \times 1^\circ$ monthly means; C) error-filtered, void-filled, remapped $2.5^\circ \times 2^\circ$ MODIS data.

(b) AERONET data

Quality assured Level 2.0 data from AERONET are used to compute the monthly mean AOD values for each individual site (Figure 4.3). Optical depths at two adjacent wavelengths (0.5 and 0.67 μm) are used to interpolate to the standard wavelength (0.55 μm) based on the Ångström empirical expression [*Ångström*, 1929].

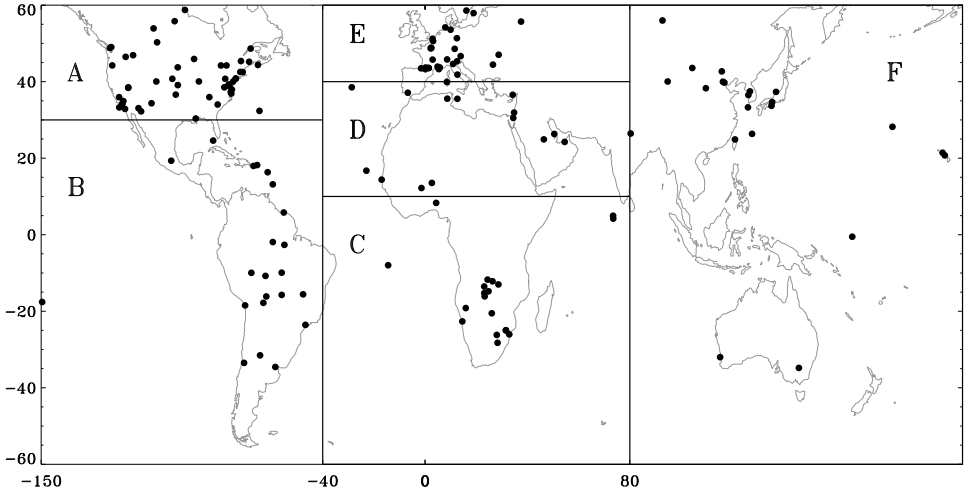

Figure 4.3 Location of AERONET stations used in this study; domains (A-F) for latter regional comparison are also specified.

While AERONET provides accurate point measurements, regional representation of monthly means is not assured [*Chin et al.,* 2002; *Kinne et al.* 2003]. Table 4.2 lists the monthly mean AOD of multiple AERONET stations collocated within the same $2.5^\circ \times 2^\circ$ grid cell. Differences of AOD from most of the collocated sites are small. Sub-grid variations larger than 0.1 exist in proximity to the source regions of biomass burning (Ndola and Solwize); dust outbreaks (Beijing and XiangHe) and local pollutions (Penn_State_Univ, GSFC and MD_Science_Center). Since most of the time aerosol concentrations vary at a synoptic scale, AERONET monthly mean AOD is considered as a good estimate of grid mean value, and used for

evaluation of grid averaged products [*Chin et al.,* 2000; *Yu et al.* 2003; *Kinne et al.* 2003].

Table 4.2 Monthly mean AOD of AERONET sites located within the same $2.5^{\circ} \times 2^{\circ}$ grid cell: a) from March 2000 to February 2001; b) from March 2001 to February. 2002. Grid cells with sub-grid variation larger than 0.1 are shaded.

a)	Mar 2000	Apr 2000	May 2000	Jun 2000	Jul 2000	Aug 2000	Sep 2000	Oct 2000	Nov 2000	Dec 2000	Jan 2001	Feb 2001
GSFC	0.111	0.142	0.294	0.326	0.299	0.338	0.152	0.130	0.075	0.071	0.076	0.113
MD_Science_Center	0.119	0.156	0.309	0.334	0.291	0.380	0.150	0.150	0.079	0.071	0.087	0.106
Oyster	0.104	0.113	0.278	/	/	/	/	/	/	/	/	/
Wallops	0.102	0.169	0.255	/	/	/	/	/	/	/	/	/
Rogers_Dry_Lake	0.073	0.096	0.100	/	0.087	/	/	/	/	/	/	/
UCLA	0.140	0.165	0.158	/	/	/	/	/	/	/	/	/
MISR-JPL	/	/	/	/	0.174	/	/	/	/	/	/	/
Creteil	/	/	/	/	0.158	0.194	/	0.104	/	/	/	/
Palaiseau	/	/	/	/	0.153	0.185	/	0.087	/	/	/	/
Paris	/	/	/	/	0.152	0.107	/	/	/	/	/	/
Mongu	/	/	/	/	/	0.258	0.717	0.476	/	/	/	/
Senanga	/	/	/	/	/	0.223	0.692	0.513	/	/	/	/
Ndola	/	/	/	/	/	0.370	0.650	/	/	/	/	/
Solwezi	/	/	/	/	/	0.520	0.834	/	/	/	/	/

b)	Mar 2001	Apr 2001	May 2001	Jun 2001	Jul 2001	Aug 2001	Sep 2001	Oct 2001	Nov 2001	Dec 2001	Jan 2002	Feb 2002
GSFC	0.100	0.210	0.272	0.368	0.187	0.516	0.155	0.109	0.124	0.065	0.058	0.079
MD_Science_Center	0.109	0.231	0.269	0.388	0.204	0.506	0.151	0.119	0.133	0.073	0.058	0.085
Penn_State_Univ					0.319	0.406	0.106					
Beijing	0.518	0.891	/	/	/	/	/	/	/	/	/	/
XiangHe	0.524	0.747	/	/	/	/	/	/	/	/	/	/
Rogers_Dry_Lake	/	/	/	/	/	/	/	/	/	/	/	0.040
UCLA	/	/	/	/	/	/	/	/	/	/	/	0.102
Avigon	/	/	/	0.169	0.187	/	/	/	/	/	/	/
Marseille	/	/	/	0.165	0.207	/	/	/	/	/	/	/
Realtor	/	/	/	0.156	0.198	/	/	/	/	/	/	/
Vinon	/	/	/	0.154	0.166	/	/	/	/	/	/	/
GISS	/	/	/	/	0.162	0.380	0.153	/	/	0.111	0.105	0.080
Philadelphia	/	/	/	/	0.243	0.441	0.154	/	/	/	/	/
CCNC	/	/	/	/	/	/	/	/	/	0.095	0.082	0.077
Aire_Adour	/	/	/	/	/	/	0.166	0.069	/	/	/	/
Tarbes	/	/	/	/	/	/	0.167	0.098	/	/	/	/
Big_Meadows	/	/	/	/	/	/	0.112	0.075	/	/	/	/
SERC	/	/	/	/	/	/	0.178	0.105	/	/	/	/
Osaka	/	/	/	/	/	/	/	/	/	0.131	0.021	0.022
Shirahama	/	/	/	/	/	/	/	/	/	0.093	0.013	0.018

/ : Temporal collocated measurements are not available.

AERONET monthly mean station AOD values are affected by under-sampling. Stations are marked as questionable if within one month, the number of total measurements is less than 100 and days in operation are fewer than five. A one year comparison among collocated AERONET, GOCART and MODIS data is presented in Figure 4.4; region grouping is described in Table 4.3. During March 2000 to February 2001, three measurements are eliminated because they show much higher values than MODIS and GOCART data (Dakar on August 2000; NCU Taiwan on October 2000; Mexico City on November 2000). Similar comparison was performed for 2001 and two unrealistic AERONET monthly mean values were filtered out (Yulin on April 2001 and Philadelphia on June 2001). Data from Mauna Loa, located 3.4 km above sea level, are not used in the analysis since the site is used for calibration of the CIMEL instruments [*Holben et al.*, 1998]. Generally, in terms of magnitude, MODIS retrievals appear to be the highest among the three, in particular in western North America during the spring/summer time and in dust dominated regions (region D). This can be partially attributable to inaccurate estimation of surface reflectance [*Chin et al.*, 2004] and insufficient knowledge of the optical properties of non-spherical particles [*Levy et al.*, 2003].

(c) Temporal sampling differences

Some intrinsic differences in temporal coverage remain in the data used. AERONET data represent the clear-sky daytime average; GOCART model reports all-sky all-time mean value; while monthly mean data from MODIS onboard Terra represents the clear- sky pre-noontime value. Inclusion of aerosols under cloudy

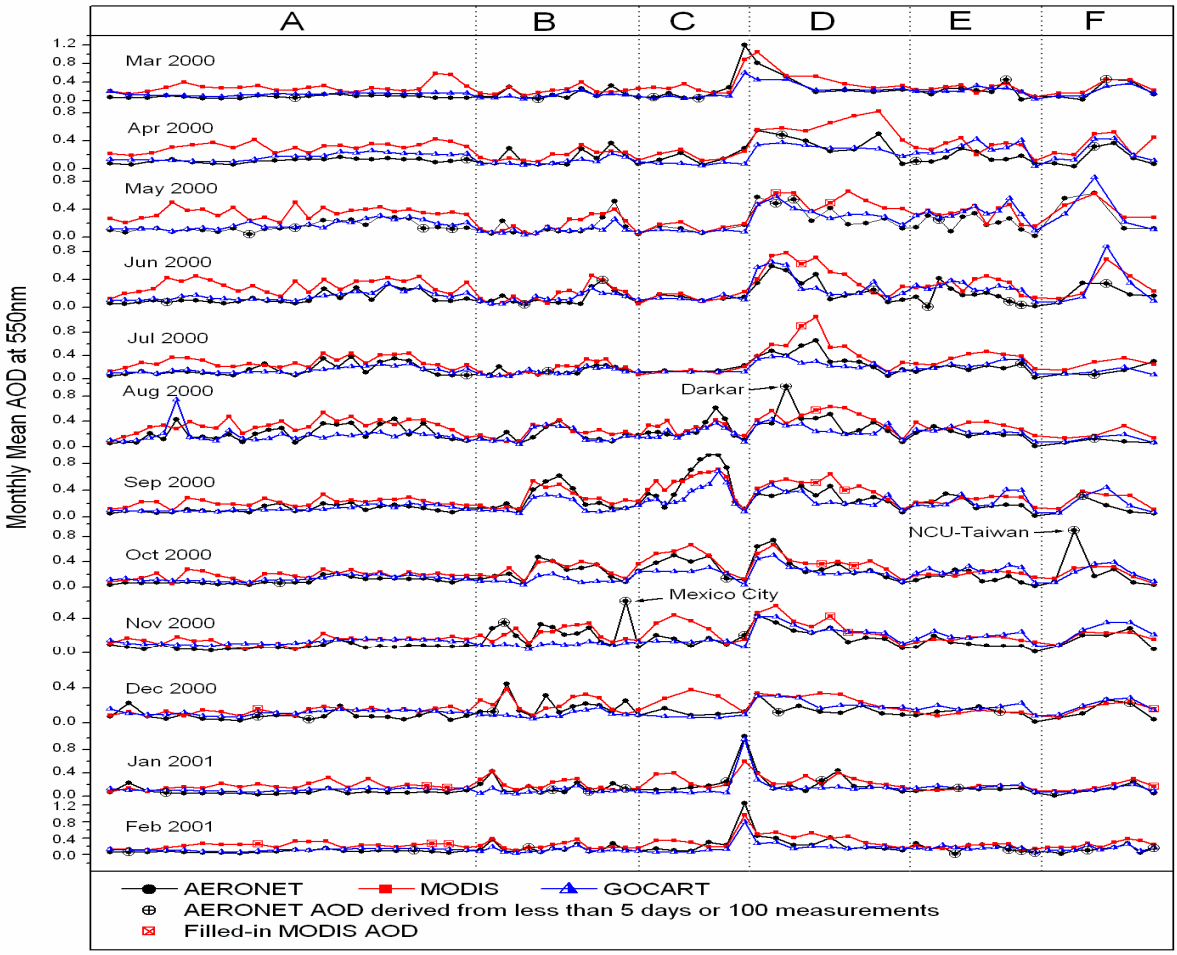

Figure 4.4 Comparison of monthly-mean AOD from GOCART, MODIS and AERONET for one-year period (March 2000–February 2001). The x-axis represents the various stations in each sub-region. The names of under-sampled AERONET sites are also given (these data are eliminated).

Table 4.3 Regions selected for the monthly mean AOD comparison from MODIS, GOCART and AERONET.

Region Index	Domain		Major aerosol types	Direction shown in Figure 3
A	150° W-40° W	30° N-60° N	Urban/Industrial	West to East
B	150° W-40° W	60° S-30° N	Biomass Burning	South to North
C	40° W-80° E	60° S-10° N	Biomass Burning	
D	40° W-80° E	10° N-40° N	Dust	
E	40° W-80° E	40° N-60° N	Urban/Industrial	
D	80° E-150° W	30° N-60° N	Dust Urban/Industrial	West to East

condition might introduce a bias relative to the clear-sky measurements. Quantitative estimation of such bias is difficult due to the compensating effects of secondary aerosol production (sulfate), hygroscopic growth and wet deposition [*Chin et al.*, 2002]. Possible bias of MODIS monthly means can be attributed to AOD diurnal variations. *Kaufman et al.* [2000] found that measurements at MODIS overpass time represent quite well clear-sky daytime averages. Other studies show detectable diurnal variability in urban/industrial areas (10-40%) [*Smirnov et al.*, 2002], and Southern African biomass burning region (25%) [*Eck et al.*, 2003]. Scatter plots of AERONET monthly mean AOD against the GOCART and MODIS data are shown in Figure 4.5. For the cases of AERONET AOD less than 0.6, MODIS retrievals have a positive bias, while biases associated with GOCART simulations are not significant. Confident estimates of the deficiencies in both data sources would be possible only when sampling effects are reliably estimated.

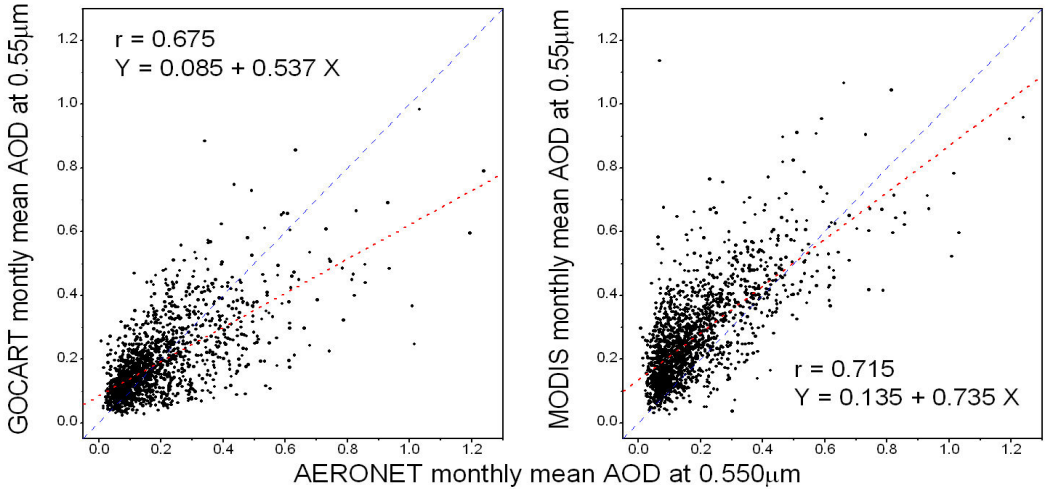

Figure 4.5 Scatter plots of AERONET monthly mean AOD at 550 nm against GOCART model simulations (left) and MODIS retrievals (right).

4.1.3 Comparison of MODIS and GOCART variability

In order to compare the spatial and temporal variability of large-scale MODIS and GOCART data, anomalies (difference between monthly means and total twenty-four months average) are calculated. Coupled analysis is performed based on the Singular Value Decomposition (SVD) method, which is a powerful tool to identify pairs of spatial patterns (modes) with the maximum temporal covariance between the two fields [*Bretherton et al.*, 1992]. It has been widely applied to meteorological data for exploring the coupled relationship between two physically related variables [*Wallace et al*., 1992; *Wang and Ting,* 2000]. If the two fields have large common signals and are joined-analyzed using the SVD method, the spatial distributions of the modes and the temporal variation of the expansion coefficients are expected to be similar. The contribution of each pair of modes is described by the squared covariance function (SCF), defined as:

$$SCF_i = \sigma_i^2 \Big/ \sum_{j=1}^{M} \sigma_j^2 \qquad (4.2)$$

where σ_i is the *i*-th singular value and M is the total number of coupled pairs. In the coupled GOCART and MODIS anomaly SVD analysis, more than 95% of squared covariance is explained by the first three leading modes, suggesting that most of the variation signal is contained in these modes. The temporal evolution of MODIS and GOCART data is similar (Figure 4.6), namely, mode 1 and mode 2 represent a strong annual cycle, and mode 3 describes the seasonal variation. The amplitude of the MODIS time series appears to be larger than that of GOCART, due to the larger variance associated with the satellite retrievals.

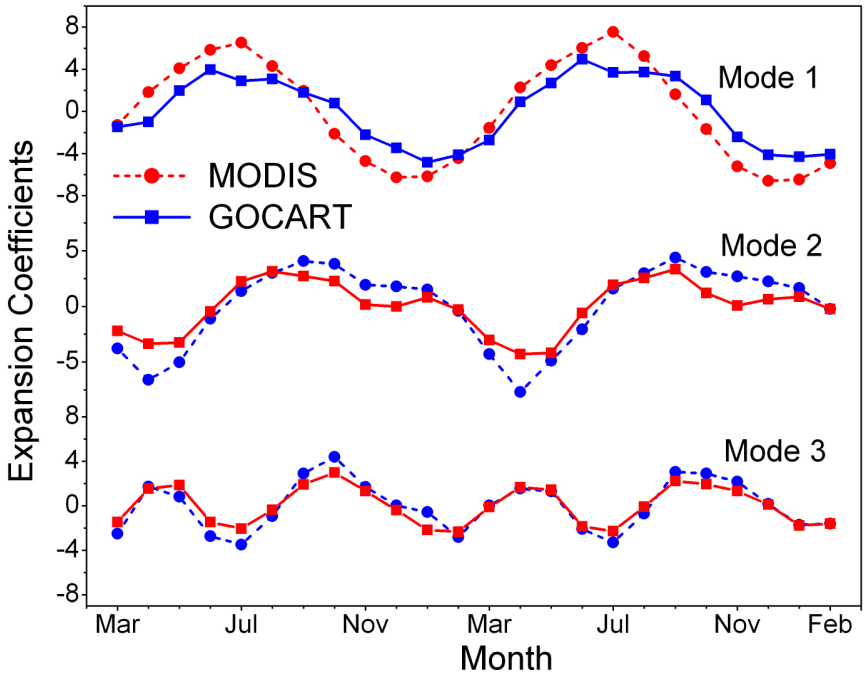

Figure 4.6 Temporal variations of the expansion coefficients (time series) of the three SVD leading modes of MODIS retrievals and GOCART simulations.

The first three leading coupled modes are present in Figure 4.7. Pairs of modes display similar spatial distribution; large scale prominent features such as biomass burning in southern hemisphere, tropical Africa and south-east Asia; dust over Northern Africa, Asia and transport over the tropical Atlantic Ocean are in good agreement.

Missing MODIS data over part of Northern Africa and Saudi Arabia are filled based on GOCART spatial information. The filled desert area is less than 2% of the total analysis domain, yet, nearly 9% of the total variance is found in this region. A question arises whether this data filling has a large effect on the anomaly analysis. Sensitivity coupled SVD analysis performed with unfilled MODIS data shows little

difference. The reason could be attributed to the large outflow areas over ocean and nearby dark land surfaces, which maintain strong signals from the data void regions.

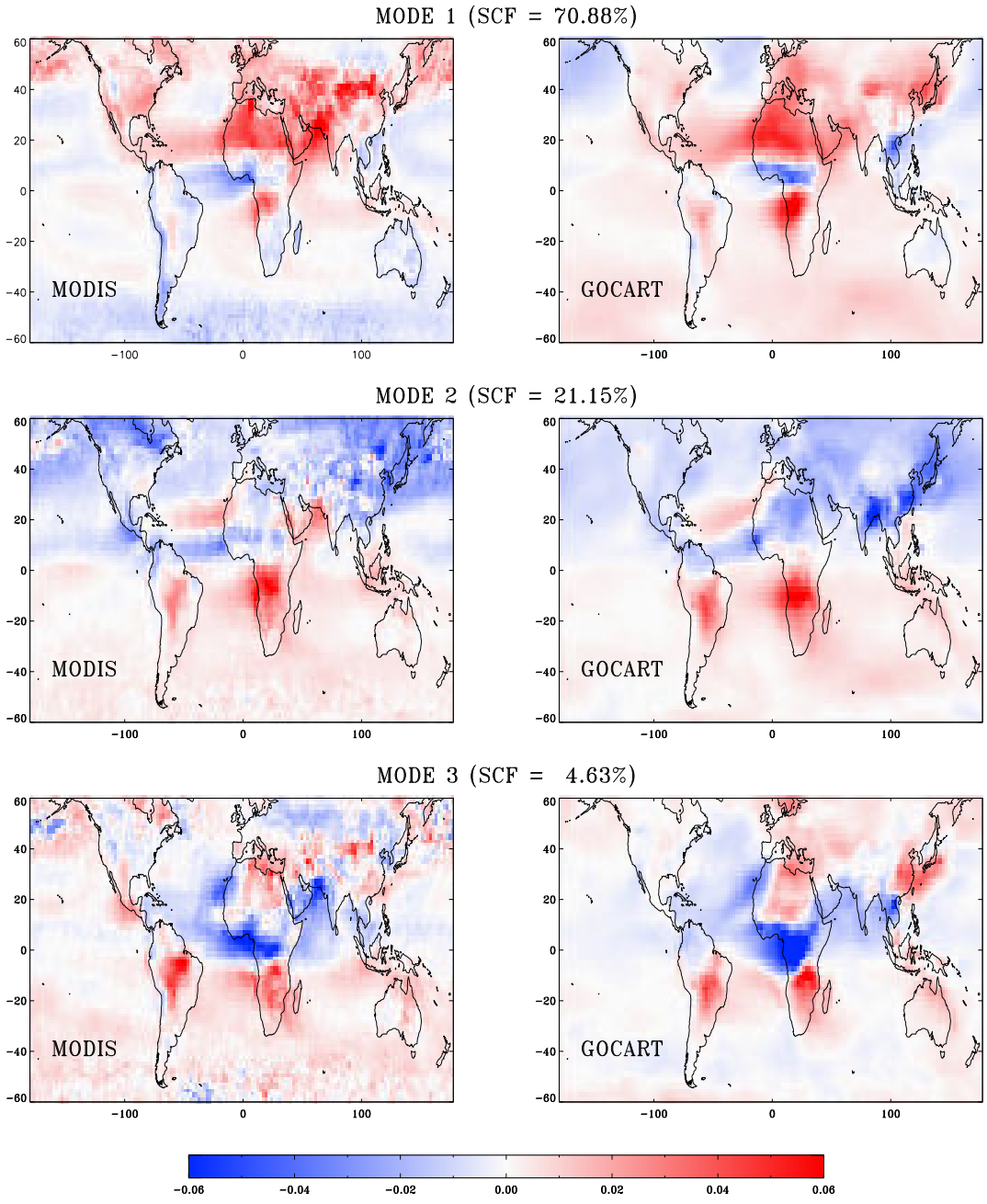

Figure 4.7 Three normalized leading modes of coupled SVD analysis of MODIS retrievals and GOCART simulations.

The SVD coupled analysis indicates that in spite of the differences in temporal coverage (clear-sky snapshot vs. all-sky all-time) the variability information from MODIS retrievals and GOCART model results is in good agreement. These results are the basis for utilizing the spatial variation information from both data sets to distribute AERONET data at a global scale.

4.1.4 Combination method

To combine the AERONET, MODIS and GOCART AOD monthly mean data, first the global two year averages are computed, and then the spatial and temporal variations are constructed using the truncated EOFs fitting method. A schematic description of the empirical combination scheme is presented in Figure 4.8.

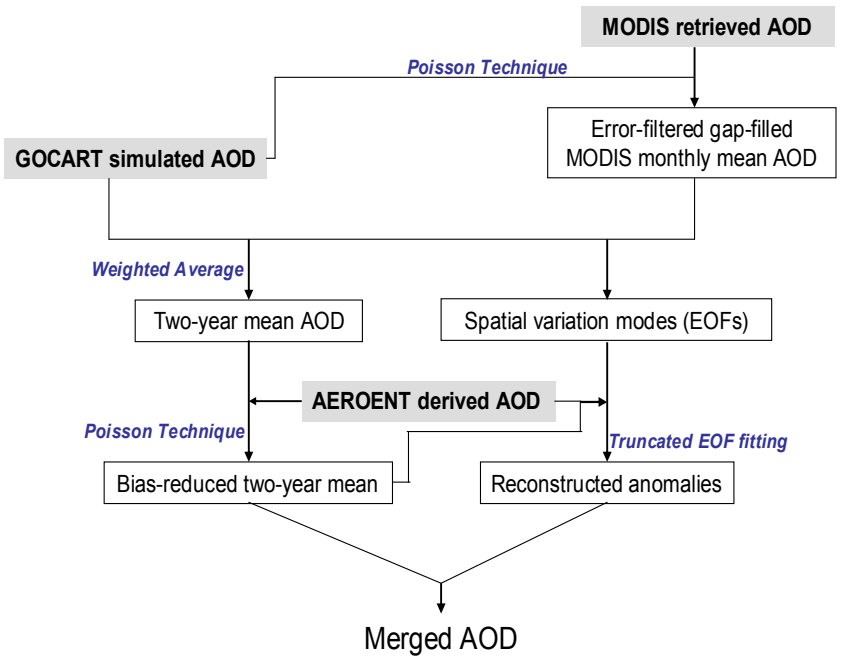

Figure 4.8 Schematic description of the combination scheme to construct global monthly mean clear-sky daytime average AOD from GOCART simulations, MODIS retrievals and AERONET measurements.

(a) Two-year averaged AOD

Minimum variance estimation method [*Daley*, 1991] is usually used to average two data sets with weights determined as:

$$w_1 = \frac{e_2^2}{e_1^2 + e_2^2} \qquad w_2 = \frac{e_1^2}{e_1^2 + e_2^2} \tag{4.3}$$

where w is the weight and e^2 is the unbiased-error variance [*North et al.,* 1991; *Huffman et al.,* 1995; *Xie and Arkin*, 1996]. To estimate the respective averaging weights for GOCART and MODIS two-year mean AOD, data from Figure 4.5 are binned at 0.02 AOD units based on AERONET measurements. Inside each bin the mean value contains the bias and the corresponding standard deviation can be regarded as the square root of unbiased-error variance. The analysis result and the linear fitting of the mean value and the standard deviations are shown in Figure 4.9.

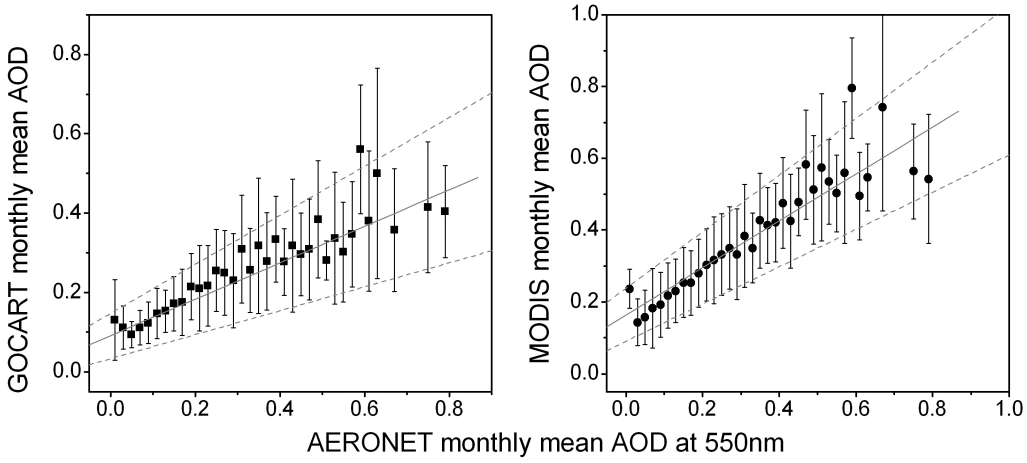

Figure 4.9 Estimation of unbiased "error" variance of GOCART (left) and MODIS (right) data. GOCART and MODIS monthly mean AODs are binned into 0.02 bins according to AERONET data (X axis). Within each bin, mean value and standard deviation are calculated. Linear fits of mean values and standard deviations are performed separately. Solid lines represent mean values fitting; dotted lines are the standard deviation fitting superposed on the solid line. Fitted standard deviation is $(0.057 + 0.158\tau)$ for GOCART and $(0.074 + 0.134\tau)$ for MODIS.

Based on this analysis, unbiased error variances are set to be $(0.057 + 0.158\tau)^2$ for GOCART and $(0.074 + 0.134\tau)^2$ for MODIS. Consequently, fractional contribution (weight) of GOCART data monotonously decreases from 0.63 to 0.48 as τ increases from 0 to 1.

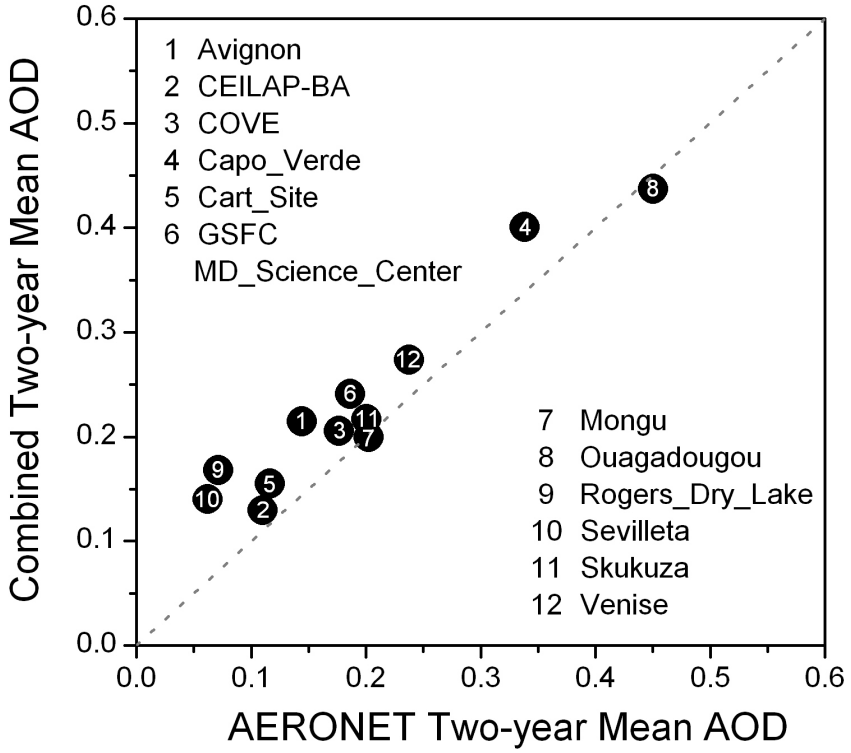

Figure 4.10 Scatter plot of AERONET two-year mean AOD (thirteen stations, twelve grid point values) against weighted average of GOCART and MODIS two-year mean AOD. Indices and names of the stations are labeled on the plot.

Figure 4.10 presents a comparison of the combined two-year average with data from thirteen AERONET stations (twelve grid values because GSFC and MD_Science_Center are located within one cell and averaged). The merged two-year means are generally larger than the AERONET observations (difference is below 0.1). To possibly reduce the remaining bias, Poisson technique is used: twelve grid points serve as anchor points (internal boundaries) and the weighted averaged data at

the Polar Regions are kept as external boundary values. We assume that these AERONET long-term averages represent the area average and that a small bias remains in the merged data at high latitude. Forcing terms at the remaining points are calculated from the weighted averaged data. The rationale of this procedure is that linear bias contained in the original field could not affect the value of the second derivative (forcing term ρ in Poisson equation). Using accurate values at some anchor grid points and keeping the original forcing terms at the remaining points, reconstruction of the field can reduce constant and linear bias from the original data. This technique is well established in the assimilation of SST and precipitation [*Reynolds,* 1988; *Reynolds and Marsico*, 1993; *Reynolds and Smith*, 1994; *Xie and Arkin*, 1996].

Figure 4.11 shows the two-year mean AOD from GOCART, MODIS (void-filled) and the final result within (60° S, 60° N). Displayed is also the effect of the Poisson technique. GOCART data (with spatially averaged AOD being 0.13) are smaller than MODIS results (0.19), and weighted average result lies in between (0.16). The Poisson technique has an overall reducing effect (Figure 4.11d) due to general overestimation by the two-year weighted average when compared with AERONET (Figure 4.10). This leads the final average value of (0.13) to be close to GOCART simulations. In the two-year average AOD (Figure 4.11c), large values are found in Africa and Asia, mostly from mineral dust, combined with biomass burning and industrial pollution. Evident is also the westward propagation from North Africa and eastward transport from East Asia. AODs over South America are somewhat lower than over South Africa, perhaps due to the shorter and less intense periods of

the burning season [*Duncan et al.,* 2003]. Urban/industrial aerosol signals are detected in the Eastern US and Europe.

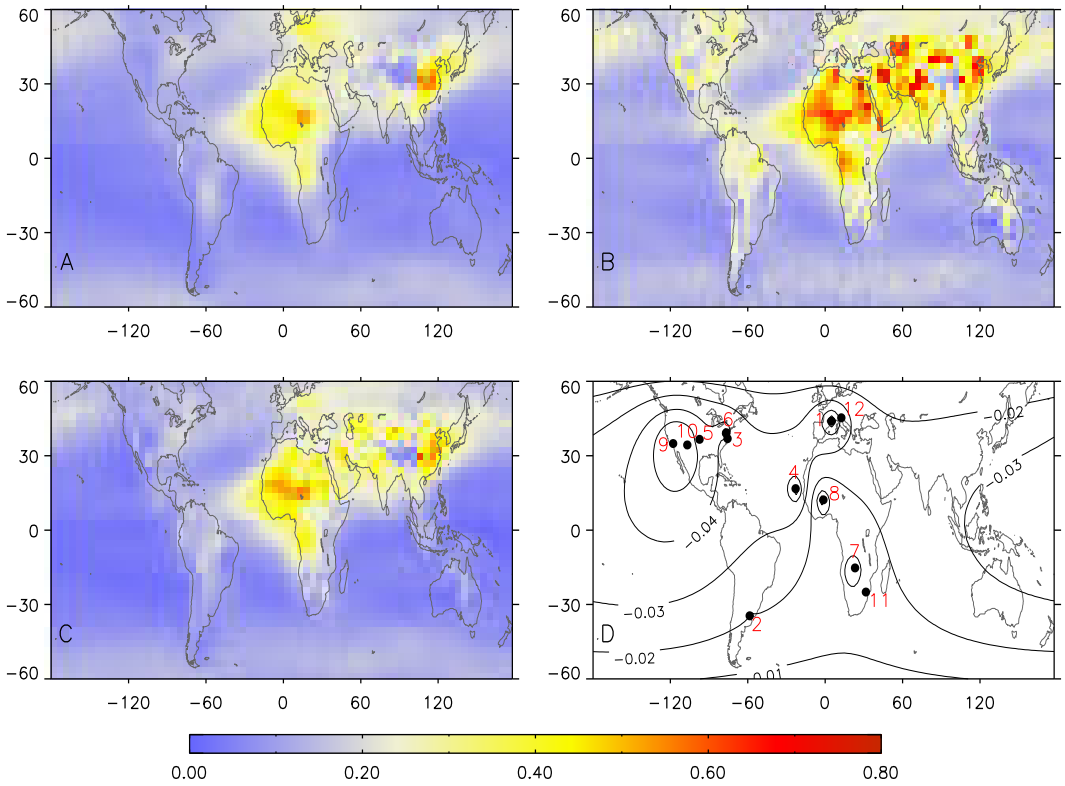

Figure 4.11 Estimation of two-year averaged AOD based on the weighted average of GOCART and MODIS data and Poisson technique: A) GOCART two-year average; B) MODIS two-year average calculated from the void-filled dataset; C) final result; D) effect of the Poisson technique; locations of AERONET stations are shown using same indices as in Figure (4.10).

(b) Spatial and temporal variations

Propagating the AERONET information at global scale is difficult largely due to the limited number of stations and the inhomogeneous and anisotropic AOD spatial distribution which might not be reliably described by simple modeled covariance functions. Truncated EOF fitting is more suitable for this case because of its ability to distribute sparse data to the large scale in a more realistic and coherent manner.

This approach is used to reconstruct historical SST and model data assimilation [*Smith et al.*, 1996; *Kaplan et al.*, 1997; *Ballabrera et al*., 2001].

Denoting the leading EOF modes computed from MODIS and GOCART anomalies as E, and AERONET anomalies as O:

$$O = \mathrm{H}E\mu + d \tag{4.4}$$

where μ is the expansion coefficient; H is the observation operator which converts the data from grid space to the observation locations; and d is the difference between the observation anomaly and the constructed value. Best estimation of the expansion coefficient μ in a least square sense requires:

$$\frac{\partial\left(d^T d\right)}{\partial\mu} = 0 \tag{4.5}$$

this equals to:

$$\left(\mathrm{H}E\right)^T\left(\mathrm{H}E\right)\mu = \left(\mathrm{H}E\right)^T O \tag{4.6}$$

μ is derived by solving this linear system and the constructed anomalies are calculated from $\mathrm{H}E\mu$.

We assume that the quality checked AERONET monthly means of AOD could be regarded as the grid average, so the observation operator H is simply mapping the stations to the grid points where they are located. AERONET anomalies O are calculated relative to the above estimated two-year average AOD values at the corresponding grids. Leading modes E are derived from area-weighted EOF analysis, performed on the composite MODIS and GOCART anomalies (i.e., concatenate two data sets together). Figure 4.12 shows the percentage of the total variance explained by each mode. More than 70% contribution comes from the first

5 modes, which indicates that large amount of variation signals are shared by the two datasets. In order to fit the leading EOFs to the measurements month by month, relative significance of each mode must be determined on a monthly basis. The leading sequence of the EOFs is determined by:

$$sig_{i,t} = \frac{\left|\sqrt{\sigma_i} T_{i,t}\right|}{\sum_{i=1}^{M} \left|\sqrt{\sigma_i} T_{i,t}\right|} \tag{4.7}$$

where the index i represents the ith mode, and t denotes the time; T is the normalized expansion coefficients (temporal amplitude) from the EOF analysis and σ is the eigenvalue (explained variance).

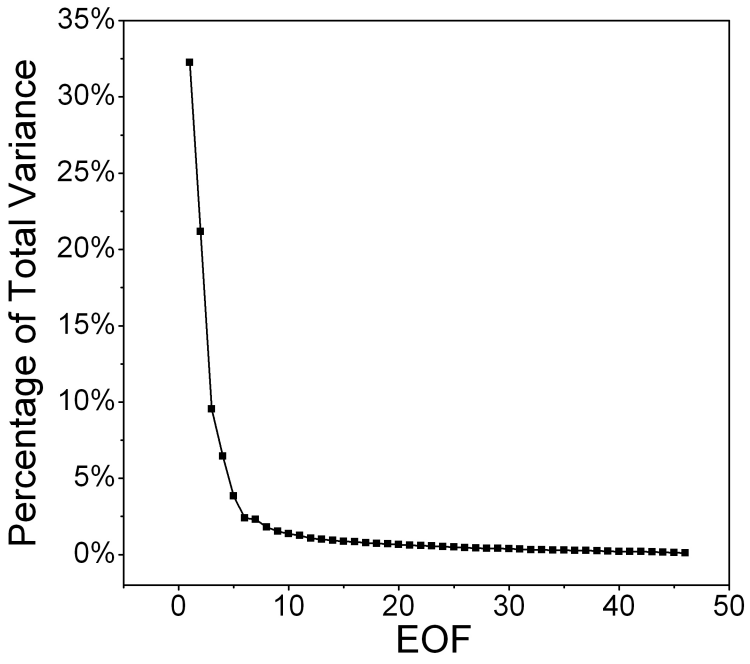

Figure 4.12 Percentage of the total variance explained by each mode, calculated from the joint EOF analysis of the composite MODIS and GOCART anomalies.

Before implementing the EOFs fitting, the following questions require answers: 1) how many modes are necessary to achieve satisfactory result? 2) Is this method robust in respect to the observational and sampling errors in the AERONET data?

To test how many EOFs are needed for capturing significant signals and for testing the performance of truncated EOF fitting, the following sensitivity test is designed: AERONET anomalies are replaced with the MODIS/GOCART anomalies at the grid points where AERONET stations are located. The result of such simulated EOF fitting will be compared with the original MODIS and GOCART anomaly fields to check whether significant signals can be reconstructed. To make a quantitative estimate of the resemblance between two fields, the two-dimension data array is reformed to a vector, and the vector cosine is computed as a similarity index. The cosine value of 0.71 represents a projection angle of 45°, which is served as an acceptable lower bound for two spatially similar fields. The robustness of the fitting, which is determined by the condition number of the matrix $(\mathrm{H}E)^T(\mathrm{H}E)$, is also calculated. Larger condition number will make the linear system ill conditioned and very sensitive to small change of observed values, thus unfavorable for the fitting process.

Test results for August 2000 are shown in Figure 4.13. Condition number and the similarity (vector cosine) between the fitting results and the simulated field are displayed as a function of the number of EOFs being used. Test results for the other months are similar. Large-scale spatial patterns can be successfully reproduced with few EOFs, resulting in vector cosine larger than 0.8. As more modes are being

included, the similarity increases; however, the condition number also becomes larger.

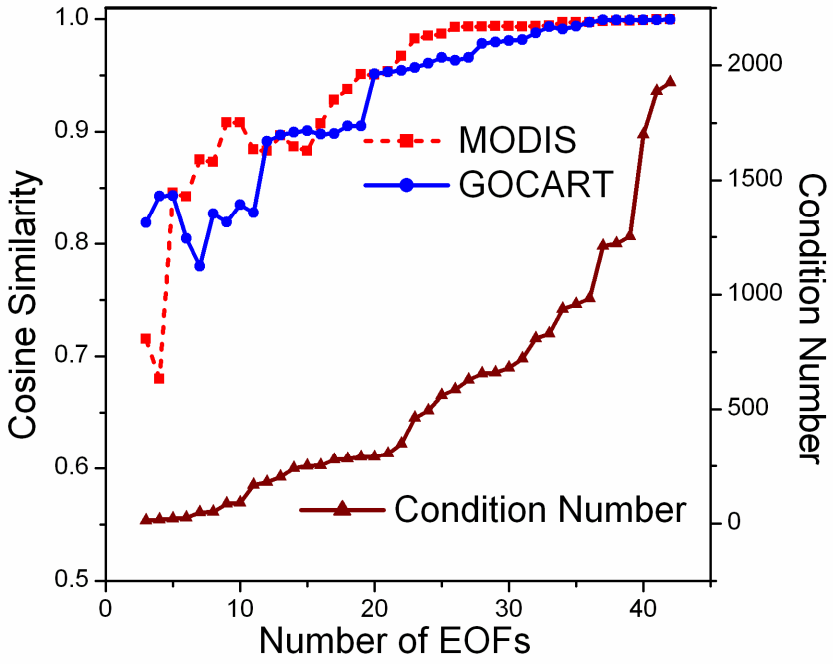

Figure 4.13 Condition number and the similarity (vector cosine) between the fitted results and the simulated field (MODIS and GOCART) as a function of the number of EOFs being used (August, 2000).

The following empirical rules are followed to decide how many leading EOFs to use: sufficient number of modes that are needed to capture significant spatial variability information; modes with small and comparable eigenvalues are usually degenerated and might be contaminated by errors [*North et al.*, 1982]; the condition number should be relatively small. As a compromise, a threshold value of 0.02 of the relative significance value $sig_{i,t}$ is used to truncate the EOF modes for each month. Table 4.4 gives the number and index of the leading modes being used and the number of grid points with available AERONET measurements.

Table 4.4 Number and index of the leading modes; number of grid points with available AERONET values used in the EOF fitting for each month.

Time	Leading EOFs used in the fitting		Number of grid points with AERONET measurements
	Number	Index	
2000_MAR	7	1 2 3 4 5 6 7	61
2000_APR	7	1 2 3 4 6 7 8	60
2000_MAY	8	1 2 3 4 5 7 8 9	69
2000_JUN	6	1 2 3 4 5 6	72
2000_JUL	9	1 2 3 4 5 6 8 11 13	69
2000_AUG	8	1 2 3 4 5 6 7 13	74
2000_SEP	5	1 2 3 4 5	75
2000_OCT	8	1 2 3 4 5 7 8 10	69
2000_NOV	10	1 2 3 4 5 7 8 9 10 12	66
2000_DEC	6	1 2 3 4 5 6	59
2001_JAN	6	1 2 3 4 5 7	63
2001_FEB	5	1 2 3 4 5	69
2001_MAR	8	1 2 3 4 5 6 7 8	72
2001_APR	8	1 2 3 4 5 7 9 15	69
2001_MAY	6	1 2 3 4 7 8	79
2001_JUN	8	1 2 3 4 5 6 8 10	83
2001_JUL	9	1 2 3 4 5 6 8 9 11	82
2001_AUG	7	1 2 3 4 5 8 10	87
2001_SEP	6	1 2 3 4 5 6	84
2001_OCT	6	1 2 3 4 6 7	78
2001_NOV	6	1 2 3 4 5 7	72
2001_DEC	5	1 2 4 5 7	68
2002_JAN	5	1 2 3 4 5	69
2001_FEB	5	1 2 3 4 5	59

(c) Combination results

Truncated EOF fitting is performed to construct the anomaly field for the time period March 2000 to February 2002 over the domain of (60° S, 60° N). Monthly mean AOD are obtained by adding the anomaly back to the two-year average. Poisson equation is used to fill in the high latitude region as used in the MODIS data void filling. Large-scale spatial and temporal variations are well represented in the combined results (Figure 4.14).

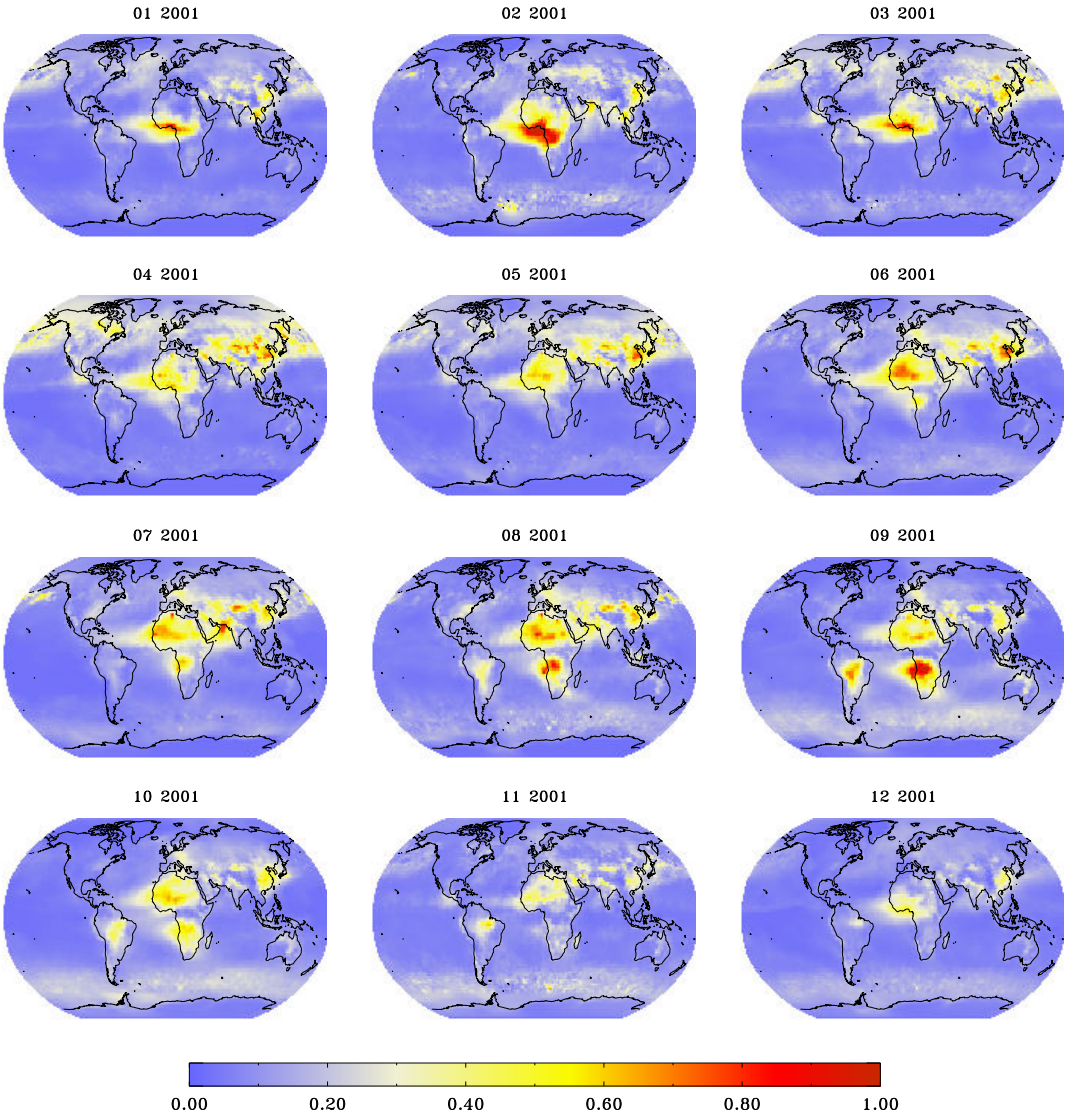

Figure 4.14 Estimation of global monthly-mean clear-sky daytime AOD at 0.55 μm from the proposed combination of AERONET, GOCART and MODIS data for the year 2001.

Minimum least-square fitting cannot reproduce the exact AERONET AOD values and quality of combination results can deteriorate if there is large incompatibility among the spatial and temporal variations associated with AERONET data and joint analysis of MODIS and GOCART results. To evaluate the merged

AOD, scatter plot of the combination results against AERONET data is presented in Figure 4.15. Improved correlation (compared with Figure 4.5) and relatively condensed distribution along the one-to-one line are observed. Dispersion and a small negative bias of the merged AOD can be caused by the different temporal coverage of GOCART and MODIS data, sub-grid scale variability in the AERONET observations, loss of small-scale signals due to the truncation of EOFs and inaccurate long-term average from which AERONET anomalies are calculated.

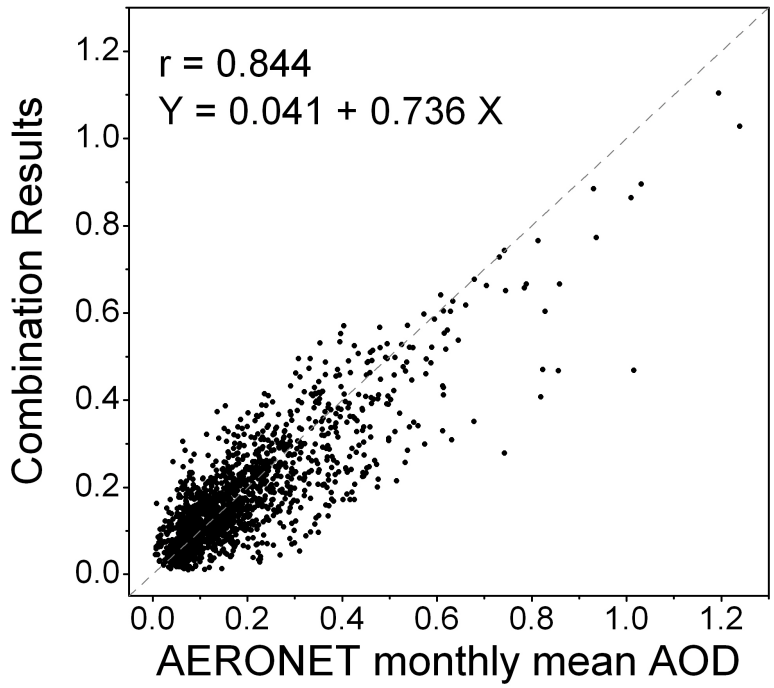

Figure 4.15 Scatter plot of AERONET monthly mean AOD against the combination results.

To assess the differences between the combination results and GOCART/MODIS data and to evaluate regional performance, comparison is performed at six regions as specified in Table 4.3 (Figure 4.3). Figure 4.16 displays

the inter-comparison between the data sets and scatter plots of each against AERONET measurements. Only grid points with MODIS retrievals are selected.

Region A: Merged AOD agrees well with GOCART in spring and summer but is lower than both datasets in autumn and winter. In general, combination results give higher correlation with AERONET.

Region B: Combination results display a negative bias. MODIS data agree well with AERONET while GOCART tends to have a low bias (will not improve the combination results here).

Region C: Combination results shows good agreement with AERONET and regionally averaged combination values are generally between GOCART and MODIS.

Region D: Combination results agree better with GOCART than with MODIS results. Underestimations exist for some high AERONET AOD cases. This region has the largest known aerosol burden.

Region E: Both GOCART and MODIS tend to overestimate the AOD. While the correlation is not improved for the combination results, positive bias is largely reduced.

Region F: Combination results show a high degree of agreement with GOCART data. MODIS data display a positive bias in the small to medium range of AOD, however, they agree better with AERONET at the high end of values.

Overall, merged results are closer to GOCART than to MODIS. This could be due to the fact that in the range of low and medium AOD, GOCART data do not show a significant bias, while MODIS data have a positive bias (Figures 4.5). Since

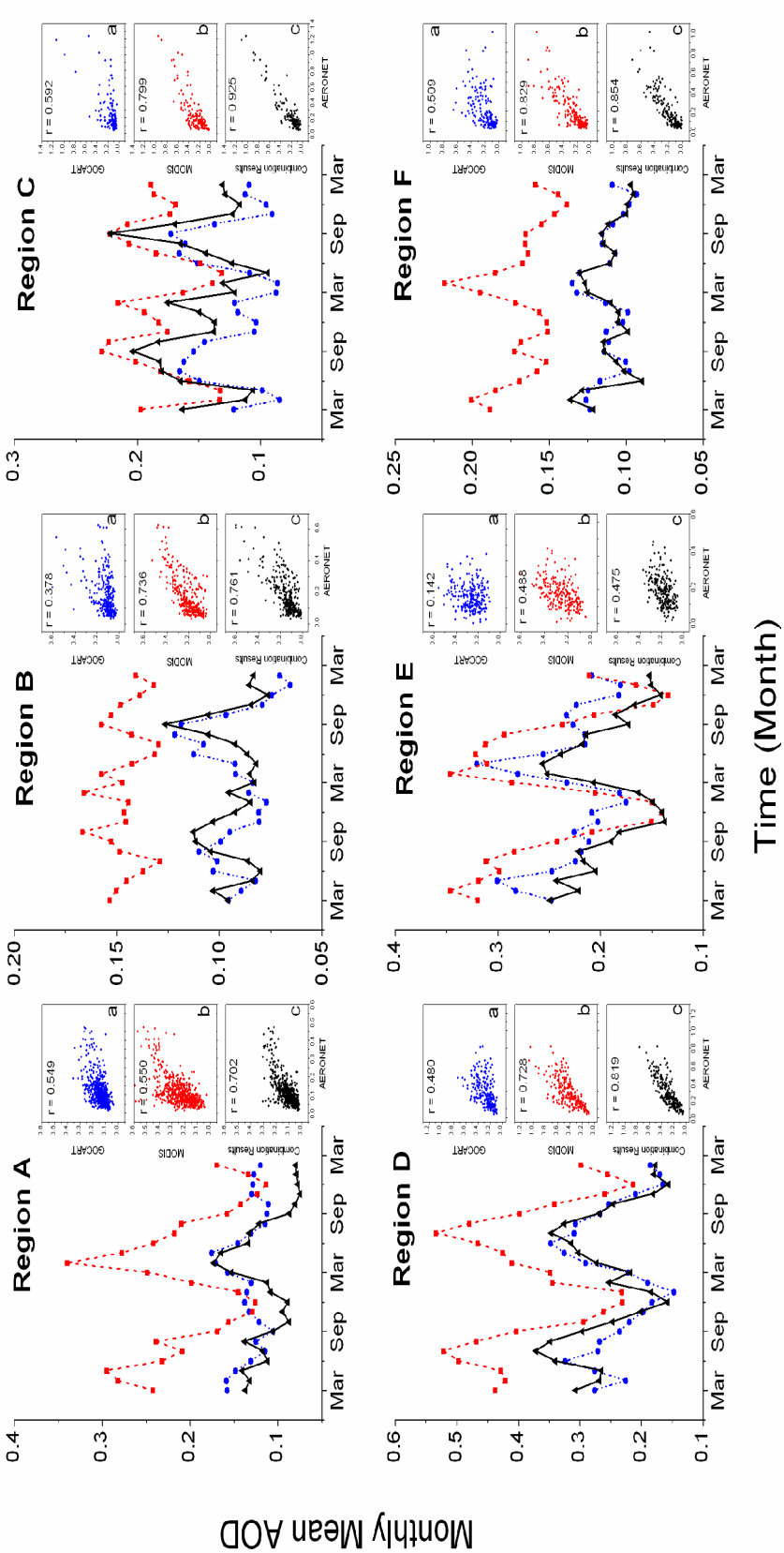

Figure 4.16 Regional comparison of the empirical combination results with GOCART and MODIS data. Also shown are the scatter plots of three datasets against AERONET measurements (a: GOCART; b: MODIS; c: Combination results). Domains are defined in Table 4.3 and shown in Figure 4.3. Grid points without MODIS retrievals are not included.

monthly AODs over large parts of the world are within the low and medium range, the combination results tend to be close to model simulations. However, variations of the merged results are more consistent with MODIS retrievals which would imply that the GOCART model provides better estimates of the magnitude, while MODIS results describe better the variations.

4.2 Aerosol single scattering albedo

The direct radiative effect of aerosols is sensitive to the single scattering albedo (ω_0) [*Hansen et al.*, 1997; *Satheesh and Ramanathan*, 2000]; however, observations of aerosol absorbing properties are limited and difficult to obtain [IPCC, 2001]. At present, no reliable global column aerosol SSA data sets from satellite retrievals are available. In this study, characterization of the single scattering albedo is based on GOCART model result and AERONET almucantar retrievals.

4.2.1 GOCART model simulated global SSA at 0.55μm

Column aerosol SSA can be calculated from the simulated concentration of each aerosol component, assumed complex refractive index and particle size and shape. GOCART model incorporates five key components (sulfate, dust, organic carbon, black carbon and sea salt). Particle density, size distribution and complex refractive index were taken from Global Aerosol Data Set (GADS) [*Köepke et al*. 1997]. Homogeneous spherical and external mixtures are assumed to calculate

aerosol column single scattering albedo (SSA). Derived monthly mean aerosol SSA at 0.55μm for the year of 2001[5] is displayed in Figure 4.17.

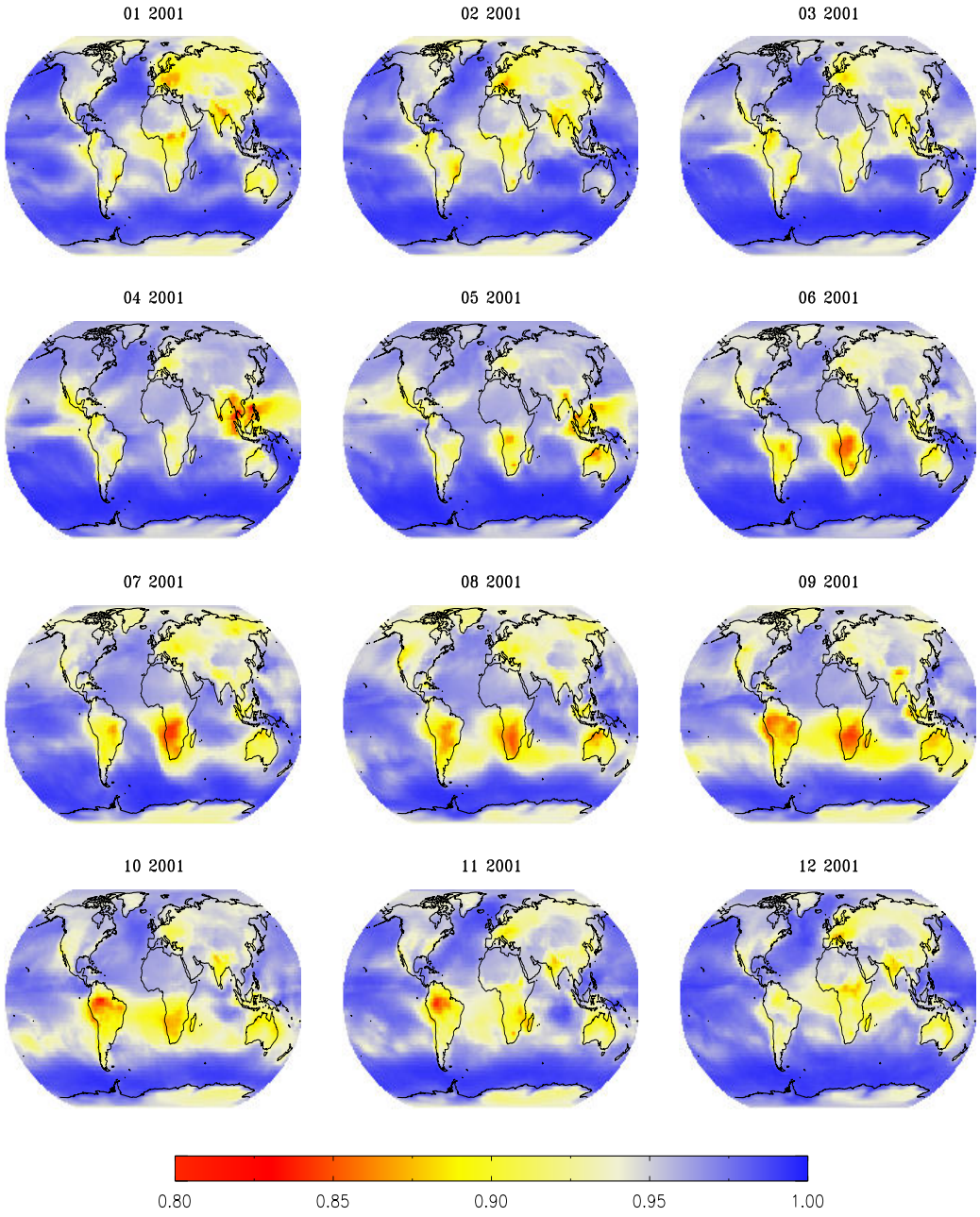

Figure 4.17 GOCART model simulated column aerosol single scattering albedo at 0.55 μm for the year 2001.

[5] Courtesy of Dr. Mian Chin.

A scatter plot of modeled ω_0 against available AERONET almucantar retrievals of ω_0 is presented in Figure 4.18. We have interpolated the AERONET values at 0.55 μm from 0.44 and 0.67 μm data if more than five retrievals are available within one month. Majority of GOCART simulated ω_0 (76%, 32 out of 42 pairs) fall within the uncertainty of AERONET retrievals (±0.03); however, outliers do exist with the most obvious ones coming from two stations (Yulin, China and Alta Floresta, Brazil) at boreal summer and autumn time. It is difficult to ascertain if such large discrepancies are due to model deficiencies or sampling issues. An effort has been made to examine the quality of GOCART aerosol intensive properties, yet it is still in a preliminary stage due to scarcity of high quality measurements [*Chin*, private communication]. Therefore, correction is not attempted here and aerosol ω_0 at 0.55 μm from GOCART model is accepted "as is".

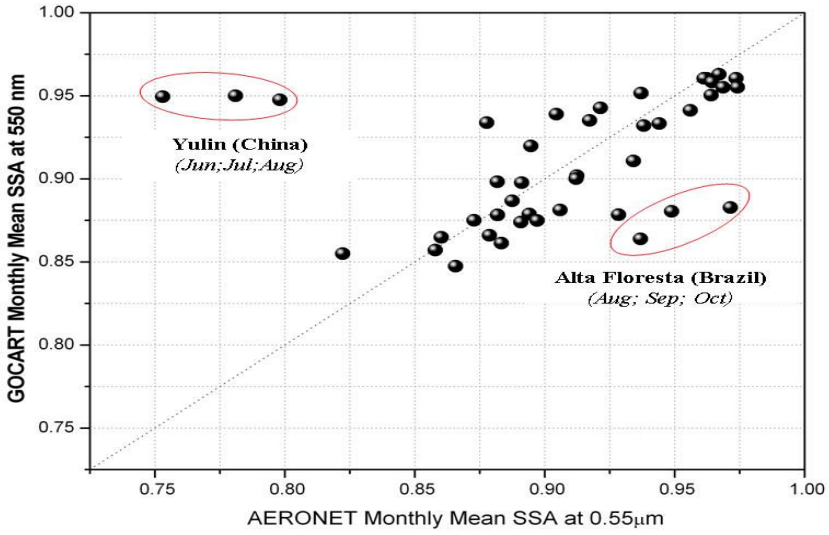

Figure 4.18 Scatter plot of GOCART monthly mean SSA at 550 μm against AERONET amucantar retrievals for the year 2001. Monthly mean AERONET SSA is calculated if more than five days data are available. Outliers are basically associated with two stations (Yulin and Alta Foresta) in the boreal summer and autumn time.

4.2.2 Spectral variation of aerosol SSA from AERONET retrievals

Chemical composition and microphysical properties determine the spectral variation of aerosol ω_0. Measurements reveal two types of wavelength dependencies for absorbing aerosols: decreasing ω_0 as a function of wavelength, associated with small-sized aerosols that contain black carbon [*Bergstrom et al.*, 2002, 2003; *Dubovik et al.*, 1998, 2002]; and increasing ω_0 as a function of wavelength, associated with dust dominated aerosols [*Sokolik and Toon*, 1999; *Dubovik et al.*, 2002; *Bergstrom et al.*, 2004; *Torres et al.*, 2005; *Eck et al.*, 2005]. In the first case the variation is largely due to the stronger decrease of the scattering coefficient with wavelength as compared to the absorption coefficient; in the second case, it is mainly attributed to the larger imaginary refractive index of mineral dust at the short end of the solar spectrum [*Patterson et al*., 1977; *Alfaro et al*, 2004]. Consequently, analysis of spectral variations of ω_0 should be executed separately for dust and other aerosols.

More than ten years (from 1993 to 2003) of instantaneous AERONET almucantar retrievals are used to demonstrate and analyze the spectral variations of ω_0. They are grouped by their value at 0.55 μm at 0.01 bin intervals. For dust dominated conditions, results based on spheroid assumption retrievals are used due to their superior quality compared to spherical assumption [*Dubovik et al*., 2002]. Figure 4.19 shows the spectral variation as a functions of aerosol type (dust vs. non-dust) and of ω_0 at 0.55 μm.

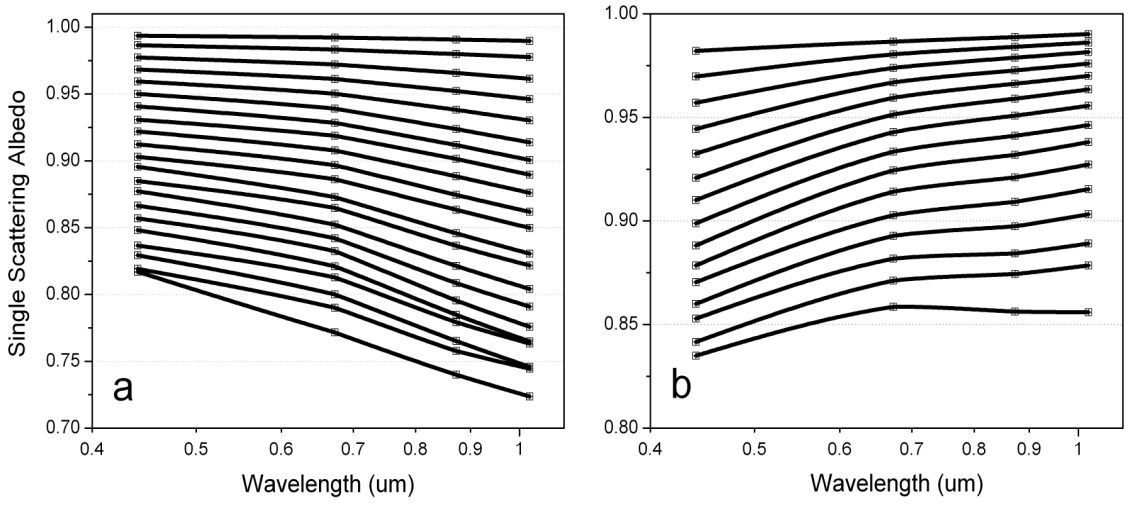

Figure 4.19 Spectral variation of aerosol single scattering albedo derived in this study from more than 6000 instantaneous AERONET almucantar retrievals from 1993 to 2003. Data are binned at 0.01 intervals of ω_0 at 0.55 μm (a) fine mode dominant; (b) coarse mode dominant (dust).

4.2.3 Global monthly mean aerosol SSA over the solar spectrum

Applying the spectral variations of Figure 4.19 to GOCART ω_0 at 0.55 μm requires the identification of aerosol type (dust or non-dust). To this end, we use MODIS derived monthly mean Ångström exponent (α) combined with merged $\tau_{0.55\mu m}$ to specify regions where dust aerosol dominates. Over bright surfaces no retrievals are made from MODIS observations; therefore, we perform data-filling as follows: 1) for high latitudes (>60º), we replace missing values with data from nearest available month; otherwise, latitudinal average is used; 2) linear interpolations in space are performed to fill in the remaining voids. Since MODIS provides $\alpha_{0.44-0.66\mu m}$ over land and $\alpha_{0.55-0.87\mu m}$ and $\alpha_{0.87-2.13\mu m}$ over ocean, a second order polynomial fit is used to estimate $\alpha_{0.44-0.66\mu m}$. Dust aerosols are determined by the criteria that over

land $\alpha_{0.44-0.66\mu m}$ is less than 0.75 (same threshold was used by *Eck et al.* [2005], but applied to $\alpha_{0.44-0.87\mu m}$); over ocean an additional requirement of $\tau_{0.55\mu m}$ larger than 0.2 is enforced to separate from large sea salt particles (relatively low optical depth of maritime aerosols). Figure 4.20 displays the successfully identified major dust source regions (Northern Africa, Middle East, Central Asia, Australia, part of America and South Africa) and transports areas (tropical Atlantic and Northern Pacific). Having such information on aerosol type and the GOCART model ω_0 at 0.55 μm, the appropriate wavelength dependent curve can be selected from Figure 4.19. Expansion of ω_0 to the whole solar spectrum is performed based on linear interpolation/extrapolation with respect to the logarithm of wavelength.

Due to built-in assumptions, uncertainties are expected in the derived global aerosol ω_0 over the solar spectrum. Simulations are performed to evaluate the sensitivity of aerosol surface effects on the aerosol single scattering albedo. Similar to the tests in section 3.1, two-stream two-layer approximation (Eq. (3.4)) is used to assess the influence of ±0.05 uncertainty in ω_0 for various types of aerosols on global annual surface irradiance. Figure 4.21 shows the changes of global annually averaged aerosol direct effect. Increasing aerosol absorption ($\Delta\omega_0 = -0.05$) leads to a further depletion of surface SW radiation; the most significant effect is associated with the least absorbing aerosols (sea salt). Sensitivity is also dependent on the aerosol asymmetry parameter (g) with stronger effects related to the more powerful forward scattering particles(larger g), as seen for dust and for GSFC aerosols that have

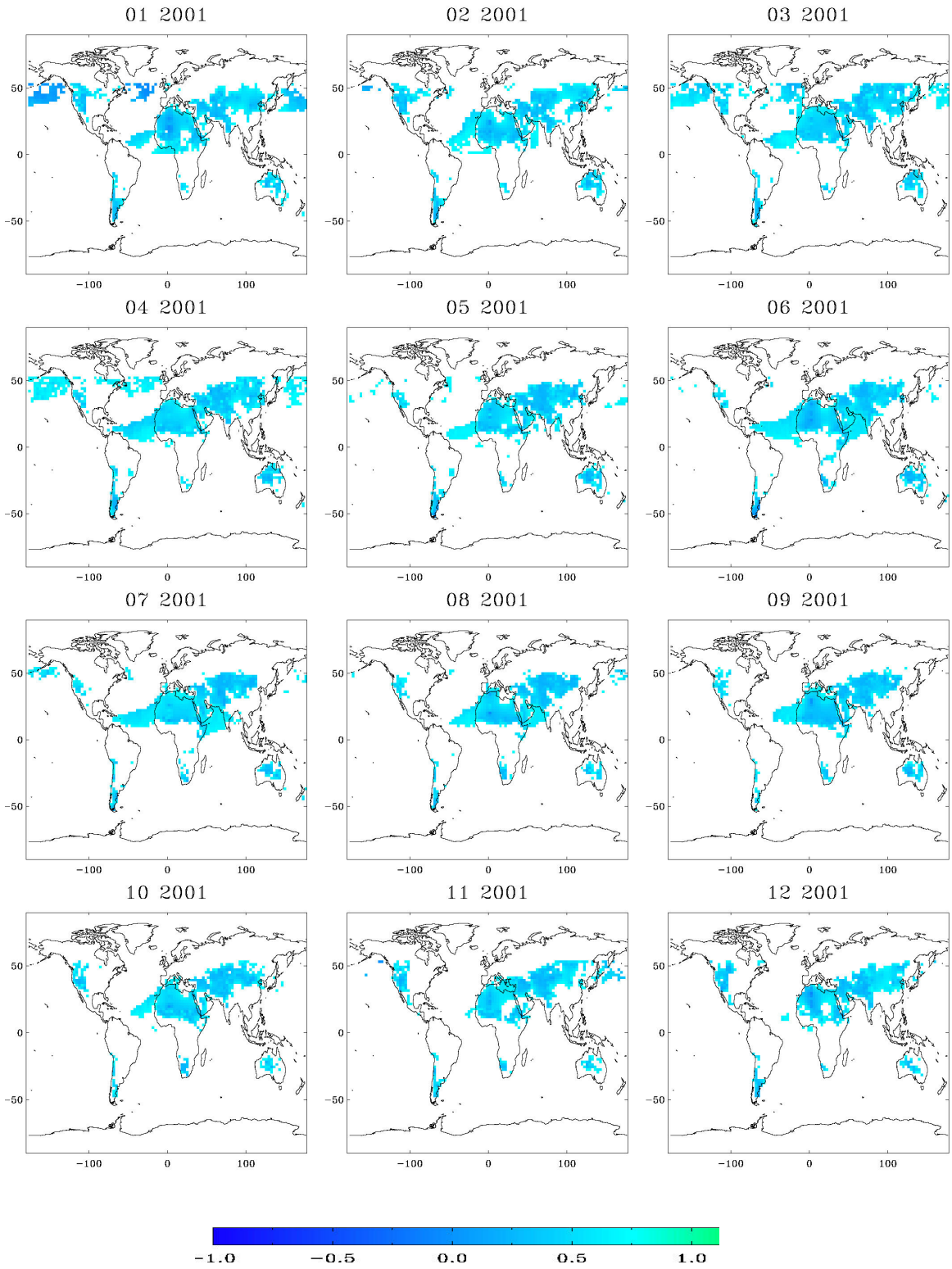

Figure 4.20 Dust dominated areas identified on the basis of MODIS $\alpha_{0.44-0.87\,\mu m}$ and merged $\tau_{0.55\,\mu m}$. The color bar represents values of $\alpha_{0.44-0.87\,\mu m}$.

similar ω_0. Assuming that the global average $\tau_{0.55\mu m}$ is 0.15, a 0.05 uncertainty in ω_0 would translate to an error of about 2 Wm^{-2} (20%) on the global annual averaged aerosol direct surface effect.

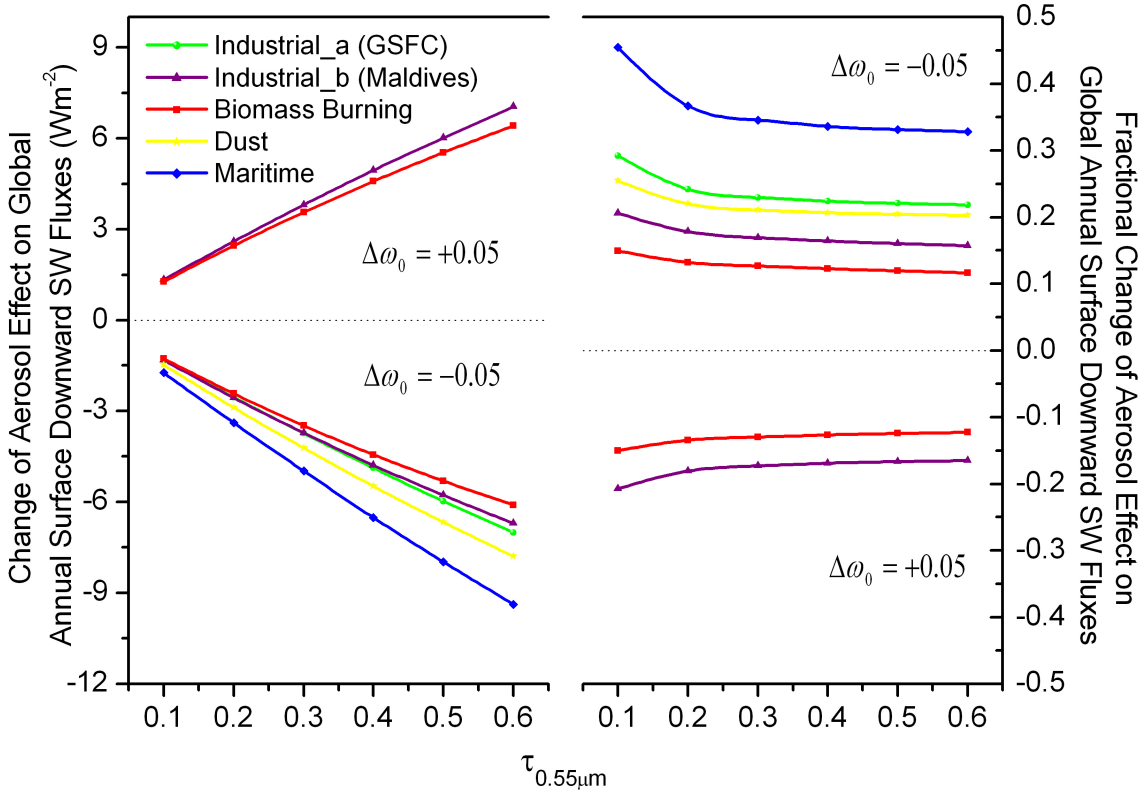

Figure 4.21 Changes of global annually averaged aerosol direct effects on the surface downward SW fluxes for various types of aerosols due to ±0.05 uncertainty of ω_0. Cases where increase of 0.05 results in ω_0 being beyond 1.0 are not simulated (GSFC, Dust and Maritime aerosols). Left Panel: change of flux values (Wm^{-2}); Right panel: fractional changes (the ratio of the change and original surface effect).

4.3 Aerosol asymmetry parameter

Aerosol asymmetry parameter (g) is determined predominantly by particle shape, size distribution and real part of the refractive index. Figure 4.22 shows the variation of g as functions of particle size and real refractive index based on theoretical analysis [*Hansen and Travis,* 1974]. In terms of geometric optics, local maxima and minima can be interpreted as the result of interference of light diffracted and transmitted by the particle. For the majority of ambient aerosols, real part of refractive index varies around the value of 1.5 within a limited range (±0.15) [*Köpke et al*. 1997]; therefore, given the widely adopted spherical shape assumption, size distribution might be the governing factor affecting the spectral variation of g. In this thesis, we obtain a global description of g from the size information inferred from MODIS remote sensing product.

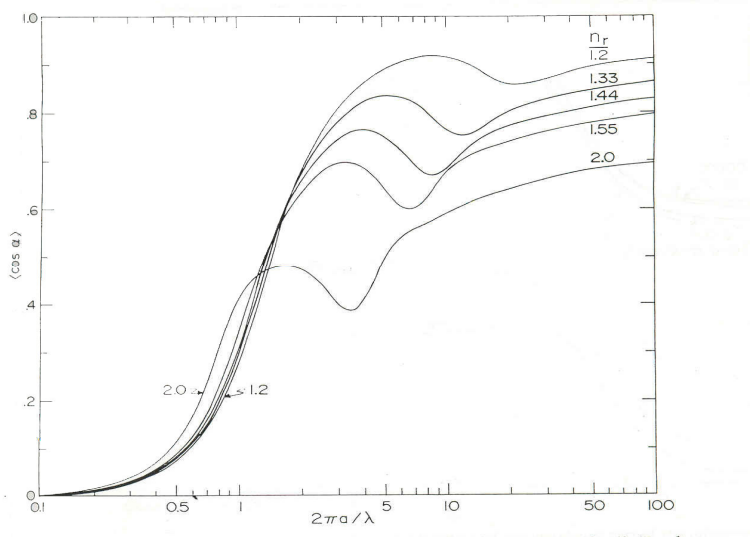

Figure 4.22 Asymmetry parameter $<\cos\alpha>$ (g), as a function of effective size parameter ($2\pi a/\lambda$). Results are shown for five values of the real refractive index, n_r, all with n_i=0. A variation of gamma size distribution was used with effective variance b=0.07 (Figure12 from *Hansen and Travis* [1974]).

4.3.1 Relationship between asymmetry parameter and Ångström exponent

Ångström exponent (α), a fundamental product from multi-spectral satellite retrievals (e.g., from MODIS, MISR, two-channel AVHRR), provides information about aerosol size. Theoretical studies revealed that α can be related to the Junge (power law) number size distribution [*Junge*, 1955]:

$$\frac{dN}{d\ln r} = cr^{-\nu} \tag{4.8}$$

by $\alpha = \nu - 2$ [*Van de Hulst*, 1957; *Bullrich*, 1964]. A more well-accepted understanding is an inverse relationship between α and particle size, namely, the larger the exponent, the smaller the particles. Due to theoretical difficulties and large variations associated with aerosol size distribution, this relationship has not been explored beyond being used as a qualitative indicator.

To develop a relationship between α and g, we produce a scatter plot of asymmetry parameters versus effective size parameters estimated from $\alpha_{0.44-0.67\mu m}$ (Figure 4.23). Data used are the instantaneous AERONET almucantar retrievals at 4 wavelengths (0.44, 0.67, 0.87 and 1.02 μm) from 1993 to 2003. We require $\tau_{0.44\mu m}$ >0.3 due to the higher retrieval quality for the higher loading cases [*Dubovik et al*, 2002]. There is a similarity in magnitude and variability when compared with theoretical studies. We fit the scatter points by a regression analysis of a two-step Gaussian curve:

$$g_\lambda = \begin{cases} a_2 \exp\left(-\dfrac{(x-a_0)^2}{2a_1^2}\right) & when \quad \ln x < 1.9 \\ b_3 - b_2 \exp\left(-\dfrac{(x-b_0)^2}{2b_1^2}\right) & when \quad \ln x \geq 1.9 \end{cases} \tag{4.9}$$

Values of corresponding coefficients are presented in Table 4.5. The independent variable is the approximated effective size parameter x derived from $\alpha_{0.44-0.67\,\mu m}$ by:

$$x = {0.8\pi}/{\lambda\alpha_{0.44-0.67\,\mu m}} \tag{4.10}$$

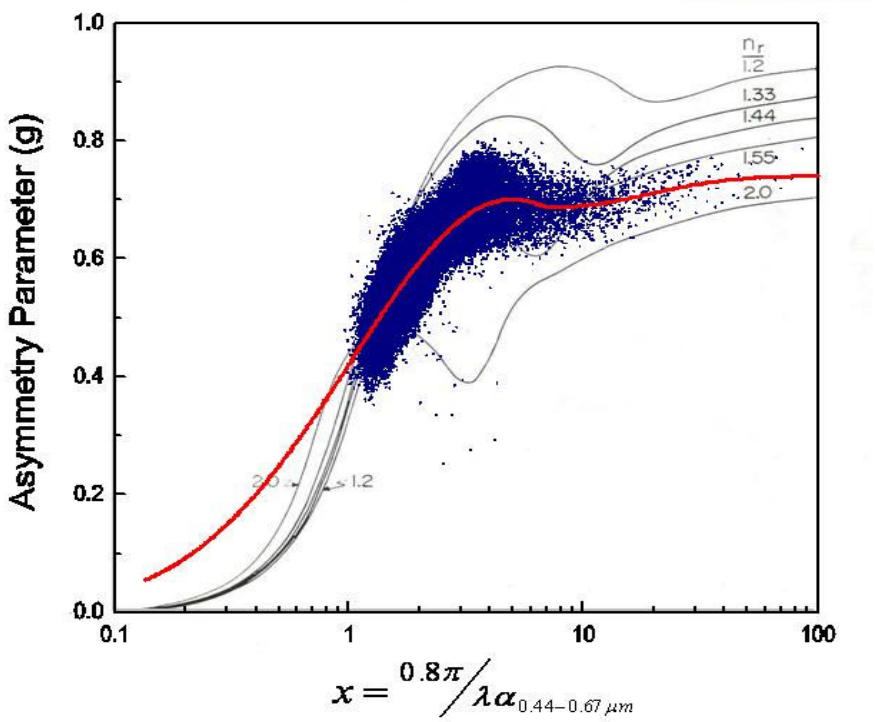

Figure 4.23 Scatter plot of asymmetry parameter against approximate effective size parameter ($x = {0.8\pi}/{\lambda\alpha_{0.44-0.67\,\mu m}}$) from instantaneous AERONET almucantar retrievals ($\tau_{0.44\,\mu m} > 0.3$) at 4 wavelengths (0.44, 0.67, 0.87 and 1.02 μm). Red curve is the regressed empirical relationship. Figure 4.22 is also shown as background for comparison.

Table 4.5 Coefficients of the empirical relationship (Eq. (4.9)) used to derive Asymmetry parameter from Ångström exponent.

	a_0	a_1	a_2
	1.61379	1.59757	0.69420
b_0	b_1	b_2	b_3
2.08552	0.84890	0.05382	0.742232

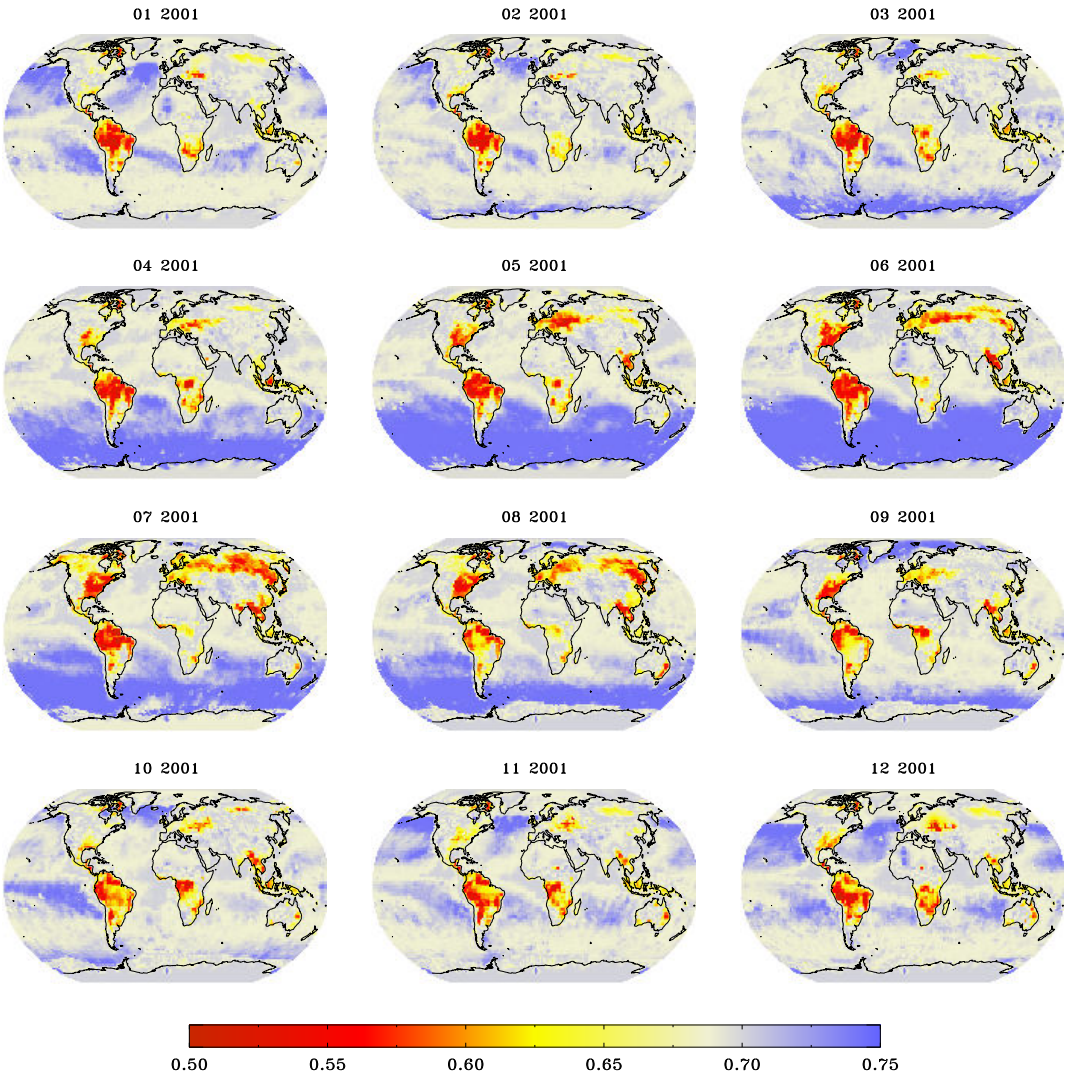

Figure 4.24 Calculated asymmetry parameter at 0.55 μm based on the empirical relationship (Eq. (4.9)) and MODIS derived $\alpha_{0.44-0.66\mu m}$ (data void areas were filled).

4.3.2 Global monthly mean asymmetry parameter over solar spectrum

Using the empirical relationship of Eq. (4.9), we estimate the global monthly averaged aerosol asymmetry parameter as a function of wavelength using MODIS $\alpha_{0.44-0.66\mu m}$ (derived from $\alpha_{0.55-0.87\mu m}$ and $\alpha_{0.87-2.13\mu m}$ over ocean based on a second order polynomial fit). Figure 4.24 illustrates the derived $g_{0.55\mu m}$ for year 2001.

The following limitations are associated with this parameterization scheme:

1). Qualitative understanding of the inverse relationship between particle size and Ångström exponent is based on the assumption that:

$$r_{eff} = 0.4 \Big/ \alpha_{0.44-0.67\,\mu m} \tag{4.11}$$

Support for this assumption is provided by Figure 4.25 in which we show the histogram of $r_{eff} * \alpha_{0.44-0.67\,\mu m}$ for more than 58,200 AERONET instantaneous retrievals from 1993 to 2003. A single peak exists around the value 0.4. However, problems arise from cases included in the extended tails. Furthermore, presence of negative α invalidates assumption of Eq. (4.11) and requires special attention (in applications a negative $\alpha_{0.44-0.67\,\mu m}$ is changed to 0.01).

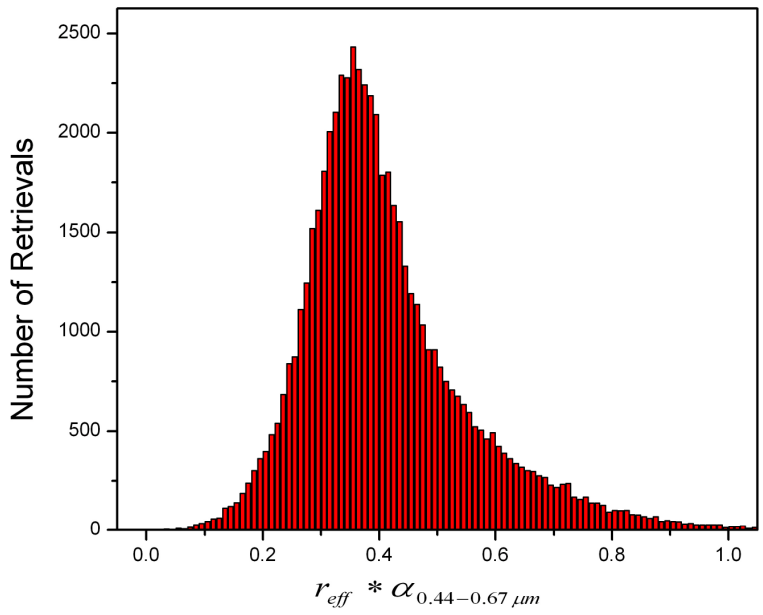

Figure 4.25 Histogram of $r_{eff} * \alpha_{0.44-0.67\,\mu m}$, derived from more than 58,200 available AERONET instantaneous almucantar retrievals from 1993 to 2003.

2). This empirical relationship is derived to represent average conditions, and therefore, it can not capture the detailed variations displayed in Figure 4.23.

3). Concern about the applicability of the empirical relationship for the fine mode dominated aerosols at longer wavelengths (>1.02 μm). As seen in Figure 4.23, this is the domain where data from AERONET retrievals are not available ($x < 1$). We base the projected monotonous decrease of g with the decrease of x on the theoretical relationship presented in Figure 4.22. Such variation is based on simulations with a variation of gamma size distribution (characterized by a single mode as used by *Hansen and Travis* [1974]), which might miss the influence of coarse mode particles. Figure 4.26 illustrates the effect of the coarse mode particles on g as a function of wavelength and effective size parameter for the GSFC aerosol model [*Dubovik et al*., 2002]. Incorporation of coarse mode greatly changes the variation trend of g in the region where $x < 1.5$ (or $\lambda > 1 \mu m$). This can be explained by the increased influence of large particles and reduced scattering contribution from the fine mode when the "small particle regime" is approached. Therefore, even an insignificant amount of coarse mode particles could dominate the behavior of g in this region. Coexistence of fine and coarse mode particles in ambient aerosols is quite common as discussed in several studies [*Whitby*, 1978; *Shettle and Fenn,* 1979; *Remer and Kaufman*, 1998, *Dubovik et al*., 2002]. Accuracy of the MODIS derived α will also affect the quality of the derived g. Evaluation of instantaneous MODIS retrieved $\alpha_{0.44-0.67 \mu m}$ over land revealed differences when compared with AERONET measurements [*Chu et al*., 2002].

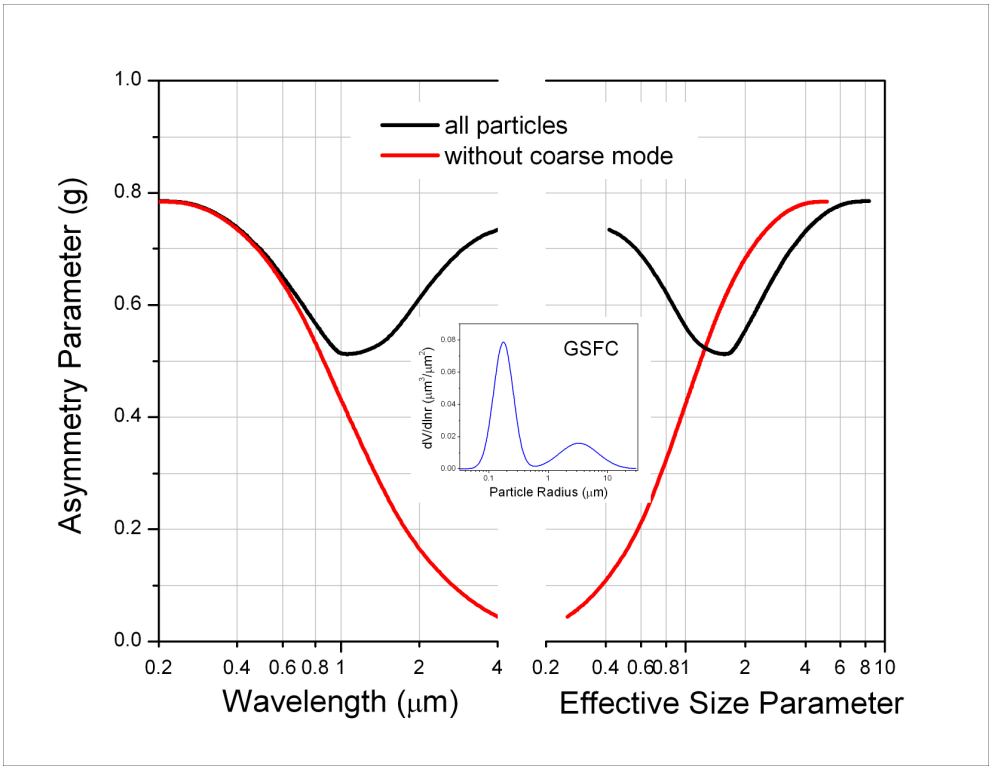

Figure 4.26 Effect of coarse mode particles on asymmetry parameter as functions of wavelength and effective size parameter. Inner panel is the volume size distribution of aerosols at GSFC [*Dubovik et al.*, 2002] where a bimodal lognormal function is used:

$$\frac{dV}{d\ln r} = \sum_{i=1}^{2} \frac{C_{v,i}}{\sqrt{2\pi}\sigma_i} \exp\left(-\frac{\left(\ln r - \ln r_{v,i}\right)^2}{2\sigma_i^2} \right)$$

Parameters were calculated for the case where $\tau_{0.44\mu m} = 0.5$, which leads to:

1) fine mode: $r_{v,1} = 0.175\mu m$, $\sigma_1^2 = 0.144$, $C_{v,1} = 0.075$;
2) coarse mode: $r_{v,2} = 3.275\mu m$, $\sigma_2^2 = 0.563$, $C_{v,2} = 0.030$.

Sensitivity tests similar to those of section 4.2.3 are carried out to assess the influence of ±0.1 variations of g for various types of aerosols on the global annual surface irradiance. Table 4.6 shows that influence on the backscattered fraction $\overline{\beta}$ is dependent on the actual value of g: the higher the asymmetry parameter the larger is the effect. In terms of impact on the surface downward SW fluxes, such dependence

is further strengthened by the positive correlation between g and ω_0 (Figure 2.1) (higher ω_0 indicates a larger part of extinction is affected by the uncertainty of g). Figure 4.27 illustrates that variations of effects are associated with different types of aerosols. Assuming a globally averaged $\tau_{0.55\mu m}$ of 0.15, a 0.1 uncertainty in g would result in an influence from 1 to 2 Wm^{-2} on the aerosol direct effects on surface irradiance.

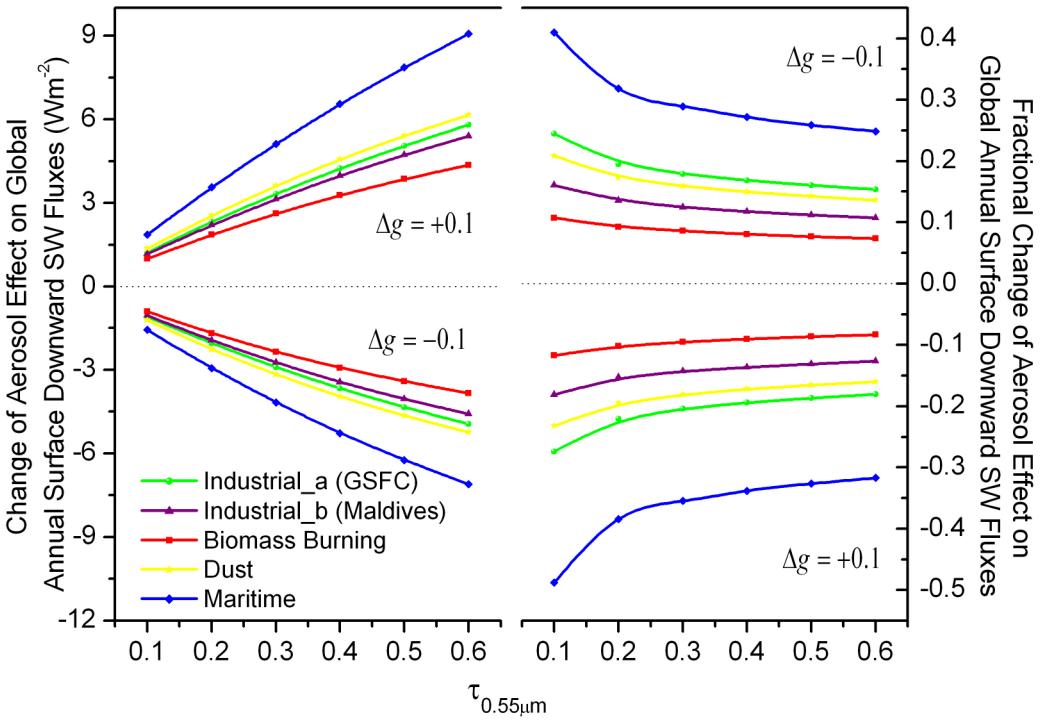

Figure 4.27 Changes of the global annually averaged aerosol direct effects on the surface downward SW fluxes for various types of aerosols due to ±0.1 uncertaintiy of g. Left Panel: change of flux values (Wm^{-2}); Right panel: fractional changes.

Table 4.6 Changes of backscattered fraction for isotropically incident radiation ($\overline{\beta}$) due to ±0.1 variations of g for various types of aerosols.

Aerosol Type	g (*SW broadband Average*)	$\Delta g = +0.1$		$\Delta g = -0.1$	
		$\Delta\overline{\beta}$	$\Delta\overline{\beta}/\overline{\beta}$	$\Delta\overline{\beta}$	$\Delta\overline{\beta}/\overline{\beta}$
Industrial (a)	0.677821	-0.051448	-0.22902	0.046427	0.20667
Industrial (b)	0.688620	-0.052154	-0.23774	0.046865	0.21363
Biomass Burning	0.607242	-0.047670	-0.18490	0.043998	0.17066
Dust	0.661138	-0.050433	-0.21675	0.045788	0.19679
Maritime	0.778430	-0.060243	-0.34850	0.051486	0.29785

4.4 Aerosol normalized extinction coefficient

Spectral variation of α has been reported previously [*Eck et al.*, 1999, *O'Neill et al.*, 2001]. Since over land, MODIS retrievals are made only in two channels, we assume a wavelength independent α ($=\alpha_{0.44-0.66\,\mu m}$) in our calculation of the normalized extinction coefficients between 0.2 to 4.0 μm. Over oceans, we use a second order polynomial fit to $\ln\tau$ versus $\ln\lambda$ (based on $\alpha_{0.55-0.87\,\mu m}$ and $\alpha_{0.87-2.13\,\mu m}$) to estimate the spectral variation of aerosol extinction.

4.5 Comparison with GOCART model results

We carry out calculations of aerosol intensive radiative properties over the solar spectrum for September 2001, using GOCART model simulated aerosol concentrations, ambient humidity, assumed aerosol optical constants and size distribution. We integrate simulated monthly and column averaged ω_0, g and the normalized extinction coefficients, as well as our derived values into five SW sub-bands (0.2-0.4, 0.4-0.5, 0.5-0.6, 0.6-0.7 and 0.7-4.0 μm) based on Eqs. (3.11-3.13). Due to uncertainties at the short end of the effective size parameter, empirically

derived g in the 0.7-4.0 μm interval is set to be no less than 0.639 (the value used for the CONT-I aerosol model [WCP-55, 1983]). In Table 4.7 we compare GOCART model results with the estimates of this work in terms of mean difference, standard deviation and correlation coefficient. Good agreement in ω_0 is due to the fact that GOCART values of ω_0 at 0.55μm are used in our estimation scheme, yet differences in spectral variation can be seen. Average difference in g is about 0.06 with GOCART data being systematically larger than the empirical estimation. Global averaged normalized extinction coefficients differ by less than 0.08. The low correlations (about 0.4) and the relatively large standard deviations in g and the normalized extinction coefficients indicate the need for additional work on the characterization of aerosol intensive properties.

Table 4.7 Comparison of monthly mean aerosol single scattering albedo, asymmetry parameter and normalized extinction coefficient at 5 SW sub-bands between GOCART model results and estimations in this work for September, 2001. Calculated are mean difference (GOCART-estimation); standard deviation of the difference and correlation coefficient.

	0.2-0.4μm	**0.4-0.5μm**	**0.5-0.6μm**	**0.6-0.7μm**	**0.7-4.0μm**
			Single Scattering Albedo (ω_0)		
Mean Diff	-0.0257	-0.0117	-0.0030	0.0024	0.0135
Std Dev	0.0111	0.0053	0.0049	0.0083	0.0241
Corr Coef	0.9245	0.9873	0.9954	0.9777	0.8209
			Asymmetry Parameter (g)		
Mean Diff	0.0628	0.0665	0.0607	0.0549	0.0605
Std Dev	0.0259	0.0306	0.0377	0.0454	0.0594
Corr Coef	0.4794	0.4415	0.3959	0.3846	0.3925
			Normalized Extinction Coefficients		
Mean Diff	-0.0778	0.0181	-0.0023	-0.0264	-0.0463
Std Dev	0.4227	0.1131	0.0023	0.0672	0.1905
Corr Coef	0.4005	0.4312	0.9921	0.4382	0.4205

4.6 Summary

In this chapter, we estimate global monthly mean aerosol properties in the SW spectrum based on data from GOCART model simulations, MODIS retrievals and AERONET measurements/retrievals.

1) Our estimates of aerosol optical depth at 0.55 μm are based on the large-scale spatial and temporal variation patterns of model and satellite data while the magnitude is regulated by the AERONET measurements.
2) We generate the single scattering albedo by extending GOCART ω_0 at 0.55 μm to the entire SW spectrum using spectral dependences derived from available AERONET retrievals.
3) We determine the asymmetry parameters over the solar spectrum from MODIS Ångström wavelength exponent, utilizing an empirical relationship derived from AERONET almucantar retrievals.
4) We estimate the normalized extinction coefficient from the MODIS Ångström wavelength exponents.
5) We perform sensitivity tests for ω_0 and g to assess effects on surface downward SW fluxes. For an assumed global average $\tau_{0.55\mu m}$ of 0.15, a perturbation of 0.05 and 0.1 in ω_0 and g will result in about 2.0 and 1.5 Wm^{-2} flux change, respectively.
6) We perform a comparison of empirically derived aerosol intensive optical properties with estimates based on GOCART modeled results for one month (September, 2001). Differences between the two data sets call for the need in additional work on this aspect.

Chapter 5: Newly derived aerosol information: Implications for surface SW radiation budget

5.1 Introduction

Information on aerosol properties at global scale is needed for many climate research applications. One such need arises in inference schemes that derive surface radiative fluxes from satellite observations. We will use the newly derived aerosol information in such a context. At the same time, assessment of the surface fluxes from the inference scheme against ground observations can serve as an independent evaluation of the improved aerosol information. Most existing models for deriving surface radiative fluxes from satellites have only a very rudimentary capability to treat aerosols. Before one can use the new aerosol information, there is a need to modify the inference schemes so that they can incorporate such information. The added value of the modified models is that they will be ready to ingest improved information from future satellite missions and advances in chemical transport models. Moreover, the chemical transport models can benefit from the satellite based inference schemes since they provide internal consistency checks by being constrained at both boundaries of the atmosphere by radiation observations. The existing status of the model will be described first to be followed by the description of the modification and implementation of the new aerosol information in the inference scheme.

5.2 The clear-sky scheme of UMD SRB model

The following steps are taken in the UMD SRB model to estimate clear-sky surface SW fluxes [*Pinker and Laszlo*; 1992]:

1) *Derive planetary albedo from satellite radiances*

Anisotropic correction and spectral transformation of narrowband measurements to convert the directional reflectance to TOA albedo are based on results from the Earth Radiation Budget Experiment (ERBE) [*Shuttle et al.*, 1988] and radiative transfer simulations [*Laszlo et al.*, 1988].

2) *Estimate atmospheric optical functions and surface albedo*.

For clear-sky cases, the satellite signal in the SW part of the spectrum contains information on both the atmosphere and the surface. Since we assume that atmospheric water vapor and ozone amounts are known, the unknowns in this signal are associated with aerosols and surface conditions. The simultaneous estimation of aerosol optical depth and surface albedo from one measurement makes this an ill-posed inverse problem. In the present version of the model, the approach taken is as follows: aerosol radiative properties are prescribed over oceans and continents (MAR-I and CONT-I from WCP-55 [1983]) with aerosol optical depths assumed as 0.23 over land; 0.5 over desert; 0.128 over ocean and 0.05 over snow/ice; clear-sky composite radiance (an average value for about a month) is used with such aerosol information to estimate the surface albedo. Once the albedo is known the instantaneous aerosol optical depth is derived for each instantaneous observation for the clear sky cases. Pre-calculated lookup tables prepared with the adding-doubling

scheme of radiative transfer are utilized in the AOD retrievals and interpolated to estimate the atmospheric optical functions ($R_a(\mu_0)$; $T_a^{dir}(\mu_0)$; $T_a^{dif}(\mu_0)$; $\tilde{R}_a$ and $\tilde{T}_a$).

3) *Calculate surface SW fluxes*.

Once the atmospheric optical functions and the surface albedo are specified, a complete description of shortwave SRB (narrow/broadband values of global/direct/diffuse downward/upward/absorbed fluxes) can be obtained using Eqs. (2.5) and (2.6). Five spectral intervals (0.2-0.4, 0.4-0.5, 0.5-0.6, 0.6-0.7 and 0.7-4.0 μm) are used in the model to cover the entire solar spectrum.

Alternative approaches can be applied to address the ill-posed problem. For example, it can be assumed that surface albedo over a time period can be determined from the minimum TOA reflectance where aerosol loading is assumed to be at a background level. The caveat associated with such scheme is that sensitivity to "rare" events (e.g., cloud shadows; wetness of surface) might lead to a negative bias in surface albedo [*Matthews and Rossow*, 1987]; hence, subjective elimination or thresholds must be applied to avoid such situations. UMD SRB model tackles this issue in a statistical manner: averaged clear-sky reflectance combined with monthly mean aerosol properties are used to estimate the surface reflectivity. In addition to the robustness of this method [*Matthews and Rossow*, 1987; *Rossow and Garder*, 1993], benefit comes from the fact that derived instantaneous AODs are fluctuating around the provided monthly mean values. As discussed in section 3.2, such AOD constraint is considered to be important.

5.3 Update of clear-sky scheme of UMD SRB model

To expand the capabilities of the model to accommodate progresses in aerosol research, the following updates were introduced:

1) Replacement of original monthly mean aerosol properties with the newly derived information (aerosol optical depth at 0.55 μm; normalized extinction coefficients, single scattering albedos and asymmetry parameters in five spectral intervals).

2) Current clear-sky look-up tables of atmospheric optical functions (five-dimension array $f\left(\lambda^i, {\mu_0}^j, \tau^k, H_2O^l, {O_3}^m\right)$ with spectral interval, cosine of solar zenith angle, aerosol optical depth at 0.55 μm, amount of water vapor and ozone in each dimension respectively; i, j, k, l, m represent the indices of discrete tabulated values associated with each variable) have been expanded to include the variation of aerosol single scattering albedo and asymmetry parameter ($f\left(\lambda^i, {\mu_0}^j, \tau^k, H_2O^l, {O_3}^m, {\omega_0}^n, g^o\right)$) [*Laszlo*, private communication].

3) In response to the complex aerosol characteristics, specific lookup tables pertaining to the specific aerosol intensive properties should be generated for AOD retrievals. To meet this challenge, modifications of model algorithm are performed as follows: the basic atmospheric optical function library $f\left(\lambda^i, {\mu_0}^j, \tau^k, H_2O^l, {O_3}^m, {\omega_0}^n, g^o\right)$ is generated as five independent sub-tables ($f_{i=1\ldots5}\left({\mu_0}^j, \tau^k, H_2O^l, {O_3}^m, {\omega_0}^n, g^o\right)$) relative to each individual spectral interval. As illustrated in Figure 5.1, at the beginning of each month, for each location, corresponding monthly mean values of single scattering albedo and asymmetry

parameter at five intervals are used to interpolate the sub-tables $f_{i=1...5}\left(\mu_0{}^j, \tau^k, H_2O^l, O_3{}^m, \omega_0{}^n, g^o\right)$ to $f'_{i=1...5}\left(\mu_0{}^j, \tau^k, H_2O^l, O_3{}^m\right)$ individually. Subsequently, normalized aerosol extinction coefficients multiplied by the tabulated discrete values of AOD are used to interpolate the sub-table $f_i'\left(\mu_0{}^j, \tau^k, H_2O^l, O_3{}^m\right)$ to $f''_i\left(\mu_0{}^j, \tau_i^k, H_2O^l, O_3{}^m\right)$ for $i = 1,\ 2,\ 4,\ 5$; therefore, for any specific index k, $\tau^k_{i=1...5}$ will keep the same ratios as the extinction coefficients. At last, five sub-tables are combined into a single one $f'''\left(\lambda^i, \mu_0{}^j, \tau^k_{0.55\mu m}, H_2O^l, O_3{}^m\right)$ with the only aerosol variable allowed to change is the extensive parameter $\tau_{0.55\mu m}$ (assume AOD averaged over 0.5-0.6 μm is equivalent to $\tau_{0.55\mu m}$). This way, spectral variations of aerosol intensive properties are included in an efficient manner.

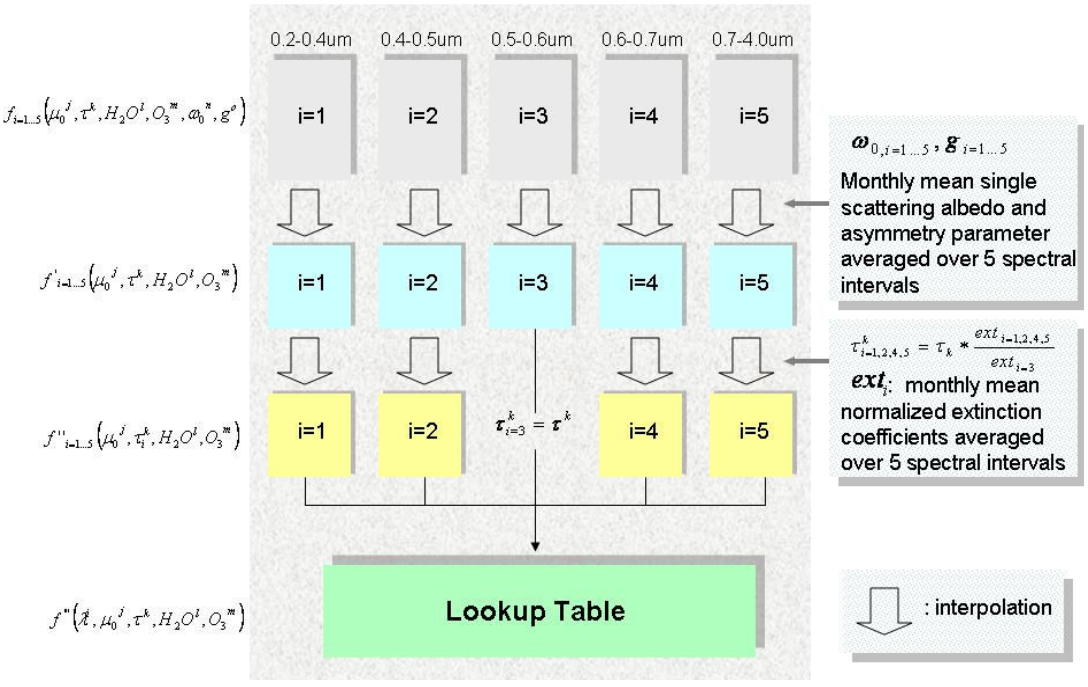

Figure 5.1 The updated look-up table scheme that allows to incorporate variation of aerosol intensive parameters: a specific look-up table is generated for specific aerosol intensive properties.

5.4 Implementation with ISCCP D1 data

In this section, the updated SRB model is implemented with satellite inputs from the ISCCP D1 product for one-year period (2001). This product is based on observations from five geostationary and two polar orbiting satellites at 3-hourly temporal resolution and 280km grids[6] [*Rossow et al.*, 1996]. The newly derived estimates of aerosol optical depths and surface SW downward fluxes will be compared with AERONET and BSRN measurements; aerosol direct radiative effects will also be calculated. The low spatial resolution of the ISCCP D1 set is not ideal for testing aerosol improvements in the scheme. However, the aim was to implement the new aerosol information at global scale; the ISCCP D1 data are the sole source of information with global coverage representing the diurnal cycle.

5.4.1 Evaluation schemes

We have developed four evaluation schemes to assess the performance of the updated version of the UMD SRB model:

Scheme A: updated model (introduced in section 5.1) is driven by the ISCCP D1 data with no changes to satellite inputs.

Scheme B: similar to scheme A, but ISCCP clear-sky composite radiance for each grid is replaced with a 31-day moving medians of clear radiances at same diurnal phase (3-hour interval). Motivation for this modification is the concern that the ISCCP clear-sky composite is not representative of the average clear-sky radiance (derived by increasing the minimum clear sky radiance by a predetermined amount that represents the typical separation of the minimum and mean value [*Rossow et al.*,

[6] More detailed introduction of ISCCP D1 data can be found in Appendix B.4.

1996]). Figure 5.2 illustrates for one grid box over the western United States that ISCCP clear-sky composite values could be systematically lower than the clear radiance. Preliminary modification is proposed by using 31-day moving median of clear radiance to characterize the averaged clear-sky reflectance. Median value is preferred to the arithmetic average due to the consideration that TOA reflection might not be a linear function of the amount of atmospheric components and insensitive to extreme situations. To derive the updated clear sky composite, the scaled radiance is first normalized to the nadir sun condition. Next, the median value of the angularly corrected scaled radiance is determined from adjacent 31 days at the same daytime. Finally, reverse angular correction is performed to derive the median scaled radiance. Moving medians resulting from this process are also displayed in Figure 5.2.

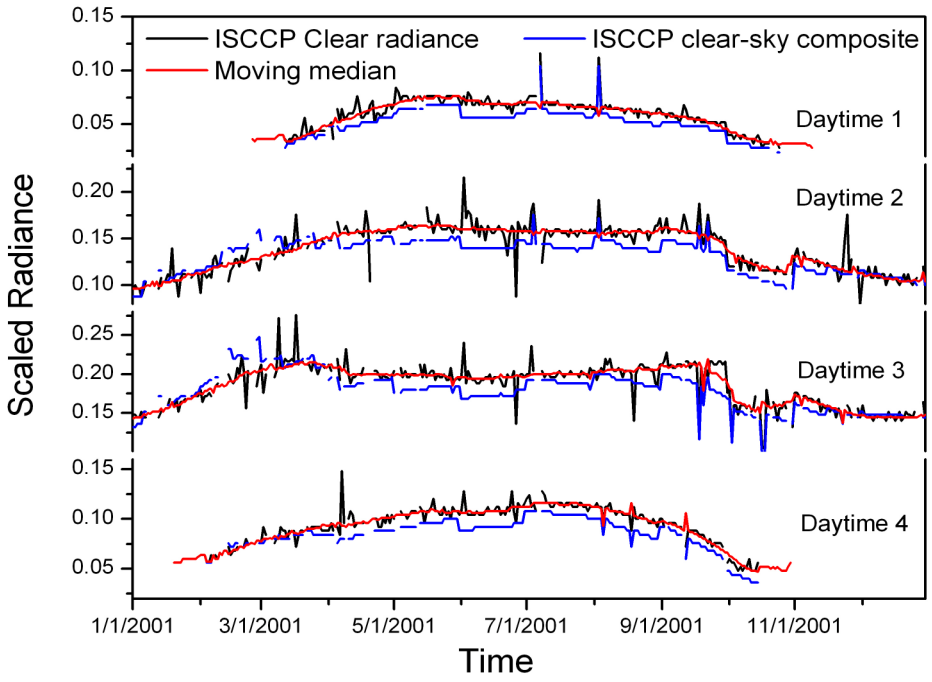

Figure 5.2 Time series of ISCCP D1 clear-sky scaled radiance, clear-sky composite and derived 31-day moving medians of scaled radiance for one grid box covering the location of Desert Rock, NV, USA. Daytime data are reported for four3-hr intervals.

Scheme C: within each month, AOD is assumed to be constant and equal to the monthly mean value. Therefore, the only unknown is now the surface albedo. In this scheme it would not be possible to capture detailed AOD variations within a month.

Scheme D: we calculate surface albedo from MOD43B1 BRDF/Albedo model parameters products[7] [*Schaaf et al*., 2002], and we retrieve the instantaneous AOD. We use a linear interpolation to describe a smooth transition from reported MODIS albedo (available every 16 days). Data void areas (over oceans and high latitudes) are not filled; hence, results from this scheme do not have a global coverage.

The original version of the UMD SRB model ("original") will be also implemented for comparison.

Conservation of energy principle will be satisfied in all schemes by producing the same amount of reflection as measured by the satellites. Additional alternative implementation approaches are available, for example, using the derived monthly mean aerosol information and MODIS retrieved surface albedo, however, in this case the TOA reflection might not be maintained. Summary of feasible implementation schemes is presented in Table 5.1. Among all schemes, B scheme is most physically complete and internally consistent and as such, will serve as the newly updated version.

[7] Introduction of MODIS surface albedo data can be found in Appendix B.2.

Table 5.1 Selected schemes to evaluate updated UMD SRB model.

Scheme code	Activity
Original	Original UMD SRB model directly driven by ISCCP D1 data
Scheme A	Updated model directly driven by ISCCP D1 data
Scheme B	Similar to scheme A, except the clear-sky composite is replaced by the 31-day moving medians of clear radiance
Scheme C	Retrieving surface albedo only with AOD equal to provided monthly mean value
Scheme D	Retrieving AOD only, with surface albedo taken from MODIS retrievals

5.4.2 Implementation results

(a) Daily aerosol optical depth at 0.55 μm

The UMD SRB model based estimates of aerosol optical depths are compared with AERONET measurements for the simulation period (year 2001). Figure 5.3 shows the scatter plots of $\tau_{0.55\mu m}$ derived from five schemes against AERONET observations, where collocated data are grouped at bin size of 0.02 using measurements from 129 stations. Overall statistics of the comparisons are listed in Table 5.2 in terms of bias, standard deviation of the difference and correlation coefficient.

Table 5.2 Statistics of comparisons between model-derived daily aerosol optical depths at 0.55 μm and AERONET measurements for the year 2001.

Scheme code	Bias	Standard Deviation	Correlation Coefficient
Original	0.2038	0.3140	0.3399
Scheme A	0.1368	0.2830	0.4571
Scheme B	0.0457	0.2374	0.4532
Scheme C	-0.0136	0.1634	0.6178
Scheme D	0.1780	0.3617	0.3597

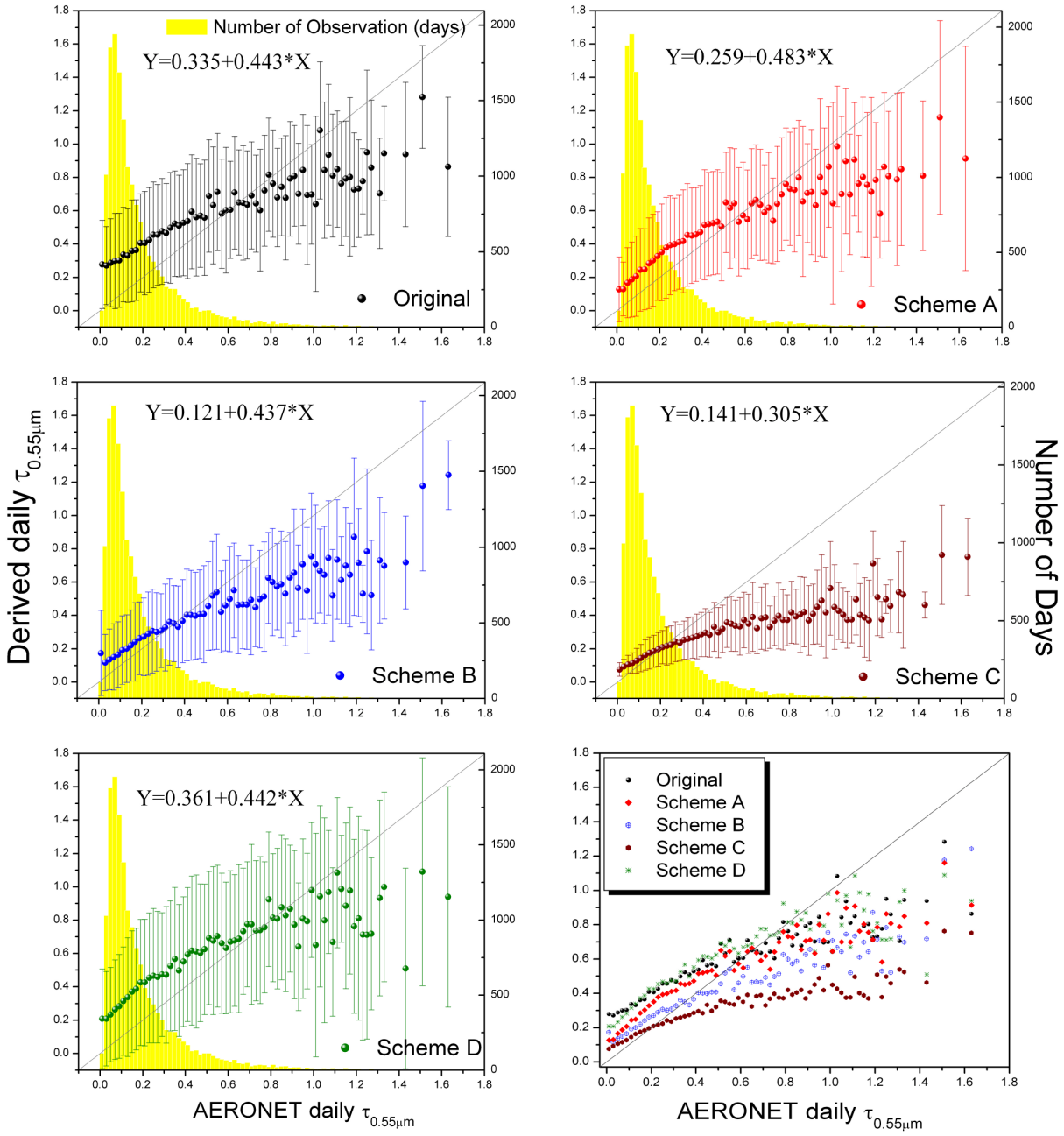

Figure 5.3 Comparison of daily aerosol optical depth at 0.55 μm derived from SRB model with AERONET measurements for the year 2001. Data are grouped at 0.02 bin size according to the measurements. Displayed are the mean values and standard deviations as well as the number of observations within each bin. Composite of the results from five model runs is shown at the right bottom panel.

Original model overestimates $\tau_{0.55\mu m}$ for the low and medium concentration cases where majority of observations are. Overall bias as high as 0.2 can be attributed to the assumption about the average $\tau_{0.55\mu m}$ over land (0.23 invariant over space and time) and possible negative bias of ISCCP clear-sky composite. With updated aerosol procedures, scheme A improves the quality of the retrieved $\tau_{0.55\mu m}$; yet, substantial positive bias (0.14) remains. Further modification of the clear-sky composite (scheme B) reduces the bias to 0.05, but significant standard deviations (0.24) and low correlation (0.45) remain. Using MODIS albedo data (scheme D) does not improve the derived $\tau_{0.55\mu m}$ much, which supports the sensitivity test result that AOD retrieval is very sensitive to the surface reflection (section 3.2). Scheme C results in minimal bias (-0.01) and standard deviation (0.16) as well as highest correlation coefficient (0.62)); however, significant underestimations are present for the large AOD cases.

A more detailed evaluation of the model's capability to detect daily AOD variations is carried out on a station-by-station basis. Figure 5.4 presents the time series of model-derived (scheme B) and AERONET measured daily $\tau_{0.55\mu m}$ at 10 locations, which have a wide geographical coverage and relatively long observation records. Merged monthly mean values (scheme C) as well as ISCCP cloud fraction are also displayed. Missing data for the model results are due to the lack of clear pixels within the grid box when cloud amount is 100%. As evident, certain episodic events are successfully identified by the model. For example, urban emissions in GSFC and Mexico City; biomass burning at Alta Floresta and Mongu; dust outbreaks

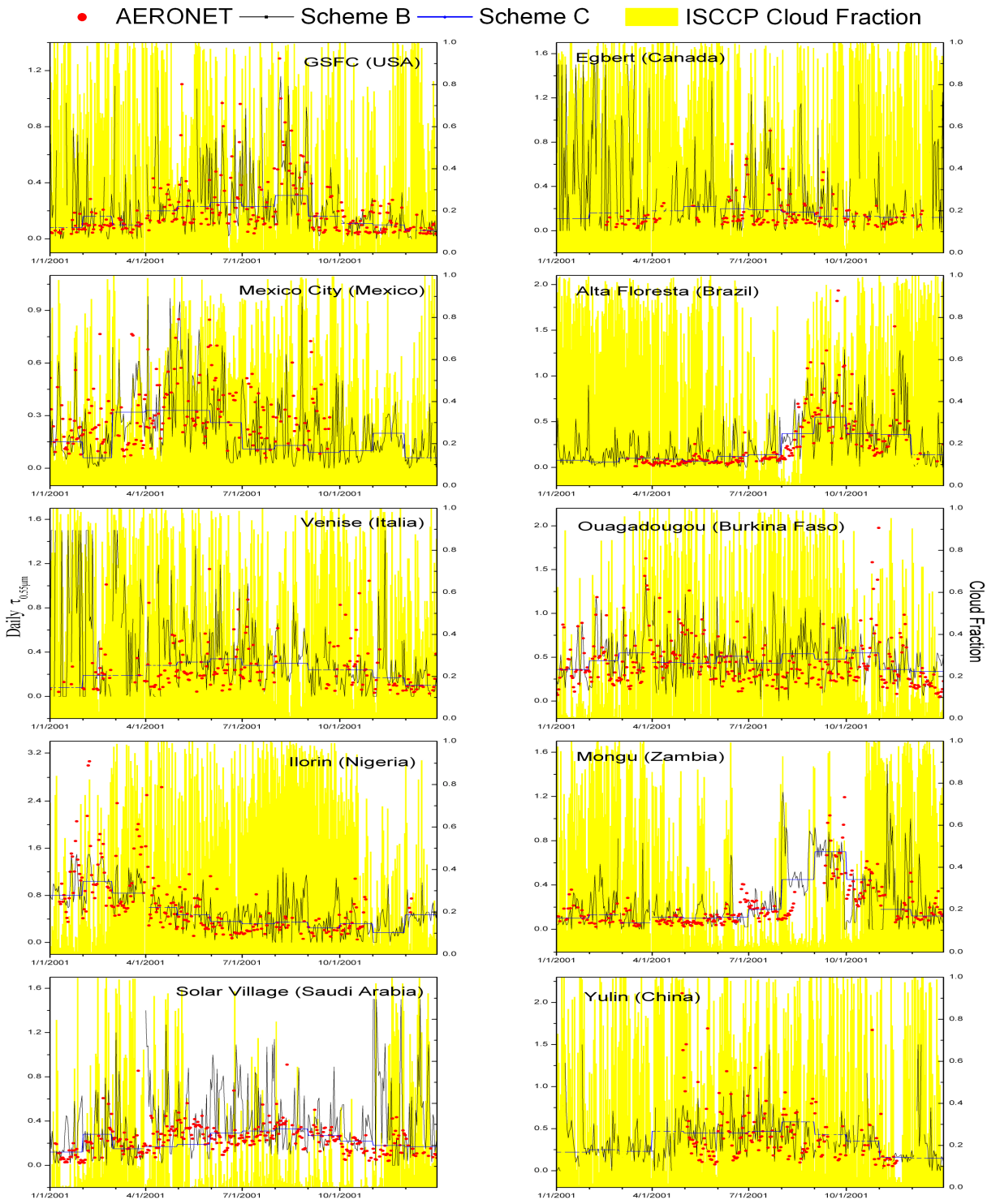

Figure 5.4 Time series of model-derived (scheme B) and AERONET daily aerosol optical depth at 0.55 μm at various stations (year 2001). Merged monthly mean $\tau_{0.55\mu m}$ (scheme C) and ISCCP cloud amount are also displayed.

in Ilorin and Ouagadougou (preset upper limit of 1.5 for the retrieved $\tau_{0.55\mu m}$ leads to the incapability to detect large magnitude of dust AOD); however, dubious fluctuations of $\tau_{0.55\mu m}$ also remain. Following factors may affect the quality of model derived AOD: 1) cloud detection errors; 2) uncertainties in narrow-to-broadband conversion and angular corrections; 3) difficulties associated with simultaneous estimation of AOD and surface reflectance over rapidly varying land and water condition Large $\tau_{0.55\mu m}$ during winter time at Egbert and Venise illustrate this problem. Furthermore, difficulties to detect clouds over snow/ice exacerbate this problem.

(b) Surface downward SW fluxes

Collocated ground measurements of SW global, direct and diffuse irradiance from 31 BSRN stations[8] for the year 2001 (Table 5.3) are used to assess the impact of the various model modifications. If measurements of both direct and diffuse irradiance are available, their sum is used to estimate global horizontal irradiance to avoid the directional response problems [*Flowers and Maxwell*, 1986; *Ohmura et al*., 1998; *Michalsky et al*., 1999]. Otherwise, measurements from unshaded pyranometer are employed. If only global and one partial irradiance (direct or diffuse) are present, the other one will be derived as the difference of the former two.

In Figure 5.5 mean differences of daily fluxes between model results and BSRN measurements are plotted as functions of ISCCP cloud fraction (binned at 0.05

[8] Introduction of BSRN dataset is presented in Appendix B.5.

Table 5.3 BSRN stations (year 2001) with their surface solar irradiance measurements being used for evaluating model results.

Index	Station Name	Longitude	Latitude	Altitude (m)
	Australia			
1	Alice Springs	133° 53' E	23° 48' S	547
	Middle East			
2	Solar Village	46° 25' E	24° 55' N	650
	Africa			
3	Tamanrasset	5° 31' E	22° 47' N	1385
4	Ilorin	4° 34' E	8° 32' N	350
5	De Aar	24° 00' E	30° 40' S	1287
	North America			
6	Goodwin Creek*	89° 52' W	34° 15' N	98
7	Billings§†	97° 31' W	36° 36' N	318
8	S. Great Plains ARM Ext. Facil. 13§	97° 30' W	36° 36' N	318
9	Desert Rock*	116° 1' W	36° 39' N	1007
10	Chesapeake Light Station	75° 43' W	36° 54' N	34
11	Boulder	105°00' W	40° 03' N	1557
12	Bondville*	88° 22' W	40° 04' N	213
13	Boulder*	105° 14' W	40° 08' N	1689
14	Rock Springs*	77° 56' W	40° 43' N	376
15	Fort Peck*	105° 06' W	48° 19' N	634
	Europe			
16	Payerne	6° 57' E	46° 49' N	491
17	Camborne	5° 19'W	50° 13' N	88
18	Lindenberg	14° 07' E	52° 13' N	125
19	Toravere	26° 28' E	58° 16' N	70
20	Lerwick	1° 11' W	60° 08' N	84
	Islands			
21	Lauder	169° 41' E	45° 00' S	350
22	Manus Island§	147° 26' E	2° 03' S	6
23	Nauru Island§	166° 55' E	0° 31' S	7
24	Kwajalein	167° 44' E	8° 43' N	10
25	Bermuda	64° 46' W	32° 18' N	30
26	Tateno	140° 08' E	36° 03' N	25
	Polar Regions			
27	South Pole	24° 48' W	89°59' S	2800
28	Georg von Neumayer	8° 15' W	70° 39' S	42
29	Syowa	39° 35' E	69° 00' S	18
30	Barrow	156° 36' W	71° 19' N	8
31	Ny Ålesund	11° 57' E	78° 56' N	11

* *also facilitate to the Surface Radiation Budget Network (SURFRAD)*

§ *also facilitate to the Atmospheric Radiation Measurement (ARM) program*

† *also known as Cloud And Radiation Testbed (CART) site*

interval). For the relatively clear cases, schemes with improved estimations of AOD tend to have a higher positive bias in the global SW fluxes. For example, scheme B and C yield average biases of 10.48 and 10.76 Wm^{-2} respectively for the cases where cloud fractions less than 50%, while the bias of the original result is only-0.82 Wm^{-2}.

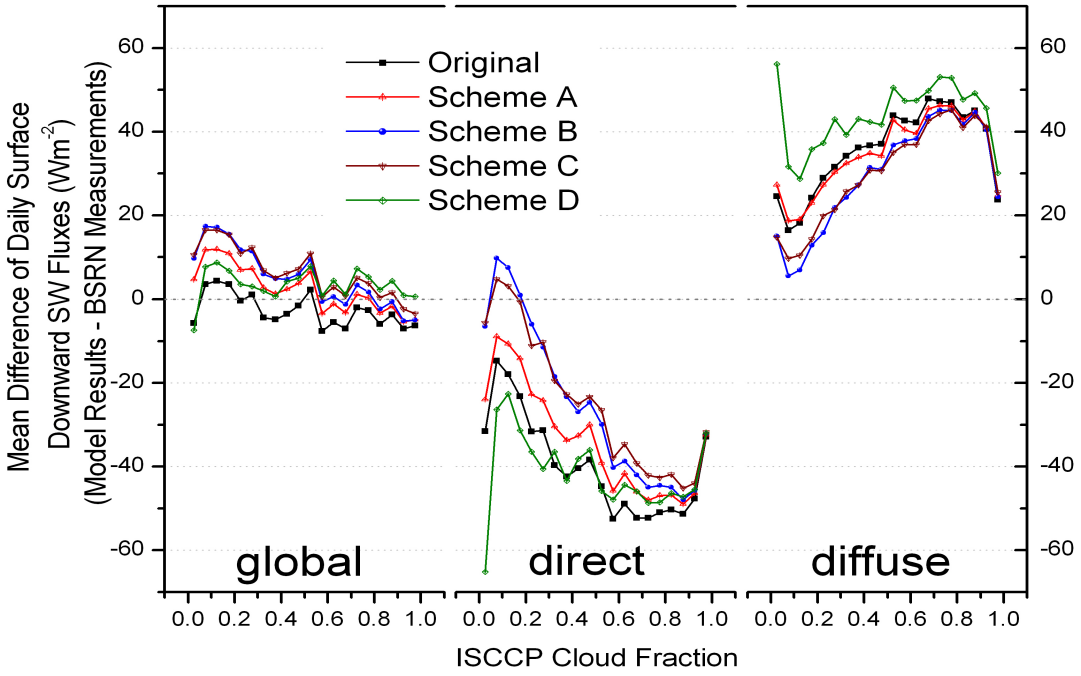

Figure 5.5 Averaged difference of daily surface downward shortwave global/direct/diffuse fluxes between model results and BSRN measurements (from 31 stations in year 2001) as functions of ISCCP cloud fraction (binned at 0.05 intervals).

To aid in diagnosing this discrepancy, estimates of the partial fluxes are also examined. Since direct fluxes are associated with aerosol optical depth by Beer's law, improved estimates of $\tau_{0.55\mu m}$ should result in improved direct fluxes. Indeed, reduced biases were found for scheme B and C (-8.29 and -9.69 Wm^{-2} compared with -31.16 Wm^{-2} for original model results). Remaining negative bias can explained by the general overestimation of AOD for the majority cases (Figure 5.3) as well as

inaccurate estimation of cloud optical depth. In terms of diffuse irradiance, there is an improvement of the mean bias (19.24 and 19.38 Wm^{-2} for scheme B and C compared with 27.88 Wm^{-2} for original model results). The apparent inconsistency of improved partial fluxes in comparison with the global ones can be attributed to possible underestimation of aerosol absorption, overestimation of aerosol forward scattering, problematic satellite inputs and sub-grid effects due to incompatible spatial domain (280km grid averages versus point measurements). It is also of interest to revisit the decade-long controversy about unexplained enhanced SW atmospheric and cloud absorption due to the model observation discrepancy of 10–25 Wm^{-2} [*Cess et al.*, 1995; *Ramanathan et al.*, 1995; *Pilewskie and Valero*, 1995, *Stephens, 1996*, *Li et al*., 1995, 2004; *Conant et al*., 1997, *Arking*, 1996; *Valero et al.*, 1996; *Kato et al*., 1997]. Investigations have revealed that clear sky direct solar flux measurements generally agree well with model calculations [*Halthore et al*., 1997], yet model calculations underestimate the globally averaged diffuse solar radiation by 17 Wm^{-2} [*Halthore et al*., 1998, *Halthore and Schwartz*, 2000]. Further studies reveal that, due to pyranometer negative thermal offsets, there can be an underestimation of diffuse irradiation by 8 to 20 Wm^{-2} [*Bush et al*., 2000; *Heaffelin et al*., 2001; *Dutton et al*., 2001; *Philipona*, 2002]. As such, with presently available measurements, it might not be possible to resolve the systematic positive bias found in the updated SRB model results.

To evaluate model performance against ground truth on a station-by-station basis: 1) Daily surface SW fluxes (global, direct, diffuse) as derived with both the original and B schemes are compared to observations at 31 BSRN stations

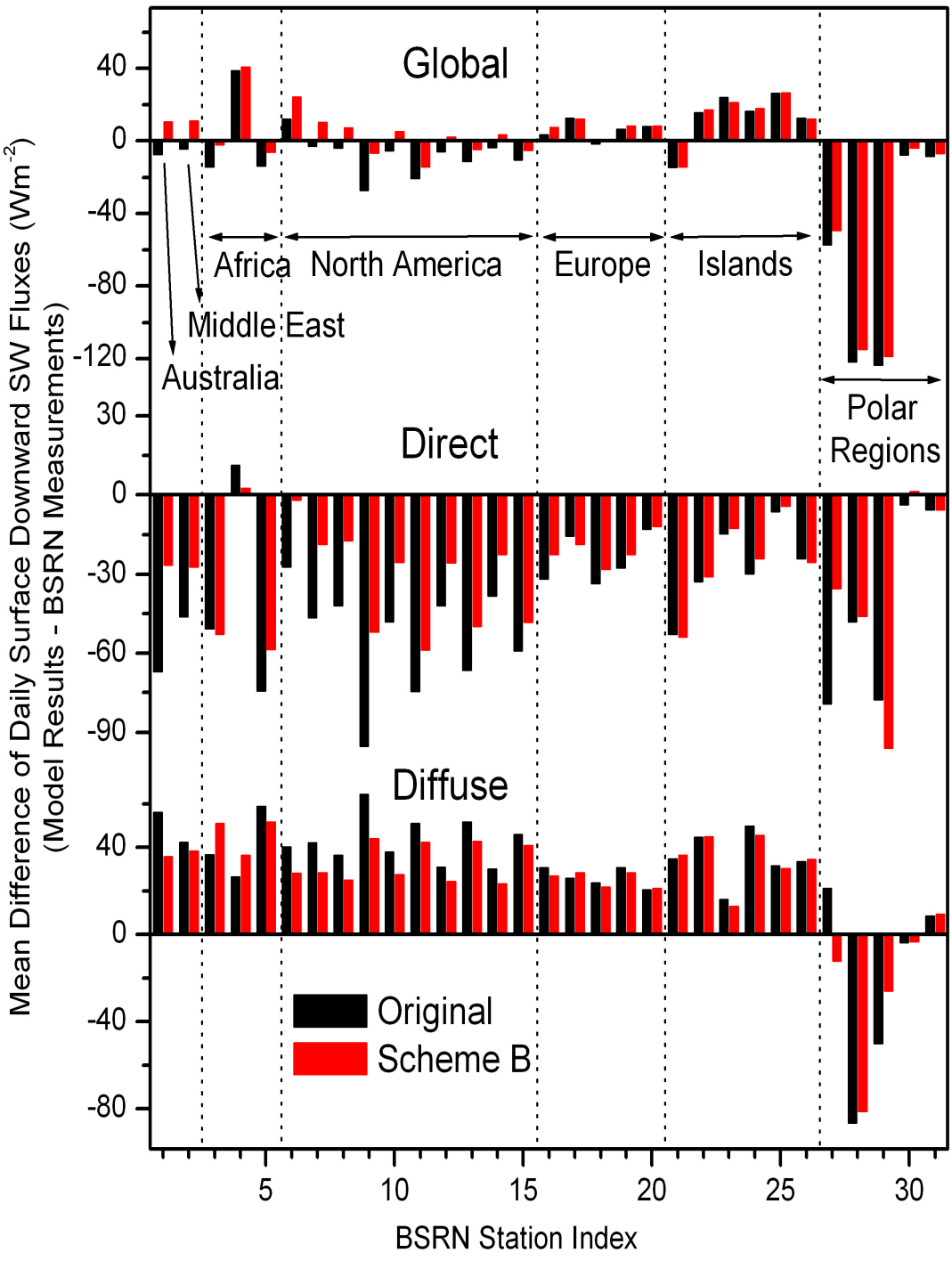

Figure 5.6 Averaged difference of daily surface downward shortwave global/direct/diffuse fluxes between model results (scheme B) and BSRN measurements at 31 stations (year 2001). (BSRN station name and location can be found in Table 5.3)

(Figure 5.6). 2) Four stations with relatively low percentage of clouds are selected for a more detailed illustration (Figure 5.7). Averaged over all stations, bias of total SW flux is reduced to -3.26 Wm^{-2} (updated) from -9.32 Wm^{-2} (original). Improvements of the partial fluxes are also evident: about 11 Wm^{-2} (-29.58 Wm^{-2} compared with original -40.57 Wm^{-2}) for the direct and 4 Wm^{-2} (24.31 Wm^{-2} from 28.31Wm^{-2}) for the diffuse part.

Large errors in the Polar Regions can be attributed to the less certain satellite inputs (difficult to detect cloud over bright and cold surfaces) [*Rossow and Schiffer*, 1991] and the inadequacy of plane parallel assumption in the radiative transfer calculations for large solar zenith angles.

Negligible improvements at island sites are due to the low aerosol concentrations over the ocean, to begin with. Sub-grid scale effects might explain the consistent significant errors among all these stations [*Whitlock et al*., 1995].

For the European sites, differences in irradiance estimations are insignificant, possibly due to the dominance of clouds (averaged ISCCP daytime cloud fraction is more than 70%) and adequate assumption about aerosol properties in the original model.

Over North America, improvements in the direct and diffuse irradiance estimations are seen for all 10 stations. The high density of observing sites in this region provides an opportunity to assess sub-grid effects. One pair of BSRN sites near Boulder is found in a single ISCCP D1 grid cell; the annually averaged global irradiances for these two sites differ by 8.67 Wm^{-2}. For another pair of adjacent sites (Billings and South Great Plains) the difference is 6.03 Wm^{-2} (only nine month of

collocated measurements). Therefore, sampling uncertainties should be taken into consideration for the interpretation of comparison results.

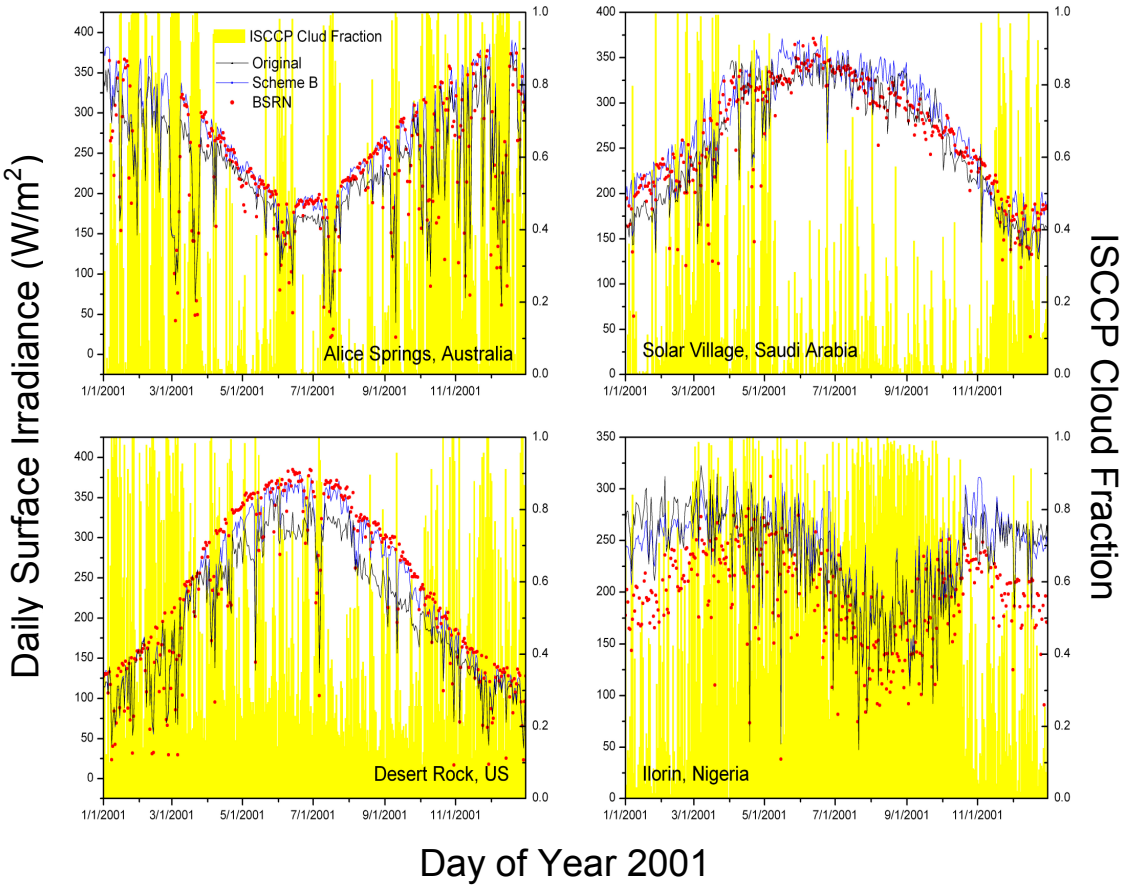

Figure 5.7 Time series of model estimated daily surface irradiance (original and scheme B) and BSRN measurements at four stations with less amount of cloud.

From the three stations located in the northern, central and southern parts of Africa, we focus on Ilorin where dust outbreaks and biomass burnings in the dry season (roughly from November to February) result in a significant aerosol signal. However, model results reveal high positive bias for the global irradiance, which is above possible sampling and measurement uncertainties and can be attribute to the

large overestimations during dry season (Figure 5.7). Scatter plots of surface irradiance and $\tau_{0.55\mu m}$ against measurements are presented in Figure 5.8 with different colors associated with three time periods (Jan.-Feb., Mar.-Oct. and Nov.-Dec.).

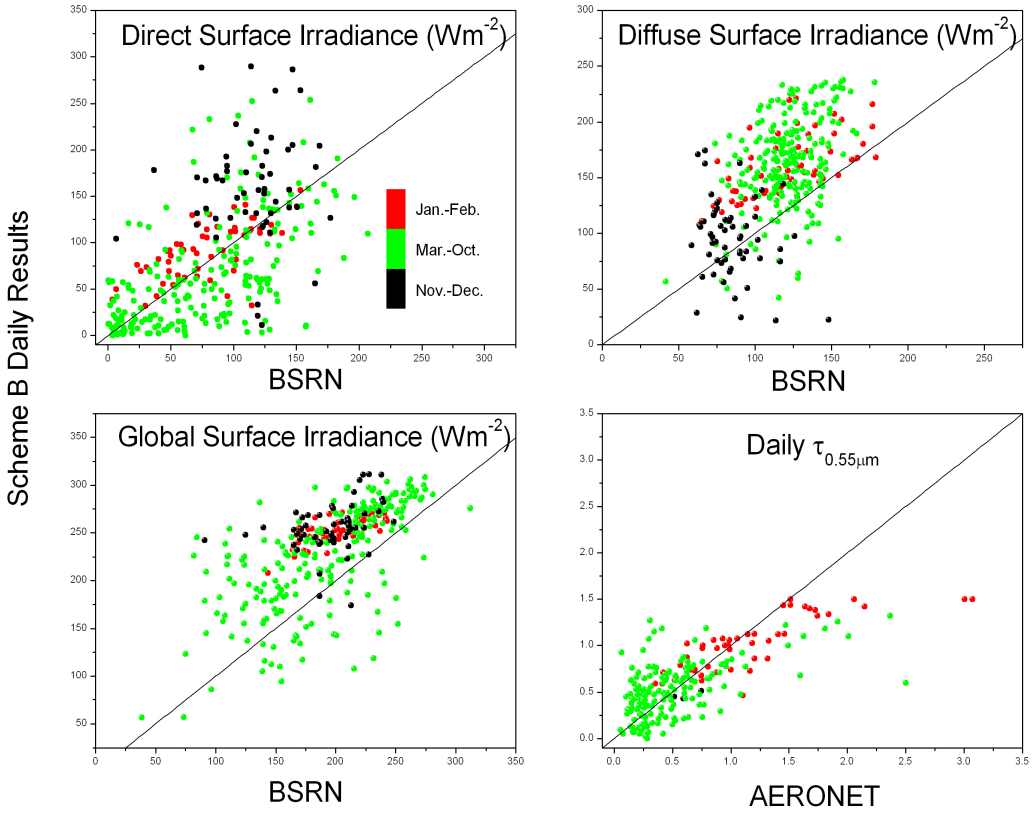

Figure 5.8 Scatter plots of model estimated (scheme B) daily surface irradiance (direct/diffuse/global) and $\tau_{0.55\mu m}$ against BSRN and AERONET measurements at Ilorin.

Similar to Figure 5.5, lower direct and higher diffuse fluxes are evident here for the cloud dominated cases (Mar.-Oct.). For the dry season, overestimation of direct irradiance is obvious with the most serious cases within the Nov.-Dec. period; which might be explained by the underestimation of monthly mean $\tau_{0.55\mu m}$ (0.17 for November and 0.47 for December compared with 0.80 for January and 1.04 for February). Apparent controversy of overestimation of both direct and diffuse fluxes

rises the suspicion that assumed aerosol might not be absorbing enough (estimated $\omega_{0\ 0.55\mu m}$ is about 0.92) or/and less forward scattering (estimated $g_{0.55\mu m}$ is about 0.69). Other explanation could be the cloud contamination which is resulted from mistakenly identifying enhanced aerosol episodes as cloudy scenarios. Such misclassification could also miss certain part of the atmospheric absorptions and generate overestimation of surface irradiance. Detailed analysis has not been performed regarding to this puzzling issue, which calls for the increase of dedicated aerosol measurements around this region.

Great improvement in the estimation of global irradiance for the relatively clear episodes at Alice Springs (Australia) is illustrated in Figure 5.7, where low aerosol loading ($\tau_{0.55\mu m}$ is about 0.1) lead to small diffuse fluxes (about 20 Wm^{-2}) where surface measurements might be less problematic. At Solar Village, another clear-sky dominated station, improvements are obvious in the first three months; however, overestimation of total fluxes is persistent between April and October. Generally, large discrepancies in the clear-sky cases can be found in the diffuse flux, which give rise to the similar suggestion as for the Ilorin case: either aerosol is not absorbing enough (assumed $\omega_{0\ 0.55\mu m}$ is about 0.95) or asymmetry parameter is underestimated (assumed $g_{0.55\mu m}$ is about 0.70).

The standard deviation of the difference (or root-mean square error, RMS) is not improved much in all schemes (generally about 30 Wm^{-2} for the global irradiance, 40 and 30 Wm^{-2} for the direct and diffuse partial fluxes respectively).

(c) Aerosol direct radiative effects

The improved representation of aerosols in the UMD SRB model provides an opportunity to assess their clear-sky direct radiative effects, defined as the reduction of surface SW fluxes due to clear-sky aerosols. Scheme C is used to perform such estimates owing to the good quality of $\tau_{0.55\mu m}$ as used in this scheme (Figure 5.3). As evident from Figure 5.9, the reduction of monthly mean global surface SW radiation follows the pattern of the distribution of aerosol optical depth (Figure 4.14). Depletion of irradiance could be more than 40Wm^{-2} for central Africa during the dry season and for South Africa during the biomass burning period. The dominance of prevailing clear sky conditions over Africa and the Middle East enhances the impact of the aerosols in these regions.

Annual mean reductions of surface downward and net SW fluxes are displayed in Figure 5.10. Globally averaged clear-sky aerosol direct effects are -3.18 and -2.71 Wm^{-2} for the downward and net fluxes respectively. These values are smaller than those derived previously based on simple model estimation (section 3.1) that did not take into account the spatial and temporal variation of the system. Over oceans, annual mean reductions of total irradiance and surface absorption are estimated to be -2.81 and -2.45 Wm^{-2}, while -4.49 and -3.60 Wm^{-2} over lands. Zonal averaged depletions of surface insolation are presented in Figure 5.11, illustrated is that major effects are within 20º S to 40º N due to biomass burning and dusts aerosols. Minimal effects between 60º S to 40º S can be attributed to persistent cloud coverage and small anthropogenic influences.

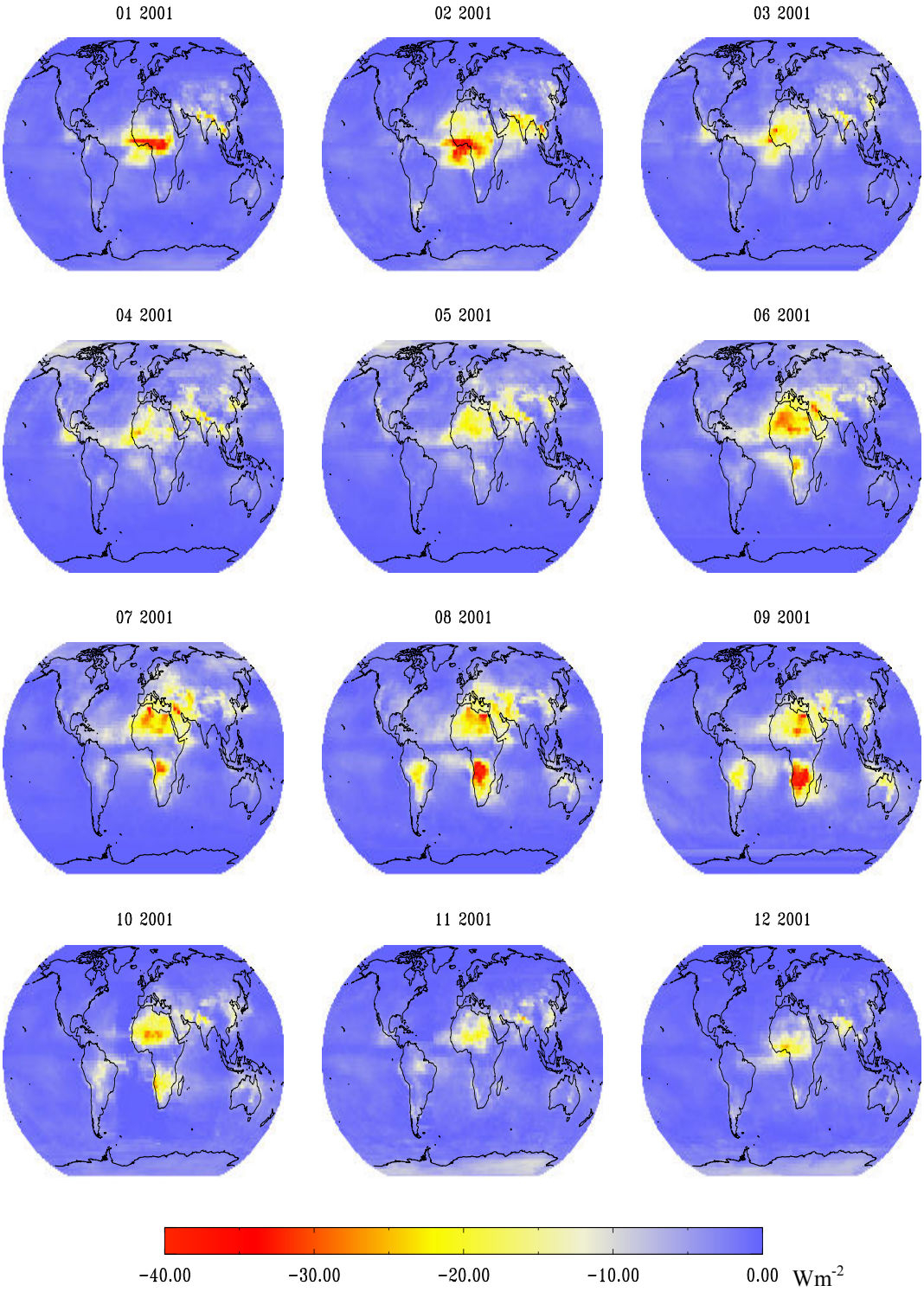

Figure 5.9 Monthly mean depletion of surface isolation (Wm^{-2}) due to clear-sky aerosols for the year 2001.

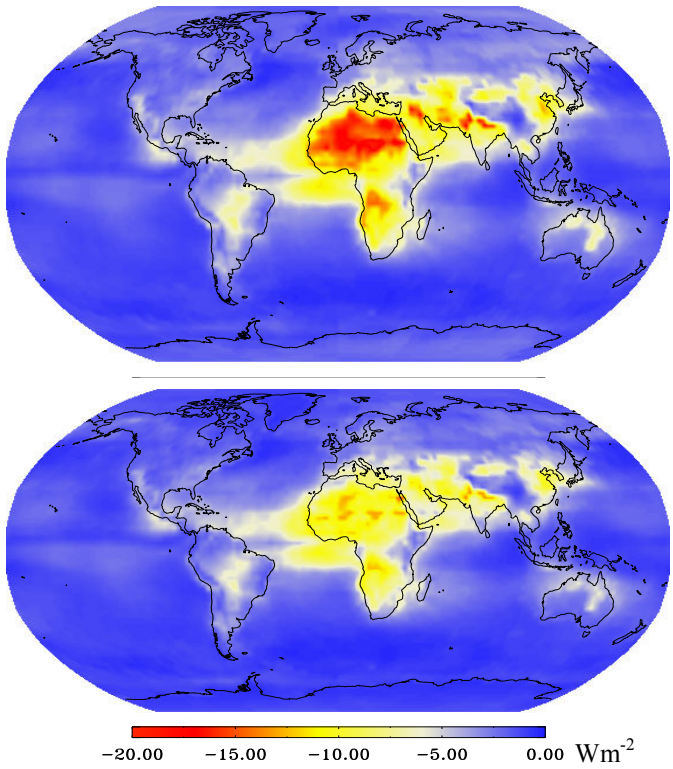

Figure 5.10 Annual mean depletion of surface downward SW fluxes (top) and surface net SW fluxes (bottom) due to clear-sky aerosols for the year 2001.

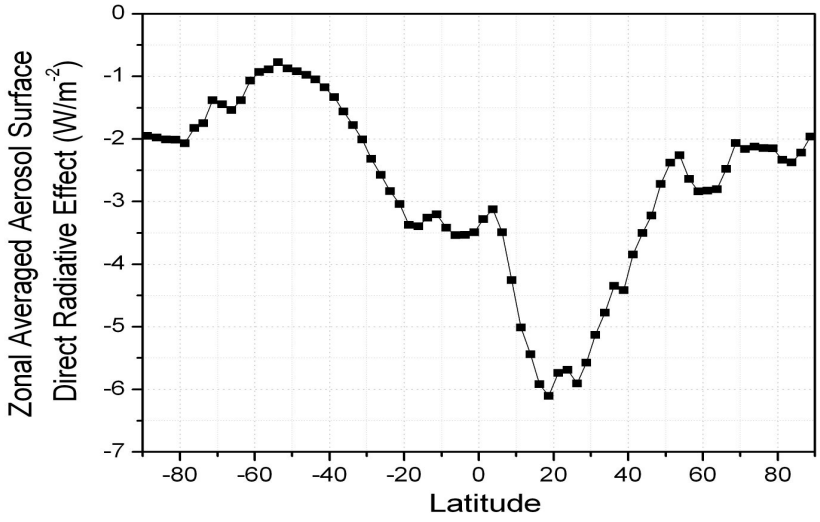

Figure 5.11 Zonal averaged aerosol surface direct radiative effect (depletion of surface insolation due to clear-sky aerosols).

From previous studies, median values of observation-based estimates of annual average of clear-sky aerosol surface forcing (reduction of surface absorption) are reported as -8.8Wm^{-2} over ocean and -11.8Wm^{-2} over land while model-based median values are -4.8 Wm^{-2} and -7.2 Wm^{-2} respectively [*Yu et al*., 2005]. These reported estimates are "theoretical" with an assumed perennial clear-sky scenario; while our results represent the "actual" values corresponding to the realistic distribution of clear-sky scenes. To make our results comparable with the others, the "actual" values are divided by the clear-sky fraction, therefore, -7.7, -8.7 and -8.0 Wm^{-2} are reported as our estimates over ocean, land and the globe.

We also estimated the TOA aerosol direct forcing over the 60º S to 60º N domain (quality of satellite data over high latitudes is still an issue). For "actual" clear-sky cases our estimates are -1.19, -1.90 and -1.31 Wm^{-2} over ocean, land and all region, and -3.88, -4.58 and -4.00 Wm^{-2} for the "theoretical" values. These latter fall within the median values of "theoretical" aerosol TOA direct forcing reported as -3.5/-2.8 (model-based) and -5.5/-4.9 Wm^{-2} (observation-based) over ocean/land.

Compared with other methods used to address aerosol direct effects, an advantage of our scheme is that it preserves closure with TOA satellite measurements. With anticipated improvements in aerosol information and satellite input, the UMD SRB model has the potential to address aerosol radiative effects in a more realistic and coherent (regarding to the closure achieved at both ends of atmosphere) way than the radiative transfer calculations based on independent inputs from various sources.

5.5 Summary

In this chapter, the UMD SRB model is updated in terms of its capability to incorporate a complex representation of aerosol properties and their variability. Aerosol properties derived in this thesis are implementated with ISCCP D1 satellite data for one annual cycle.

Evaluation of performance is in terms of the model's ability to estimate daily $\tau_{0.55\mu m}$ and surface downward SW fluxes. Compared with AERONET measurements from 129 stations, the SRB model with scheme B demonstrates the ability to retrieve detailed AOD variations from the broadband TOA albedo. Overall bias of retrieved AOD at 0.55 μm is reduced to 0.05 compared with 0.20 for the original model results. Using state-of-the-art BSRN surface irradiance measurements, assessment of model estimated surface SW fluxes shows improvements. Averaged over all stations, biases of estimates of surface total, direct and diffuse SW fluxes are reduced by about 7, 11 and 4 Wm^{-2} respectively. UMD SRB model is also expanded with the capability to estimate clear-sky aerosol direct effects. Annually averaged clear-sky direct radiative aerosol forcing is estimated to be -1.31 Wm^{-2} at the top of atmosphere (60º S to 60º N) and -2.71 Wm^{-2} at the surface (global). This indicates that the effect of aerosols on the SW energy absorption is comparable with their effect on the reflection at the TOA. Global annually averaged reduction of surface irradiance is estimated to be -3.18 Wm^{-2} for clear-sky aerosols. These estimates of aerosol direct radiative effects compare favorably with reported studies.

Chapter 6: Summary and discussion

Using available information, a methodology to construct a comprehensive characterization of aerosol properties at global scale was developed. First, utilized was information on aerosol optical depth from a wide range of sources and developed was an approach to merge this information by combining distinctive advantages associated with individual datasets. Due to their high quality, AERONET measurements serve as an anchor to regulate the large-scale spatial and temporal distribution patterns of the GOCART model and MODIS satellite retrievals, using truncated EOF fitting methods. Two-years (March 2000 – February 2002) of global $\tau_{0.55\mu m}$ were used. Merits of this approach can be summarized as: 1) Leading EOFs can retrieve the significant and geographically continuous variation signals from model and satellite data. 2) Fitting leading EOFs to ground observations can propagate the AERONET information in an inhomogeneous and anisotropic manner, with amplitude close to the measurements in a general least-square sense.
3) Truncated EOF fitting is robust and not very sensitive to possible sampling errors in ground observations. Limitations: 1) The approach is statistical in nature; assumptions can be only partially tested due to the limited amount of high quality monthly mean, grid area averaged AOD datasets. 2) Propagation of AERONET information in the time dimension is not implemented. *Kaplan et al.* [1997] propose a first-order linear Markov model to provide further constrains on temporal amplitudes. (A reliable model of this type can be constructed only with an expanded database of collocated data). 3) More realistic observation operator might ameliorate the regional representativeness of AERONET point measurements. It is hoped that

the full potential of the proposed approach would be achieved when longer term information from independent sources becomes available.

Estimations of aerosol intensive properties are also undertaken. Aerosol single scattering albedo over the solar spectrum is estimated based on GOCART simulation results at 0.55 μm and spectral variation revealed from AERONET almucantar retrievals; wavelength resolved asymmetry parameters are calculated from MODIS Ångström exponents based on an empirical relationship derived from AERONET sky-radiance retrievals; normalized aerosol extinction coefficients are estimated from MODIS Ångström exponents to create a complete global description of spectral variation of aerosol optical depth, absorption and scattering properties. Comparison of empirically derived asymmetry parameters and normalized extinction coefficients with GOCART extensive simulation results in five SW spectral bands shows differences, which warrants future efforts to reduce the uncertainties associated with aerosol intensive properties.

To incorporate effectively aerosol information into satellite algorithms to infer surface SW fluxes, the aerosol impact on the relationship between TOA and surface radiation budget needs to be fully understood. Initially, sensitivity tests were performed to address this issue. It was learned that ambient aerosols have significant surface effects, depending on aerosol concentrations, absorbing and scattering properties. Variation of aerosol properties greatly affects the relationship between TOA and surface radiation budget. Detailed aerosol information that includes aerosol optical depth, single scattering albedo and asymmetry parameter, as well as a

adequate schemes are needed for incorporation of such effects into satellite-based SRB estimation..

Update of the lookup table technique of the UMD SRB model expands model capability to dynamically incorporate complex variation of aerosol intensive properties, which is important since realistic variations of aerosol parameters cannot be adequately characterized with a limited number of aerosol models. Implementation of the new information on aerosols in the modified version of the SRB model is performed with ISCCP D1 data for one year period. Compared with AERONET measurements, positive biases (about 0.2) of daily $\tau_{0.55\mu m}$ as estimated from the original version of the model are largely reduced (to about 0.05 for the dynamical scheme B). Also, demonstrated was the capability to capture daily variation of aerosol optical depth. Comparison of surface downward SW fluxes with BSRN measurements shows improvements (about 7 Wm^{-2} for the total; 11 and 4 Wm^{-2} for the direct and diffuse parts); To explain the remaining biases (about -3.26 Wm^{-2} for the total; -29.58 and 24.31 Wm^{-2} for direct and diffuse SW fluxes), possible underestimation of diffuse fluxes by measurements can not be ruled out; updates on the cloud schemes and additional improvements in aerosol scattering and absorption properties are also needed. Further assessment of sub-grid effects shows that the difference of annually averaged surface irradiance between two closely located sites can be as large as 8.7 Wm^{-2}. It is worth emphasizing that strict validation of satellite-derived fluxes is nearly impossible since point ground measurements can at best yield only a reasonable estimate of the true quantity at satellite spatial scales. However, the

updates performed here on the representation of aerosols resulted in improved estimation of atmospheric optical parameters, which is progress in the right direction.

The new aerosol formulation in the UMD SRB provides capabilities to assess aerosol direct radiative effects. Annually averaged reduction of surface downward and net SW fluxes due to aerosols under clear-sky conditions was estimated to be -3.18 and -2.71 Wm^{-2} respectively. For the TOA aerosol direct forcing, increase of SW reflection due to actual clear-sky aerosols is estimated as 1.31 Wm^{-2}. Converted to the "theoretical" perennial clear-sky cases, our estimates of aerosol direct forcing is -4.0 and -8.0 Wm^{-2} at the TOA and surface. Compared with previous studies, our results fall within the median values reported from satellite and model-based methods.

Our estimated total aerosol direct TOA effect is comparable with the projected 3.7 Wm^{-2} TOA forcing due to a doubling of CO_2 [IPCC, 2001]. However, since natural and anthropogenic material can be mixed in a single particle, evaluation of the contribution from anthropogenic aerosols is still a challenge. Using MODIS retrieved fine mode fraction of AOD as a proxy of anthropogenic aerosol contribution, *Kaufman et al.* [2005] estimated that about 21% of total aerosol optical depth over ocean had an anthropogenic origin. Based on present satellite retrievals over land it is not easy to separate the anthropogenic part from the natural component. Compared with the natural particles (e.g., dust and sea salt), anthropogenic aerosols tend to be smaller (stronger reflection) and more absorbing. These two characteristics have opposite effects at the TOA, but strengthen each other at the surface to yield a strong

reduction of irradiance. To assess aerosol effects on climate change requires additional information from in-situ measurements and model simulations.

In brief, aerosol information from different sources is utilized to achieve a unique global description of aerosol radiative properties. The resulting information is evaluated in the framework of an inference scheme to estimate surface radiative fluxes from satellites. For this end, first, the relationship between SW surface fluxes and TOA planetary albedo (the satellite input) is investigated and sensitivity tests explored the effect of aerosols on this relationship. Subsequently, the inference model was modified to allow the incorporation of the new information on aerosols and the new version was implemented for one annual cycle using the ISSCP satellite data. Compared with ground measurements, improvements in model performance are demonstrated. It is anticipated that implementation of this approach with future satellite observations at finer spatial scales and with better capabilities to detect clouds will demonstrate expected improvements of the inference scheme.

Appendices

A. Derivations

A.1 Derivation of Eqs. (2.7) and (2.8)

From Eq. (2.4) we get:

$$\frac{R_s(\mu_0)T_a^{dir}(\mu_0)+\tilde{R}_s\,T_a^{dif}(\mu_0)}{1-\tilde{R}_s\,\tilde{R}_a}=\frac{r-R_a(\mu_0)}{\tilde{T}_a} \tag{A.1.1}$$

Substituting Eq. (A.1.1) in Eq. (2.5):

$$\begin{aligned} t &= T_a^{dir}(\mu_0)+\left(T_a^{dif}(\mu_0)+\frac{\tilde{R}_a}{\tilde{T}_a}\left(r-R_a(\mu_0)\right)\right) \\ &= \left(T_a^{dir}(\mu_0)+T_a^{dif}(\mu_0)-\frac{\tilde{R}_a}{\tilde{T}_a}R_a(\mu_0)\right)+\frac{\tilde{R}_a}{\tilde{T}_a}r \end{aligned} \tag{A.1.2}$$

Substituting Eq. (A.1.1) in Eq. (2.6):

$$n=\left(1-R_s(\mu_0)\right)T_a^{dir}(\mu_0)+\left(1-\tilde{R}_s\right)\left(T_a^{dif}(\mu_0)+\frac{\left(R_s(\mu_0)T_a^{dir}(\mu_0)+\tilde{R}_s\,T_a^{dif}(\mu_0)\right)\tilde{R}_a}{1-\tilde{R}_s\,\tilde{R}_a}\right)$$

$$=\left(T_a^{dir}(\mu_0)+T_a^{dif}(\mu_0)\right)-\left(1-\tilde{R}_a\right)\frac{\left(R_s(\mu_0)T_a^{dir}(\mu_0)+\tilde{R}_s\,T_a^{dif}(\mu_0)\right)}{1-\tilde{R}_s\,\tilde{R}_a}$$

$$=\left(T_a^{dir}(\mu_0)+T_a^{dif}(\mu_0)\right)-\frac{\left(1-\tilde{R}_a\right)}{\tilde{T}_a}\left(r-R_a(\mu_0)\right)$$

$$= \left(T_a^{dir}(\mu_0) + T_a^{dif}(\mu_0) + \frac{\left(1-\tilde{R}_a\right)}{\tilde{T}_a} R_a(\mu_0) \right) - \frac{\left(1-\tilde{R}_a\right)}{\tilde{T}_a} r \qquad \text{(A.1.3)}$$

Using the relationship: $T_a^{dir}(\mu_0) + T_a^{dif}(\mu_0) + R_a(\mu_0) + A_a(\mu_0) = 1$ and $\tilde{T}_a + \tilde{R}_a + \tilde{A}_a = 1$,

where $A_a(\mu_0)$ is the atmospheric absorption over a nonreflecting surface, and $\tilde{A}_a$ is the atmosphere spherical absorption (for the surface reflected radiation), Eqs. (A.1.2) and (A.1.3) become:

$$t = \left(1 - A_a(\mu_0) - \frac{1-\tilde{A}_a}{\tilde{T}_a} R_a(\mu_0) \right) + \left(\frac{1-\tilde{A}_a}{\tilde{T}_a} - 1 \right) r \qquad \text{(A.1.4)}$$

$$n = \left(1 - A_a(\mu_0) + \frac{\tilde{A}_a}{\tilde{T}_a} R_a(\mu_0) \right) - \left(1 + \frac{\tilde{A}_a}{\tilde{T}_a} \right) r \qquad \text{(A.1.5)}$$

A.2 Derivation of Eqs. (2.9) and (2.10)

For a Lambertian surface with surface albedo being R_s :

$$r = R_a(\mu_0) + \frac{R_s T_a(\mu_0) \tilde{T}_a}{1 - R_s \tilde{R}_a} \qquad \text{(A.1.6)}$$

$$t = \frac{T_a(\mu_0)}{1 - R_s \tilde{R}_a} \qquad \text{(A.1.7)}$$

$$n = (1 - R_s) t \qquad \text{(A.1.8)}$$

Using the relationship $T_a(\mu_0) + R_a(\mu_0) + A_a(\mu_0) = 1$, from Eq. (A.1.6) we have:

$$T_a(\mu_0) = \frac{1 - A_a(\mu_0) - r}{1 - \dfrac{\tilde{R}_s \tilde{T}_a}{1 - \tilde{R}_s \tilde{R}_a}} \qquad \text{(A.1.9)}$$

Substituting Eq. (A.1.9) into Eq. (A.1.7-8) and utilizing $\tilde{T}_a + \tilde{R}_a + \tilde{A}_a = 1$:

$$t = \frac{1 - A_a(\mu_0) - r}{1 - R_s \tilde{R}_a - R_s \tilde{T}_a} = \frac{1 - A_a(\mu_0) - r}{1 - R_s\left(1 - \tilde{A}_a\right)} \qquad \text{(A.1.10)}$$

$$n = (1 - R_s)t = (1 - R_s)\frac{1 - A_a(\mu_0) - r}{1 - R_s\left(1 - \tilde{A}_a\right)} \qquad \text{(A.1.11)}$$

B. Datasets

B.1 GOCART model simulations

The GOCART (Global Ozone Chemistry Aerosol Radiation and Transport) model developed by Georgia Institute of Technology and NASA GSFC is a three-dimensional chemical transport model with a horizontal resolution of 2.5^o in longitude by 2^o in latitude and 20-30 vertical layers. [*Chin et al.,* 2000, 2002*; Ginoux et al.,* 2001] In the model, key types of aerosols (sulfate, dust, organic carbon, black carbon and sea salt) are separately simulated and the total aerosol optical depth is the summation of all the components. Global simulation of aerosol characteristics remains a challenge due to the diversity of aerosols emission mechanisms, complexity of processes undergone in their lifetime, and large variability of their physical, optical and chemical properties. [*Kinne et al.,* 2001, 2003*; Penner et al.,* 2002]. As a forward model to provide the needed AOD information, GOCART estimates the emissions of the key types of aerosols and their precursors based on the state-of-the-art fossil/bio-fuel combustion; biomass burning; surface topographic features databases and the background meteorological condition is taken from Goddard Earth Observing System Data Assimilation System (GEOS DAS); the chemical reactions (DMS and SO_2 oxidation et al.), transportation mechanisms (advection, diffusion and convection) and aging and removing processes (clustering, gravitational settling, wet deposition, washing-out et al.) are built in the model to simulate the aerosol evolvement. Dry aerosol mass M_d for each aerosol component is calculated, aerosol optical parameters are assumed to provide the mass extinction efficiency β, which

describes a linear relationship between the dry aerosol mass and the AOD at specified wavelength, and actually is a complicated function of aerosol size distribution, shape, complex refractive index, and ambient humidification condition. Most of these processes are highly parameterized and could be the sources of error. The relative contributions to the error are not known because the quantitative estimation of the error is difficult due to the paucity of high quality data sets that are coherent in temporal and geographical variability [*Kinne et al.,* 2001, 2003*; Penner et al.,* 2002]. Evaluation of GOCART AOD against AVHRR and TOMS retrievals and AERONET ground observations has demonstrated that the model has the capability to reproduce prominent spatial and temporal variations, especially in areas with strong signals (biomass burning and dust dominant). [*Chin et al.,* 2002] Compared with the combined satellite retrievals from MODIS and TOMS, GOCART tends to underestimate the optical depth while has comparable intercontinental transport of carbon and dust [*Kinne et al.,* 2003].

Aerosol intensive properties, particle density, size distribution and complex refractive index were taken from Global Aerosol Data Set (GADS [*Köpke et al*. 1997]). Homogeneous spherical assumption enables Mie calculations to create a comprehensive lookup table. External mixing is used to composite various components into ambient aerosols.

B.2 MODIS satellite retrievals

The MODerate resolution Imaging Spectroradiometer (MODIS) onboard the EOS Terra and Aqua polar orbiting satellites is a well designed instrument for AOD retrievals [*Salomonson et al.,* 1989; *King et al*, 1999]. With thirty-six well-calibrated bands, a wide spectral range (from visible to infrared) of radiance observations provided is an opportunity for implementing more accurate cloud screening algorithms and for determining surface reflectance across the solar spectrum. Benefiting from the high spatial resolution and near daily global coverage, MODIS improved are the chances to monitor global aerosol characteristics with a relatively high accuracy.

The retrievals of AOD using multi-spectral signals from MODIS are performed separately over ocean and land. [*Kaufman et al.,* 1997; *Tanré et al*, 1997]. Over land, multi-spectral cloud mask is used for screening out cloudy pixels; [*Ackerman et al*, 1998]. Dark target technique is used to determine surface reflectance. It is based on the observation that dark surface reflectance at the blue and red channels (0.47 μm and 0.66 μm) is well correlated with that at the two shortwave infrared channels (2.1 μm and 3.8 μm). Aerosol models are dynamically selected and weighted, AOD is retrieved from the look-up table given the aerosol properties and geometry information. Major error sources for the retrieval over land could be attributed to sub-pixel cloud contamination, inaccurate surface reflectance estimation, and inappropriate aerosol models. Evaluation of three months level-2 ($10\text{km} \times 10\text{km}$) land AOD product with AERONET data shows that retrievals are within the expected error range ($\pm 0.05 \pm 0.2\tau$) for the wavelengths at 470 *nm* and 660 *nm* , with root-

mean-square error below 0.1 for inland and 0.2-0.3 for coasts, which might be a result of heterogeneous surface condition [*Chu et al*, 2002]. Over the oceans, surface reflectance at different wavelength is calculated based on the available ocean models and information or assumption on the wavelength dependence. Cloud screening is based on the spatial variability strategy in combination with the cloud masking algorithm used over the land, [*Martins et al*, 2002]. Taking advantage of the relative homogeneous surface condition of ocean, and the observation that aerosol usually display a more homogeneous spatial distribution on a scale of few kilometers than clouds, this algorithm gives a satisfactory improvement. Five fine modes and six coarse mode aerosol models are built in the look-up table, selection and relative contribution is decided by the least-square best fit to the multi-spectral path radiance. Validation of about six months level-2 ocean AOD product with AERONET observations shows that retrievals are well within the expected error uncertainties ($\pm 0.03 \pm 0.05\tau$), with standard error being about 0.02 for the wavelengths at $660nm$ and $870nm$ [*Remer et al.*, 2002].

Surface Bidirectional Reflectance Distribution Function (BRDF) (and albedo) has also been derived from MODIS measurements based on a semi-empirical kernel-driven model [*Wanner et al.*, 1997; *Lucht et al.*, 2000; *Schaaf et al.*, 2002]. MOD43B1 BRDF/Albedo model parameter product provides the weighting parameters ($f_{iso}, f_{vol}, f_{geo}$) for each of the MODIS spectral channels as well as for three broad bands (0.3-0.7μm, 0.7-5.0μm, and 0.3-5.0μm). The integrated black-sky albedos ($\alpha_{bs}(\theta, \lambda)$, direct beam directional hemispherical reflection) and white-sky

albedos ($\alpha_{ws}(\lambda)$, diffuse bi-hemispherical reflection) can be calculated based on the formulations:

$$\begin{aligned}\alpha_{bs}(\theta,\lambda) = & f_{iso}(\lambda)\left(g_{0,iso} + g_{1,iso}\theta^2 + g_{2,iso}\theta^3\right) + \\ & f_{vol}(\lambda)\left(g_{0,vol} + g_{1,vol}\theta^2 + g_{2,vol}\theta^3\right) + \\ & f_{geo}(\lambda)\left(g_{0,geo} + g_{1,geo}\theta^2 + g_{2,geo}\theta^3\right)\end{aligned} \quad \text{(A.2.1)}$$

$$\alpha_{ws}(\lambda) = f_{iso}(\lambda)g_{iso} + f_{vol}(\lambda)g_{vol} + f_{geo}(\lambda)g_{geo} \quad \text{(A.2.2)}$$

Comparison with SURFRAD and CART/SGP measurements shows that the MODIS surface albedo generally meets an absolute accuracy requirement of 0.02 during April–September 2001, while larger discrepancies appear in the winter season probably due to the presence of snow [*Jin et al.*, 2003].

B.3 AERONET ground observations

The AERONET [*Holben, et al.,* 1998] is a globally distributed federated network of ground-based observations representing a wide variety of atmospheric conditions. AERONET imposes standardization for measurement protocol, data processing and calibration, and uses the weather-resistant automatic CIMEL sun-sky radiometer with approximately a 1.2º full angle field of view, which enable frequent measurements of atmospheric aerosol optical properties at remote sites. The radiometer makes two basic measurements, either direct sun radiation or sky radiation. The direct sun measurements are made in (up to) eight spectral bands (340, 380, 440, 500, 670, 870, 940, and 1020nm) and provide the AOD retrievals. With the information from sky-scanning measurements, size distributions, optical parameters and non-sphericity can be reliably estimated [*Dubovik and King,* 2000*; Dubovik et*

al., 2000]. A consistent, reproducible and system-wide cloud screening procedure is applied, which is based on the observation that rapid temporal AOD variations are attributed to the presence of clouds [*Smirnov, et al.,* 1999]. Since the retrieval of the AOD from the measurements of the spectral extinction of solar direct beam is straight forward (Beer's law), AERONET AOD product has the highest accuracy. Assessments of the possible errors due to calibration uncertainties and inaccuracy in ozone absorption and Rayleigh scattering calculations show that total uncertainty of AOD is about 0.01 to 0.02 for a field instrument [*Holben et al.,* 1998*; Eck et al.,* 1999]. With such high accuracy, AERONET data are regarded as a "benchmark" and extensively used for the evaluations and radiative effects calculation.

Aerosol intensive parameters, microphysical (size distribution) and optical constants (complex reflective index) are retrieved based on optimal statistical analysis [*Dubovik and King*, 2000; *Dubovik et al.*, 2000; 2002]. Sky-radiances at multi-wavelenght (0.44; 0.67; 0.87 and 1.02μm) and mult-iangles combined with estimated AOD and various a priori constraints serve as multi-source data with predetermined accuracy. Search for best fit is carried out by maximum likelihood method. Success of retrievals demands homogeneous clear-sky conditions (radiances from at least 21 out of 27 scattering angles are symmetric on both sides of the sun), high aerosol loadings ($\tau_{0.44\mu m}$ >0.4) and large solar zenith angles (≥45º). Given the infrequency of sky radiance measurements (made at optical air masses of 4, 3, and 2 in the morning and afternoon, and once per hour in between) and strict qualification requirements, such retrievals are limited in the number of samplings and biased to the enhanced concentration cases. Based on sensitivity studies, accuracy of retrievals is estimated

as 0.03 for the single scattering albedo; 15-25% for the volume size distribution between 0.1 and 7μm (25-100% for the particles smaller than 0.1μm and larger than 7μm); 0.04 for the real part of refractive index and 30% (50%) for imaginary part of strongly (weakly) absorbing aerosols. Moreover, artifacts of overestimation of small particle numbers (<0.1μm) and strong spectral dependence of the real part of the refractive index are associated with non-spherical dust aerosols if spherical shape is assumed, therefore, spheroid particle assumption retrieval has been developed to address this challenge.

B.4 ISCCP stage D1 data

The ISCCP D1 product is a global, calibrated and normalized radiance data-set [*Rossow et al*., 1996], which is derived from the pixel-level DX data with 3-hour temporal resolution and 280km by 280km equal-area grid size. Up to five geostationary satellites and two polar orbiting satellites are used to obtain complete global coverage. Visible calibration gives a scaled radiance for each geosynchronous and sun synchronous instrument which are normalized relative to the AVHRR visible channel [*Rossow et al*. 1987, *Desormeaux et al*. 1993]. In addition, ancillary data are also included to facilitate the radiative transfer analysis: atmospheric temperature and humidity profiles and column ozone amount are taken from TIROS Operational Vertical Sounder (TOVS) atmosphere gridded data product; sea ice cover data are from the analyses by U.S. Navy (before 1991) and National Snow and Ice Data Center (after 1991); snow cover data are provided by Synoptic Analysis Branch at NOAA.

Table A.1 Parameters from ISCCP D1 data used by UMD SRB model

Geometry & satellite information	***Radiance***
Solar zenith angle (cosine)	Clear scaled radiance
Satellite Zenith angle (cosine)	Cloudy scaled radiance
Relative azimuth angle	Clear-sky composite scaled radiance
Satellite ID	
Cloud amount information	***Atmospheric data***
Number of total pixels	Column amount of water vapor
Number of cloud pixels	Column amount of ozone
	Snow/ice cover (in percentage)

Twelve parameters from ISCCP D1 dataset, which are relevant to the SW flux estimation and used by UMD SRB model, are listed in Table A.1.

The cloud detection procedure based on threshold tests on spatial and temporal variations of radiances (IR, VIS and NIR if polar orbit satellite data are used) is used to decide whether a satellite pixel is cloudy or clear. Cloud amount for each grid cell is calculated as the ratio of the number of cloudy pixels over total pixels. Scaled radiances are calculated by dividing the measured radiance by the solar constant at the mean earth-sun distance. Assuming a characteristic distribution mode associated with clear radiance, clear-sky composite scaled radiance is simply determined by increasing the minimum value (over time period of 5, 15 or 30 days according to the surface type and latitude) by an amount representing the typical separation of the

minimum and the mean value. Five predetermined values (0.050, 0.035, 0.015, 0.030 and 0.060) are specified for different types of surface, further refinements are introduced to eliminate the unrealistic values.

B.5 BSRN surface SW flux measurements

International Baseline Surface Radiation Network (BSRN), initiated by the World Climate Research Program (WCRP), was developed to provide earth's surface irradiance measurements for validating satellite-based estimates of the surface radiation budget, improving radiative transfer calculations of climate model and detecting long-term trends in radiative fluxes at the surface [*Ohmura et al.*, 1998; http://bsrn.ethz.ch/] at over 40 stations in contrasting climatic zones, surface solar global and partial (direct and diffuse) irradiance is measured with instruments of the highest available accuracy at a very high frequency (minutes). Aiming to acquire the most accurate possible in situ surface radiation measurements, dedicated efforts have been carried out to improve the calibration and measurement capabilities by establishing standard protocols and central organization.

The performance and accuracy of broadband shortwave instruments, such as pyrheliometer and pyranometer, to measure downwelling solar radiation has been an important issue for BSRN scientists. A number of questions were raised in this respect, especially because of the hot-debated issue on unexplained enhanced absorption of shortwave radiation in clear sky atmospheres as well as in clouds. In addition to the uncertainty in the absolute calibration of the instrument, other factors might significantly degrade the quality of measurements: 1) solar-tracking errors and

cleaning of the radiometer surface; 2) varying sensitivity to irradiance as a function of incident angle, called “cosine response error”; 3) detector sensitivity to the gradient of temperature within the instrument, referred to as “thermal offset problem”. Although BSRN recommended the use of the component summation method, in which total isolation is estimated indirectly by the summation of direct irradiance measured by the pyrheliometer and diffuse measurements by a shaded pyranometer to avoid the directional responses problem, uncorrected thermal offsets might still introduce a systematic 8-20 Wm^{-2} underestimation of diffuse sky radiation [*Philipona*, 2002].

C. Acronyms

ABI	Advanced Baseline Imager
ACE	Aerosol Characterization Experiments
ADEOS	Advanced Earth Observing Satellite
AERONET	AErosol RObotic NETwork
AOD	Aerosol Optical Depth
ARIES	Airborne Research Interferometer Evaluation System
ASYM	ASYMmetry parameter
ATSR	Along-Track Scanning Radiometer
AATSR	Advanced Along-Track Scanning Radiometer
AVHRR	Advanced Very High Resolution Radiometer
BRDF	Bidirectional Reflectance Distribution Function
BSRN	Baseline Surface Radiation Network
CALIOP	Cloud-Aerosol Lidar with Orthogonal Polarization
CALIPSO	Cloud-Aerosol Lidar and Infrared Pathfinder Satellite Observations
CART/SGP	Cloud And Radiation Testbed–Southern Great Plains
CLAMS	Chesapeake Lighthouse and Aircraft Measurements for Satellites
CNES	Centre National d'Etudes Spatiales (France)
DOE	Department Of Energy
EARLINET	European Aerosol Research Lidar Network
ECHAM	European Centre/Hamburg Model
ETM+	Enhanced Thematic Mapper Plus
EUMETSAT	European Organization for the Exploitation of Meteorological Satellites

GADS	Global Aerosol Data Set
GISS	Goddard Institute for Space Studies
GFDL	Geophysical Fluid Dynamics Laboratory
GLI	Global Imager
GOCART	Global Ozone Chemistry Aerosol Radiation and Transport model
GOES	Geostationary Operational Environmental Satellite
GSFC	Goddard Space Flight Center (NASA)
ICARTT	International Consortium for Atmospheric Research on Transport and Transformation
IMPACT	Integrated Massively Parallel Atmospheric Chemical Transport model
INTEX-NA	Intercontinental Chemical Transport Experiment - North America
ISCCP	International Satellite Cloud Climatology Project
LACE	Lindenberg Aerosol Characterization Experiment
LANDSAT	LAND remote sensing SATellite
Lidar	LIght Detection and Ranging
MATCH	Model of Atmospheric Transport and Chemistry
MBL	Marine Boundary Layer
MISR	Multi-angle Imaging Spectroradiometer
MIRAGE	Model for Integrated Research on Atmospheric Global Exchange
MODIS	Moderate Resolution Imaging Spectroradiometer
MOZART	Model for OZone And Related chemical Tracers
MPLNET	Micro Pulse Lidar Network
MSG	Meteosat Second Generation
NASA	National Aeronautics and Space Administration
NCAR	National Center for Atmospheric Research

NCEP	National Centers for Environmental Prediction
NIR	Near InfRared
NOAA	National Oceanic and Atmospheric Administration
NPOESS	National Polar-orbiting Operational Environmental Satellite System
OCTS	Ocean Color and Temperature Scanner
OMI	Ozone Monitoring Instrument
OPAC	Optical Properties of Aerosol and Clouds
PAR	Photosynthetically Active Radiation
PARASOL	Polarization and Anisotropy of Reflectances for Atmospheric Sciences Coupled with Observations from Lidar
POLDER	Polarization and Directionality of the Earth's Reflectance
PRIDE	Puerto Rico Dust Experiment
RH	Relative Humidity
SBDART	Santa Barbara DISORT Atmospheric Radiative Transfer
SCAR-A	Smoke, Clouds, and Radiation experiments – Atlantic region
SCAR-B	Smoke, Clouds, and Radiation-Brazil
SCF	Squared Covariance Function
SEVIRI	Spinning Enhanced Visible and Infrared Imager
SHADE	SaHAran Dust Experiment
SPRINTARS	Spectral Radiation-Transport Model for Aerosol Species
SRB	Surfaces Radiation Budget
SSA	Single Scattering Albedo
SSM/I	Special Sensor Microwave Imager
SURFRAD	SURFace RADiation budget network

SWIR	ShortWave InfRared
TARFOX	Tropospheric Aerosol Radiative Forcing Observational Experiment
TOMS	Total Ozone Mapping Spectrometer
TOVS	TIROS Operational Vertical Sounder
TRACE-P	TRansport And Chemical Evolution over the Pacific
WCRP	World Climate Research Program

Bibliography

Ackerman, S. A., O. B. Toon, D. E. Stevens, A. J. Heymsfield, V. Ramanathan, and E. J. Welton (2000), Reduction of tropical cloudiness by soot, *Science, 288*, 1042-1047.

Albrecht, B. A. (1989), Aerosols, cloud microphysics and fractional cloudiness, *Science, 245*, 1227-1230.

Alfaro, S. C., et al. (2003), Chemical and optical characterization of aerosols measured in spring 2002 at the ACE-Asia supersite, Zhenbeitai, China, *J. Geophys. Res., 108*(D23), 8641, doi:10.1029/2002JD003214.

Alfaro, S. C., S. Lafon, J. L. Rajot, P. Formenti, A. Gaudichet, and M. Maille (2004), Iron oxides and light absorption by pure desert dust: An experimental study, *J. Geophys. Res., 109*, D08208, doi:10.1029/2003JD004374.

Anderson G. P., J. H. Chetwynd, J. M. Theriault, P. K. Acharya, A. Berk, D. C. Robertson, F. X. Kneizys, M. L. Hoke, L. W. Abreu and E. P. Shettle (1993), MODTRAN2: Suitability for Remote Sensing," *Proceedings of the SPIE, 1984, Remote Sensing*.

Anderson, T. L., S. J. Masonis, D. S. Covert, N. C. Ahlquist, S. G. Howell, A. D. Clarke, and C. S. McNaughton (2003), Variability of aerosol optical properties derived from in situ aircraft measurements during ACE-Asia, *J. Geophys. Res., 108*(D23), 8647, doi:10.1029/2002JD003247.

Ångström, A. (1929), On the atmospheric transmission of Sun radiation and on dust in the air, *Geogr. Ann., 12*, 130-159.

Ansmann, A., U. Wandinger, A. Wiedensohler, and U. Leiterer (2002), Lindenberg Aerosol Characterization Experiment 1998 (LACE 98): Overview, *J. Geophys. Res., 107*(D21), 8129, doi:10.1029/2000JD000233.

Arking, A. (1996), Absorption of solar energy in the atmosphere: Discrepancy between model and observations, *Science, 273*, 779– 782.

Artaxo, P., E. T. Fernandes, J. V. Martins, M. A. Yamasoe, P. V. Hobbs, W. Maenhaut, K. M. Longo, and A. Castanho (1998), Large-scale aerosol source apportionment in Amazonia. *J. Geophys. Res., 103*(D24), 31,837-31847.

Bahreini, R., J. L. Jimenez, J. Wang, R. C. Flagan, J. H. Seinfeld, J. T. Jayne, and D. R. Worsnop (2003), Aircraft-based aerosol size and composition measurements during ACE-Asia using an Aerodyne aerosol mass spectrometer, *J. Geophys. Res., 108*(D23), 8645, doi:10.1029/2002JD003226.

Barkstrom, B. R. (1984), The Earth Radiation Budget Experiment (ERBE), *Bull. Amer. Meteor. Soc., 65*, 1170-1185.

Bates, T. S.; V. N. Kapustin, P. K. Quinn; D. S. Covert, D. J. Coffman, C. Mari, A. Durkee, W. J. De Bruyn, and E. S. Saltzman (1998), Processes controlling the distribution of aerosol particles in the lower marine boundary layer during the First Aerosol Characterization Experiment (ACE 1), *J. Geophys. Res., 103*(D13), 16,369-16,383.

Bates, T.S., P.K. Quinn, D.J. Coffman, J.E. Johnson, T.L. Miller, D.S. Covert, A. Wiedensohler, S. Leinert, A. Nowak and C. Neusüb (2001), Regional Physical and Chemical Properties of the Marine Boundary Layer Aerosol across the

Atlantic during Aerosols99: An overview, *J. Geophys. Res.*, *106*(D18), 20,767-20,782.
Bergstrom, R. W., P. B. Russel, and P. Hignett (2002), Wavelength dependence of the absorption of black carbon particles: Predictions and results from the TARFOX experiment and implications for the aerosol single scattering albedo. *J. Atmos. Sci*., *59*, 567-577.
Bergstrom, R. W., P. Pilewskie, B. Schmid, and P. B. Russell (2003), Estimates of the spectral aerosol single scattering albedo and aerosol radiative effects during SAFARI 2000, *J. Geophys. Res.*, *108*(D13), 8474, doi:10.1029/2002JD002435.
Bergstrom, R. W., P. Pilewskie, J. Pommier, M. Rabbette, P. B. Russell, B. Schmid, J. Redemann, A. Higurashi, T. Nakajima, and P. K. Quinn (2004), Spectral absorption of solar radiation by aerosols during ACE-Asia, *J. Geophys. Res.*, *109*, D19S15, doi:10.1029/2003JD004467.
Blake, N. J. ; Blake, D. R. ; Wingenter, O. W. ; Sive, B. C. ; Kang, C. H. ; Thornton, D. C. ; Bandy, A. R. ; Atlas, E. ; Flocke, F. ; Harris, J. M. ; Rowland, F. S. (1999). Aircraft measurements of the latitudinal, vertical, and seasonal variations of NMHCs, methyl nitrate, methyl halides, and DMS during the First Aerosol Characterization Experiment (ACE 1*), J. Geophys. Res., 104*(D17), 21,803-21,817.
Bond, T. C., and R. W. Bergstrom (2004), Toward resolution on the optics of light-absorbing carbon. *AGU Fall Meeting*, Dec. 13-17, San Francisco, CA.
Boucher, O. and T. L. Anderson (1995), GCM assessment of the sensitivity of direct climate forcing by anthropogenic sulfate aerosols to aerosol size and chemistry, *J. Geophys. Res.*, *100,* 26,117-16,134.
Boucher, O., and D. Tanré (2000), Estimation of the aerosol peturbation to the Earth's radiative budget over oceans using POLDER satellite aerosol retrievals, *Geophys. Res. Lett., 27(8)*, 1103-1106.
Breon, F., R. Frouin and C. Gautier (1994), Global Shortwave Energy Budget at the Earth's Surface from ERBE Observations, *J. Climate, 7*, 309-324.
Bretherton, C. S., C. Smith, and J. M. Wallace (1992), An intercomparison of methods for finding coupled patterns in climate data*, J. Clim., 5,* 541-560.
Bullrich, K. (1964), Scattered radiation in the atmosphere and the natural aerosol, *Advances in Geophysics, 10*, Academic Press, 99-260.
Bush, B. C., F. P. J. Valero, A. S. Simpson, and L. Bignone (2000), Characterization of thermal effects in pyranometers: A data correction algorithm for improved measurement of surface insolation, *J. Atmos. Oceanic Technol., 17*, 165–175.
Bush, B. C., and F. P. J. Valero (2003), Surface aerosol radiative forcing at Gosan during the ACE-Asia campaign, *J. Geophys. Res., 108*(D23), 8660, doi:10.1029/2002JD003233.
Busch, B., K. Kandler, L. Schutz and C. Neusuß (2002), Hygroscopic properties and water-soluble volume fraction of atmospheric particles in the diameter range from 50 nm to 3.8 Mm during LACE 98. *J. Geophys. Res., 107*(D21), 8119, doi:10.1029/2000JD000228.
Carrico, C. M., P. Kus, M. J. Rood, P. K. Quinn, and T. S. Bates (2003), Mixtures of pollution, dust, sea salt, and volcanic aerosol during ACE-Asia: Radiative

properties as a function of relative humidity, *J. Geophys. Res.*, *108*(D23), 8650, doi:10.1029/2003JD003405.
Castanho, A. D. A., J. V. Martins, P. V. Hobbs, P. Artaxo, L. Remer, and M. Yamasoe (2005), Chemical characterization of aerosols on the East Coast of the United States using aircraft and ground-based stations during the CLAMS experiment. *J. Atmos. Sci.,* 62, 934–946.
Ceballos, J. C., M. J. Bottino, and J. M. de Souza (2004), A simplified physical model for assessing solar radiation over Brazil using GOES 8 visible imagery, *J. Geophys. Res.*, *109*, D02211, doi:10.1029/2003JD003531.
Cess, R.D. (1985), Nuclear war: Illustrative effects of atmospheric smoke and dust upon solar radiation. *Clim. Change*, *7*, 237-251.
Cess, R. D., and I. L. Vulis (1989), Inferring surface solar absorption from broadband satellite measurements*, J. Climate, 2,* 974-985.
Cess, R. D., E. G. Dutton, J. J. Deluisi and F. Jiang (1991), Determining Surface Solar Absorption from Broadband Satellite Measurements for Clear Skies: Comparison with Surface Measurements, *J. Climate*, *4*, 236-247.
Cess, R. D., et al. (1995), Absorption of solar radiation by clouds: Observations versus model, *Science, 267*, 496–499.
Chandrasekhar S. (1960), *Radiative Transfer*, Dover, 393pp.
Charlson, R. J., J. Langner, H. Rodhe, C. B. Leovy, and S. G. Warren (1991), Perturbation of the Northern Hemisphere radiative balance by backscattering from anthropogenic sulfate aerosols, *Tellus, 43AB* , 152-163.
Charlson, R. J., S. E. Schwartz, J. M. Hales, R. D. Cess, J. A. Coakley, Jr., J. E. Hansen, and D. J. Hofmann (1992), Climate forcing by anthropogenic aerosols, *Science, 255*, 423-430.
Charlson, R. J. (2001), Extending atmospheric aerosol measurements to the global scale, IGACtivities, 25, 11– 14.
Chin, M., R. B. Rood, S.-J. Lin, J.-F., Muller, and A. M. Thompson (2000), Atmospheric sulfur cycle simulated in the global model GOCART: Model description and global properties, *J. Geophys. Res.*, *105*, 24,671-24,687.
Chin, M., P. Ginoux, S. Kinne, O. Torres, B. Holben, B. N. Duncan, R. V. Martin, J. A. Logan, A. Higurashi, and T. Nakajima (2002), Aerosol distributions and radiative properties simulated in the GOCART model and comparisons with observations, *J. Atmos. Sci., 59*, 461-483.
Chin, M., D. A. Chu, R. Levy, L. Remer, Y. Kaufman, B. Holben, T. Eck, P. Ginoux, and Q. Gao (2004), Aerosol distribution in the Northern Hemisphere during ACE-Asia: Results from global model, satellite observations, and Sun photometer measurements. *J. Geophys. Res.*, *109*(D23), doi: 10.1029/2004GL02014.
Chowdhary, J., B. Cairns and L. D. Travis (2002), Case studies of aerosol retrievals over the ocean from multiangle, multispectral photopolarimetric remote sensing data. *J. Atmos. Sci., 59*, 383–397.
Chowdhary, J., B. Cairns, M.I. Mishchenko, P.V. Hobbs, G.F. Cota, J. Redemann, K. Rutledge, B.N. Holben, and E. Russell (2005), Retrieval of aerosol scattering and absorption properties from photopolarimetric observations over the ocean during the CLAMS experiment. *Journal of the Atmospheric Sciences*, 62:1093-1117.

Christopher, S. A., J. Wang, Q. Ji, and S.-C. Tsay (2003), Estimation of diurnal shortwave dust aerosol radiative forcing during PRIDE, *J. Geophys. Res., 108*(D19), 8596, doi:10.1029/2002JD002787.

Chuang, C. C., and J. E. Penner (1995), Effects of anthropogenic sulfate on cloud drop nucleation and optical properties, *Tellus*, *47B*, 566-577.

Chuang, C. C., J. E. Penner, K. E. Taylor, A. S. Grossman, and J. J. Walton (1997), An assessment of the radiative effects of anthropogenic sulfate, *J. Geophys. Res.*, *102*, 3761-3778.

Chuang, C.C., D.J. Bergmann, J.E. Dignon and P.S. Connell (2001), Global Modeling of Tropospheric Aerosols by LLNL IMPACT and Comparisons with Field Measurements. American Geophysical Union, Fall Meeting, San Francisco, Dec. 10–14, 2001, UCRL-JC-145282-ABS.

Chylek P. and J. Wong (1995), Effect of Absorbing Aerosols on Global Radiation Budget, *Geophys. Res. Lett., 22*, 929-931.

Clarke, A. D., et al. (2002), INDOEX aerosol: A comparison and summary of chemical, microphysical, and optical properties observed from land, ship, and aircraft, *J. Geophys. Res.*, *107*(D19), 8033, doi:10.1029/2001JD000572.

Clarke, A. D., et al. (2004), Size distributions and mixtures of dust and black carbon aerosol in Asian outflow: Physiochemistry and optical properties, *J. Geophys. Res.*, *109*, D15S09, doi:10.1029/2003JD004378.

Coakley, J. A., Jr., and P. Chylek (1975), The two-stream approximation in radiative transfer: Including the angle of the incident radiation, *J. Atmos. Sci., 32*, 61-70.

Collins, W. D., P. J. Rasch, B. E. Eaton, D. W. Fillmore, J. T. Kiehl, C. T. Beck, and C. S. Zender (2002), Simulation of aerosol distributions and radiative forcing for INDOEX: Regional climate impacts, *J. Geophys. Res.*, *107*(D19), 8028, doi:10.1029/2000JD000032.

Conant, W. C., V. Ramanathan, F. P. J. Valero (1997), and J. Meywerk, An examination of the clear-sky solar absorption over the central equatorial pacific: Observations versus models, *J. Clim., 10*, 1874–1884.

Conant, W. C., J. H. Seinfeld, J. Wang, G. R. Carmichael, Y. Tang, I. Uno, P. J. Flatau, K. M. Markowicz, and P. K. Quinn (2003), A model for the radiative forcing during ACE-Asia derived from CIRPAS Twin Otter and R/V *Ronald H. Brown* data and comparison with observations, *J. Geophys. Res., 108*(D23), 8661, doi:10.1029/2002JD003260.

Daley, R. (1991), *Atmospheric Data Analysis.* Cambridge University Press, New York, 457pp, ISBN 0-521-38215-7.

Darnell, W. L., W. F. Staylor, S. K. Gupta, and F. M. Denn (1998), Estimation of surface insolation using Sun-synchronous satellite data, *J. Climate, 1*, 820-835.

Darnell, W. L., W. F. Staylor, S. K. Gupta, N. A. Ritchey, and A. C. Wilberx (1998). Seasonal variation of surface radiation budget derived from ISCCP-C1 data, *J. Geophys. Res., 97,* 15741-15760.

Dedieu, G., P. Y. Deschamps and Y. H. Kerr (1987), Satellite Estimation of Solar Irradiance a the Surface of the Earth and of Surface Albedo Using a Physical Model Applied to Meteosat Data, *J. Climate Appl. Meteor.*, *26*, 79-87.

Desormeaux, Y., W. B. Rossow, C. L. Brest, and C. G. Campbell (1993), Normalization and calibration of geostationary satellite radiances for ISCCP. *J. Atmos. Ocean Tech., 10*, 304-325.

Deuzé, J. L., P. Goloub, M. Herman, A. Marchand, G. Perry, and D. Tanré (2000), Estimate of the aerosol properties over the ocean with POLDER. *J. Geophys. Res., 105*, 15,329–15,346.

Deuzé, J. L., F. M. Bréon, C. Devaux, P. Goloub, M. Herman, B. Lafrance, F. Maignan, A. Marchand, F. Nadal, G. Perry and D. Tanré (2001), Remote sensing of aerosols over land surfaces from POLDER-ADEOS-1 polarized measurements, *J. Geophys. Res.*, *106,* 4913-4926.

Diak, G. R. and C. Gautier (1983), Improvements to a simple physical model for estimating insolation from GOES data, *J. Appl. Meteor*., *22*, 505-508.

Diner, D.J., J.C. Beckert, T.H. Reilly, C.J. Bruegge, J.E. Conel, R. Kahn, J.V. Martonchik, T.P. Ackerman, R. Davies, S.A.W. Gerstl, H.R. Gordon, J-P. Muller, R. Myneni, R.J. Sellers, B. Pinty, and M.M. Verstraete (1998), Multi-angle Imaging SpectroRadiometer (MISR) description and experiment overview. *IEEE Trans. Geosci. Rem. Sens.*, *36 (4)*. 1072-1087.

Diner, D. J., et al. (2004), PARAGON: An integrated approach for characterizing aerosol climate impacts and environmental interactions, *Bull.Am. Meteorol. Soc., 85*, 1491–1501.

Dubovik, O., B. N. Holben, Y. J. Kaufman, M. Yamasoe, A. Smirnov, D. Tanré, and I. Slutsker (1998), Single scattering albedo of smoke retrieved from the sky radiance and solar transmittance measured from ground. *J. Geophys. Res., 103*, 31,903–31,923.

Dubovik, O. and M. D. King (2000a), A flexible inversion algorithm for retrieval of aerosol optical properties from Sun and sky radiance measurements, *J. Geophys. Res.*, *105*, 20,673-20,696.

Dubovik, O., A. Smirnov, B. N. Holben, M. D. King, Y. J. Kaufman, T. F. Eck, and I. Slutsker (2000b), Accuracy assessments of aerosol optical properties retrieved from AERONET sun and sky-radiance measurements, *J. Geophys. Res*., 105, 9791-9806.

Dubovik, O., B. N. Holben, T. F. Eck, A. Smirnov, Y. J. Kaufman, M. D. King, D. Tanré, and I. Slutsker (2002), Variability of absorption and optical properties of key aerosol types observed in worldwide locations, *J. Atmos. Sci.,* 59, 590-608.

Dutton, E. G., J. J. Michalsky, T. Stoffel, B. W. Forgan, J. Hickey, D. W. Nelson, T. L. Alberta, and I. Reda (2001), Measurements of broadband diffuse solar irradiance using current commercial instrumentationwith a correction for thermal offset errors, *J. Atmos. Oceanic Technol., 18*, 297– 314.

Ebert, M., S. Weinbruch, A. Rausch, G. Gorzawski, P. Hoffmann, H. Wex, and G. Helas (2002), Complex refractive index of aerosols during LACE 98 as derived from the analysis of individual particles, *J. Geophys. Res.*, *107*(D21), 8121, doi:10.1029/2000JD000195.

Eck, T. F., B. N. Holben, I. Slutsker and A. Setzer (1998), Measurements of irradiance attenuation and estimation of aerosol single-scattering albedo for biomass burning aerosols in Amazonia. *J. Geophys. Res., 103*(D24), 31,865-31,878.

Eck, T.F., B.N. Holben, J.S. Reid, O. Dubovik, A. Smirnov, N.T. O'Neill, I. Slutsker, and S. Kinne (1999), Wavelength dependence of the optical depth of biomass burning, urban and desert dust aerosols, *J. Geophys. Res., 104*, 31 333-31 350.

Eck, T. F., et al. (2003), Variability of biomass burning aerosol optical characteristics in southern Africa during the SAFARI 2000 dry season campaign and a comparison of single scattering albedo estimates from radiometric measurements, *J. Geophys. Res.*, *108*(D13), 8477, doi:10.1029/2002JD002321.

Eck, T. F., B. N. Holben, O. Dubovik, A. Smirnov, P. Goloub, H. B. Chen, B. Chatenet, L. Gomes, X. Y. Zhang, S. C. Tsay, Q. Ji, D. Giles, and I. Slutsker (2005), Columnar aerosol optical properties at AERONET sites in central eastern Asia and aerosol transport to the tropical mid-Pacific, *J. Geophys. Res.*, *110*, D06202, doi:10.1029/2004JD005274.

Fillmore, D.W., and W.D. Collins (2002), Global aerosol distributions from a chemical transport model with MODIS assimilation. American Geophysical Union, Fall Meeting, San Francisco, California, Dec. 6-10, 2002. *EOS Trans. AGU* , vol. 83 (no.47), p. F124.

Fischer, H., D. Wagenbach, and J. Kipfstuhl (1998), Sulfate and nitrate firn concentrations on the Greenland ice sheet: 2. Temporal anthropogenic deposition changes, *J. Geophys. Res., 103*(D17), 21927-21934.

Flowers, E. C., and E. L. Maxwell (1986), Characteristics of network measurements. *Sol. Cells, 18*, 205–212.

Formenti, P., W. Elbert, W. Maenhaut, J. Haywood, and M. O. Andreae (2003a), Chemical composition of mineral dust aerosol during the Saharan Dust Experiment (SHADE) airborne campaign in the Cape Verde region, September 2000, *J. Geophys. Res.,108*(D18), 8576, doi:10.1029/2002JD002648.

Formenti, P., W. Elbert, W. Maenhaut, J. Haywood, S. Osborne, and M. O. Andreae (2003b), Inorganic and carbonaceous aerosols during the Southern African Regional Science Initiative (SAFARI 2000) experiment: Chemical characteristics, physical properties, and emission data for smoke from African biomass burning, *J. Geophys. Res.*, *108*(D13), 8488, doi:10.1029/2002JD002408.

Gao, S., D. A. Hegg, P. V. Hobbs, T. W. Kirchstetter, B. I. Magi, and M. Sadilek (2003), Water-soluble organic components in aerosols associated with savanna fires in southern Africa: Identification, evolution, and distribution, *J. Geophys. Res.*, *108*(D13), 8491, doi:10.1029/2002JD002324.

Gautier, C., Diak and S. Masse (1980), A simple physical model to estimate incident solar radiation at the surface from GOES satellite data, *J. Appl. Meteor.*, *19*, 1005-1012.

Gautier, C. and Lansfeld M. (1997), Surface Solar Radiation Flux and Cloud Radiative Forcing for the Atmospheric Radiation Measurement (ARM) Southern Great Plains (SPG): A Satellite, Surface Observations, and Radiative Transfer Model Study, *J. Atmos. Sci.,* 54, 1289-1307.

Geogdzhayev, I. V., M. I. Mishchenko, W. B. Rossow, B. Cairns, and A. A. Lacis (2002), Global two-channel AVHRR retrievals of aerosol properties of the ocean for the period of *NOAA-9* observations and preliminary retrievals using *NOAA-7* and *NOAA-11* data. *J. Atmos. Sci., 59*, 262–278.

Ghan, S., R. Easter, E. Chapman, H. Abdul-Razzak, Y. Zhang, L. Leung, N. Laulainen, R. Saylor, and R. Zaveri (2001a), A physically based estimate of readiative forcing by anthropogenic sulfate aerosol, *J. Geophys. Res.*, *106*, 5279-5293.

Ghan, S., N. Laulainen, R. Easter, R. Wagener, S. Nemesure, E. Chapman, Y. Zhang, and R. Leung (2001b), Evaluation of aerosol direct forcing in MIRAGE, , *J. Geophys. Res.*, *106*, 5295-5316.

Ghan, S. J., R. C. Easter, J. Hudson, and F.-M. Breon, (2001c), Evaluation of aerosol indirect radiative forcing in MIRAGE, *J. Geophys. Res.*, 106, 5317-5334.

Ginoux, P., M. Chin, I. Tegen, J. Prospero, B. Holben, O. Dubovik, and S.-J. Lin (2001), Sources and distributions of dust aerosols simulated with the GOCART model, *J. Geophys. Res.*, *106*, 20,225-20,273.

Gong, S. L., L. A. Barrie, J.-P. Blanchet, K. von Salzen, U. Lohmann, G. Lesins, L. Spacek, L. M. Zhang, E. Girard, H. Lin, R. Leaitch, H. Leighton, P. Chylek and P. Huang (2003), CAM: A Size Segregated Simulation of Atmospheric Aerosol Processes for Climate and Air Quality Models 1 .Module Development. *J. Geophys. Res.s, 108*(D1), 4007-4023.

Gordon, H. R., and M. Wang (1994), Retrieval of water-leaving radiance and aerosol optical thickness over the oceans with SeaWiFS: A preliminary algorithm. *Appl. Opt., 33*, 443–452.

Halthore, R. N., S. E. Schwartz, J. J. Michalsky, G. P. Anderson, R. A. Ferrare, B. N. Holben, and H. M. Ten Brink (1997), Comparison of model estimated and measured direct-normal solar irradiance, *J. Geophys. Res., 102*, 29,991– 30,002.

Halthore, R. N., S. Nemesure, S. E. Schwartz, D. G. Imre, A. Berk, E. G. Dutton, and M. H. Bergin (1998), Models overestimate diffuse clear-sky surface irradiance: A case for excess atmospheric absorption, *Geophys. Res. Lett., 25*, 3591–3594.

Halthore, R. N., and S. E. Schwartz (2000), Comparison of model-estimated and measured diffuse downward irradiance at surface in cloud-free skies, *J. Geophys. Res.*, *105*, 20,165–20,177.

Hansen, J. E. (1969), Exact and approximate solutions for multiple scattering by cloudy and hazy planetary atmospheres. *J. Atmos. Sci., 26*, 478–487.

Hansen J. E. and L. D. Travis (1974), Light scattering in planetary atmospheres, *Space Science Reviews*, *16*, 527-610.

Hansen, J. E., M. Sato, and R. Ruedy (1997), Radiative forcing and climate response, *J. Geophys. Res.*, *102*, 6831-6864.

Hauglustaine, D. A., F. Hourdin, L. Jourdain, M.-A. Filiberti, S. Walters, J.-F. Lamarque, and E. A. Holland (2004), Interactive chemistry in the Laboratoire de Météorologie Dynamique general circulation model: Description and background tropospheric chemistry evaluation, *J. Geophys. Res.*, *109*, D04314, doi:10.1029/2003JD003957.

Haywood, J. M., S. R. Osborne, P. N. Francis, A. Keil, P. Formenti, M. O. Andreae, and P. H. Kaye (2003), The mean physical and optical properties of regional haze dominated by biomass burning aerosol measured from the C-130 aircraft during SAFARI 2000, *J. Geophys. Res.*, *108*(D13), 8473, doi:10.1029/2002JD002226.

Heaffelin, M., S. Kato, A. M. Smith, C. K. Rutledge, T. P. Charlock, and J. R. Mahan (2001), Determination of the thermal offset of the Eppley precision spectral pyranometer, *Appl. Opt., 40*, 472–484.

Hegg, D. A., J. Livingston, P. V. Hobbs, T. Novakov, and P. Russell (1997), Chemical apportionment of aerosol column optical depth off the Mid-Atlantic Coast of the United States, *J. Geophys. Res., 102,* 25,293-25,303.

Henyey, L. and J. Greenstein (1941), Diffuse radiation in the galaxy, *Astrophys. Journal*, *93*, 70-83.

Herman, J. R., P. K. Bhartia, O. Torres, C. Hsu, C. Seflor, and E. Celarier (1997), Global distribution of UV-absorbing aerosols from Nimbus 7/TOMS data, *J. Geophys. Res*., *102*, 16,9111-16,922.

Hess, M., P. Köpke, and I. Schult (1998), Optical Properties of Aerosols and Clouds: The Software package OPAC, *Bull. Am. Met. Soc.*, *79*, 831-844.

Highwood, E. J., J. M. Haywood, M. D. Silverstone, S. M. Newman, and J. P. Taylor (2003), Radiative properties and direct effect of Saharan dust measured by the C-130 aircraft during Saharan Dust Experiment (SHADE): 2. Terrestrial spectrum, *J. Geophys. Res.,108*(D18), 8578, doi:10.1029/2002JD002552.

Hignett, P., J. P. Taylor, P. N. Francis, and M. D. Glew (1999), Comparison of observed and modeled direct aerosol forcing during TARFOX, *J. Geophys. Res.*, *104*(D2), 2279–2288.

Higurashi, A., and T. Nakajima (1999), Development of a two channel aerosol retrieval algorithm on global scale using NOAAAVHRR, *J. Atmos. Sci., 56*, 924-941.

Hobbs, P. V., J. S. Reid, R. A. Kotchenruther, R. J. Ferek, and R. Weiss (1997), Direct Radiative Forcing by Smoke from Biomass Burning, *Science, 272,* 1776-1778.

Holben, B. N., T. F. Eck, I. Slutsker, D. Tanré, J. P. Buis, A. Setzer, E. Vermote, J. A. Reagan, Y. J. Kaufman, T. Nakajima, F. Lavenu, I. Jankowiak, and A. Smirnov (1998), AERONET - A federated instrument network and data archive for aerosol characterization, *Rem. Sens. Environ., 66*, 1-16.

Holben, B. N. and coauthors (2001), An emerging ground-based aerosol climatology: Aerosol optical depth from AERONET, J. Geophys. Res., *106* (D11): 12067-12097.

Hoell, C., O'Dowd, C., Osborne, S. and Johnson, D. W. (2000), Timescale analysis of marine boundary layer aerosol evolution: Lagrangian case studies under clean and polluted cloudy conditions. *Tellus, 52B*, 423–438.

Holzer-Popp, T., M. Schroedter, and G., Gesell (2002), Retrieving aerosol optical depth and type in the boundary layer over land and ocean from simultaneous GOME spectrometer and ATSR-2 radiometer measurements, 1, Method description, *J. Geophys. Res*., *107*(D21), 4578, doi:10.1029/2001JD002013.

Horowitz, L. et al. (2003), A global simulation of tropospheric ozone and related tracers: Description and evaluation of MOZART, version 2, *J. Geophys. Res*., *108*(D24), 4784, doi:10.1029/2002JD002853.

Husar, R. B., J. M. Prospero, and L. L. Stowe (1997), Characterization of tropospheric aerosols over the oceans with the NOAA advanced very high-

resolution radiometer optical thickness operational product, *J. Geophys. Res*., *102*, 16,889-16,909.

Ichoku, C., L. A. Remer, Y. J. Kaufman, R. Levy, D. A. Chu, D. Tanré, and B. N. Holben (2003), MODIS observation of aerosols and estimation of aerosol radiative forcing over southern Africa during SAFARI 2000, *J. Geophys. Res.*, *108*(D13), 8499, doi:10.1029/2002JD002366.

Ignatov, A. and L. Stowe (2000), Physical basis, premises, and self-consistency checks of aerosol retrievals from TRMM/VIRS. *J. Appl. Meteorol.*, *39*, *12*, 2259-2277.

Ignatov, A.and N. Nalli (2002), Aerosol retrievals from multiyear multisatellite AVHRR Pathfinder atmosphere (PATMOS) dataset for correcting remotely sensed sea surface temperatures. *J. Atmos. Oceanic Technol., 12*, 1986–2008.

Intergovernmental Panel on Climate Change (IPCC) (2001), *Climate Change 2001: The Scientific Basis. Contribution of Working Group I to the Third Assessment Report of the Intergovernmental Panel on Climate Change*, edited by J. T. Houghton et al., 881 pp., Cambridge Univ. Press, New York.

Jacob, D. J., J. H. Crawford, M. M. Kleb, V. S. Connors, R. J. Bendura, J. L. Raper, G. W. Sachse, J. C. Gille, L. Emmons, and C. L. Heald (2003), Transport and Chemical Evolution over the Pacific (TRACE-P) aircraft mission: Design, execution, and first results, *J. Geophys. Res., 108*(D20), 9000, doi:10.1029/2002JD003276.

Jacobowitz, H., H.V. Soule, H.L. Kyle, F.B. House, and the NIMBUS 7 ERB Experiment Team (1984), The Earth Radiation Budget (ERB) Experiment: An overview, *J. Geophy. Res*., *89*, 5021-5038.

Jeong, M.-J., Z. Li, D. A. Chu, and S.-C. Tsay (2005), Quality and compatibility analyses of global aerosol products derived from the advanced very high resolution radiometer and Moderate Resolution Imaging Spectroradiometer, *J. Geophys. Res., 110*, D10S09, doi:10.1029/2004JD004648.

Jin, Y., C. B. Schaaf, C. E. Woodcock, F. Gao, X. Li, A. H. Strahler, W. Lucht, and S. Liang (2003), Consistency of MODIS surface bidirectional reflectance distribution function and albedo retrievals: 2. Validation, *J. Geophys. Res.*, *108*(D5), 4159, doi:10.1029/2002JD002804.

Joaquim, B., A. J. Busalacchi and R. Murtugudde (2001), Application of a reduced-order Kalman Filter to initialize a coupled atmosphere-ocean model: impact on the prediction of El Nino, *J. Climate, 14*, 1720-1737.

Johnson, D. W., Osborne, S., Wood, R., Suhre, K., John-son, R., Businger, S., Quinn, P. K., Wiedensohler, A., Durkee, P. A., Russell, L. M., Andreae, M. O., O'Dowd, C., Noone, K. J., Bandy, B., Rudolph, J. and Rapsomanikis, S. (2000), An overview of the Lagrangian experiments undertaken during the North Atlantic regional aerosol characterisation experiment (ACE-2). *Tellus 52B*, 290–320.

Junge, C. E. (1955), The size distribution and aging of natural aerosols as determined from electrical and optical measurements in the atmosphere, *J. Meteorol., 12*, 13-25.

Kahn, R. A., B. J. Gaitley, J. V. Martonchik, D. J. Diner, K. A. Crean, and B. Holben (2005), Multiangle Imaging Spectroradiometer (MISR) global aerosol optical depth validation based on 2 years of coincident Aerosol Robotic Network

(AERONET) observations, *J. Geophys. Res*., *110*, D10S04, doi:10.1029/2004JD004706.
Kalnay, E., and Coauthors, 1996: The NCEP/NCAR 40-Year Reanalysis Project. *Bull. Amer. Meteor. Soc.,* 77, 437–471.
Kalplan, A., Y. Kushnir, M. A. Cane, and M. B. Blumenthal (1997), Reduced space optimal analysis for historical data sets:136 years of Atlantic Sea surface temperatures, *J. Geophys. Res., 102,* 27,835-27,860.
Kanamitsu, M., W. Ebisuzaki, J. Woollen, S-K Yang, J.J. Hnilo, M. Fiorino, and G. L. Potter (2002), NCEP-DEO AMIP-II Reanalysis (R-2), *Bull. Amer. Meteor. Soc*., *83*, 1631-1643.
Kato, S., T. P. Ackerman, E. E. Clothiaux, J. H. Mather, G. G. Mace, M. L. Wesley, F. Murcray, and J. Michalsky (1997), Uncertainties in modeled and measured clear sky surface shortwave irradiances, *J. Geophys. Res., 102*, 25,881– 25,898.
Kaufman, Y. J., A. Setzer, D. Ward, D. Tanré, B. N. Holben, P. Menzel, M. C. Pereira, and R. Rasmussen (1992), Biomass Burning Airborne and Spaceborne Experiment in the Amazonas (BASE-A), *J. Geophys. Res, 97,* 14581-14599.
Kaufman, Y. J., D. Tanré, L. Remer, E. F. Vermote, A. Chu, and B. N. Holben (1997), Operational remote sensing of tropospheric aerosol over the land from EOS-MODIS, *J. Geophys. Res.*, *102,* 17,051-17,068.
Kaufman, Y. J., Y., D. Tanré, O. Dubovik, A. Karnieli. and L.A. Remer (2001), Absorption of sunlight by dust as inferred from satellite and ground-based remote sensing, *Geophys. Res. Lett., 28*, 1479– 1483.
Kaufman, Y. J., D. Tanré, and O. Boucher (2002a), A satellite view of aerosols in the climate system, *Nature, 419*, 10.1038/natue01091.
Kaufman, Y. J., J. V. Martins, L. A. Remer, M. R. Schoeberl, and M. A.Yamasoe (2002b), Satellite retrieval of aerosol absorption over the oceans using sunglint, *Geophys. Res. Lett., 29*, 1928, doi:10.1029/2002GL015403.
Kaufman Y. J., O. Boucher, D. Tanré, M. Chin, L. A. Remer, T. Takemura (2005), Aerosol anthropogenic component estimated from satellite data, *Geophys. Res. Lett., 32*, L17804, doi:10.1029/2005GL023125.
Keil, A., and J. M. Haywood (2003), Solar radiative forcing by biomass burning aerosol particles during SAFARI 2000: A case study based on measured aerosol and cloud properties, *J. Geophys. Res.*, *108*(D13), 8467, doi:10.1029/2002JD002315.
Kiehl, J. T., and B. P. Briegleb (1993), The relative roles of sulfate aerosols and greenhouse gases in climate forcing, *Science, 260*, 311-314.
Kiehl, J. T., and K. E. Trenberth (1997), Earth's annual global mean energy budget, *Bull. Amer. Meteor. Soc.*, *78*, 197-208.
Kim, D.-H., B.-J. Sohn, T. Nakajima, T. Takamura, T. Takemura, B.-C. Choi, and S.-C. Yoon (2004), Aerosol optical properties over east Asia determined from ground-based sky radiation measurements, *J. Geophys. Res., 109*, D02209, doi:10.1029/2003JD003387.
King, M. D., Y. J. Kaufman, D. Tanré, and T. Nakajima (1999), Remote sensing of tropospheric aerosols from space: Past, present and future, *Bull. Am. Meterol. Soc.*, *80(11),* 2,229-2,259.

Kinne, S., B. N. Holben, T. F. Eck, A. Smirnov, O. Dubovik, I. Slutsker, D. Tanre, G. Zibozdi, U. Lohmann, S. Ghan, R. Easter, M. Chin, P. Ginoux, T. Takemura, I. Tegen, D. Koch, R. Kahn, E. Vermote, L. Stowe, O. Torres, M. Mishchenko, I. Geogdzhayev, and A. Hiragushi (2001), How well do aerosol retrievals from satellites and representation in global circulation models match ground-based AERONET aerosol statistics? In *Remote Sensing and Climate Modeling: Synergies and Limitations* (M. Beniston and M. M. Verstraete, Eds.), Advances in Global Change Research, Vol. 7, 103-158. Kluwer Academic. Dordrecht, Netherlands.

Kinne, S. and coauthors (2003), Monthly averages of aerosol properties: A global comparison among models, satellite data, and AERONET ground data, *J. Geophys. Res.*, *108(D20),* 4634, doi:10.1029/2001JD001253.

Kinne, S., and coauthers (2005), An AeroCom initial assessment – optical properties in aerosol component modules of global models, *Atmos. Chem. Phys*., *5*, 8285–8330.

Klink, J. C., and K. J. Dollhopf (1986), An evaluation of satellite-based insolation estimates for Ohio, *J. Climate Appl. Meteor.*, *24*, 1741-1751.

Knapp, K. R., T. H. Vonder Haar, and Y. J. Kaufman (2002), Aerosol optical depth retrieval from GOES-8: Uncertainty study and retrieval validation over South America. *J. Geophys. Res.*, *107*(D7), 4055, doi:10.1029/2001JD000505.

Kneizys, F.X., L.W. Abreu, G. P. Anderson, J. H. Chetwynd, E. P. Shettle, A. Berk, L. S. Bernstein, D. C. Robertson, P. Acharya, L. S. Rothman, J. E. A. Selby, W. O. Gallery, and S. A. Clough (1996), The MODTRAN 2/3 Report and LOWTRAN 7 Model, Phillips Laboratory, Geophysics Directorate, PL/GPOS, Hanscom AFB, MA 01731-3010.

Koch, D., D. Jacob, I. Tegen, D. Rind, and M. Chin (1999), Tropospheric sulfur simulation and sulfate direct forcing in the Goddard Institute for Space Studies (GISS) general circulation model, *J. Geophys. Res.*, *104,* 23,799-23,822.

Koch, D. (2001), The transport and direct radiative forcing of carbonaceous and sulfate aerosol in the GISS GCM, *J. Geophys. Res.*, *106,* 20,311-20,332.

Koch, D., G. Schmidt, and C. Field (2005), Sulfur, sea salt and radionuclide aerosols in GISS ModelE. *J. Geophys. Res.,* submitted.

Köepke, P., M. Hess, I. Schult, and E. P. Shettle (1997), Global aerosol data set. MPI Meteorologie Hamburg Rep. 243, 44 pp.

Kotchenruther, R. A., P. V. Hobbs, and D. A. Hegg (1999), Humidification factors for atmospheric aerosol off the mid-Atlantic coast of United States. *J. Geophys. Res., 104*, 2239–2251.

Kotchenruther, R. A. and P. V Hobbs (1998), Humidification factors of aerosols from biomass burning in Brazil. *J. Geophys. Res., 103*(D24), 32,081-32,089.

Krol, M., S. Houweling, B. Bregman, M. van den Broek, A. Segers, P. van Velthoven, W. Peters, F. Dentener and P. Bergamaschi (2004), The two-way nested global chemistry-transport zoom model TM5: algorithm and applications, *Atmos. Chem. Phys*., *4*, 3975-4018.

Laszlo, I., H. Jacobowitz, and A. Gruber (1988), The relative merits of narrowband channels for estimating broadband albedos. *J. Atmos. Ocean. Technol*., *5*, 757-773.

Laszlo I. and R. T. Pinker (1994), Of the relationship between shortwave net radiative fluxes at the top of the atmosphere and at the surface, Eighth Conference on Atmospheric Radiation, Nashville, TN, January 23-28, 1994, *Amer. Meteor. Soc*., 532-533.

Lauer, A., J. Hendricks, I. Ackermann, B. Schell, H. Hass, and S. Metzger (2005), Simulating aerosol microphysics with the ECHAM/MADE GCM – Part I: Model description and comparison with observations*, Atmos. Chem. Phys., 5,* 7965–8026.

Lavanchy, M. G., Schotterer, U., Schwikowski, M., Gaggeler, H. W., and Baltensperger, U. (1999), Historical record of carbonaceous particle concentrations from a european high-alpine glacier. *J. Geophys. Res*, *104*, 21227–21236.

Léon, J.-F., D. Tanré, J. Pelon, Y. J. Kaufman, J. M. Haywood, and B. Chatenet (2003), Profiling of a Saharan dust outbreak based on a synergy between active and passive remote sensing, J. Geophys. Res., 108(D18), 8575, doi:10.1029/2002JD002774.

Levy, R. C., L. A. Remer, D. Tanre´, Y. J. Kaufman, C. Ichoku, B. N. Holben, J. M. Livingston, P. B. Russell, and H. Maring (2003), Evaluation of the Moderate-Resolution Imaging Spectroradiometer (MODIS) retrievals of dust aerosol over the ocean during PRIDE, *J. Geophys. Res., 108*(D19), 8594, doi:10.1029/2002JD002460.

Levy, R. C., L. A. Remer, J. V. Martins, Y. J. Kaufman, A. Plana-Fattori, J. Redemann, P. B. Russell, and B. Wenny (2005), Evaluation of the MODIS aerosol retrievals over ocean and land during CLAMS. *J. Atmos. Sci.*, *62*, 974-992.

Li, Z. and H.G. Leighton (1993a), Estimation of SW flux absorbed at the surface from TOA reflected flux*, J. Climate. 6,* 317-330.

Li, Z. and H. G. Leighton (1993b), Global Climatologies of Solar Radiation Budgets at the Surface and in the Atmosphere from 5 Years of ERBE Data, *Journal of Geophys. Res., 98*, 4919-4930.

Li, Z. (1995a), Intercomparison between two satellite-based products of net surface shortwave radiation, *J. Geophy. Res.*, *100*, 3221-3232.

Li, Z., H. W. Barker, and L. Moreau (1995b), The variable effect of clouds on atmospheric absorption of solar radiation, *Nature, 376*, 486– 490.

Li, Z., W. Wiscombe, G.L. Stephens, T. P. Ackerman (2004), Disagreements over cloud absorption, *Science, 305*, 1240.

Li, Z., M. C. Cribb, F-L. Chang, A. Trishchenko, and Y. Luo (2005), Natural variability and sampling errors in solar radiation measurements for model validation over the Atmospheric Radiation Measurement Southern Great Plains region, *J. Geophys. Res., 110*, D15S19, doi:10.1029/2004JD005028.

Liu, H., R. T. Pinker, and B. N. Holben (2005), A global view of aerosols from merged transport models, satellite, and ground observations, *J. Geophys. Res., 110*, D10S15, doi:10.1029/2004JD004695.

Lohmann, U., J. Feichter, C. Chuang, and J. Penner (1999), Predicting the number of cloud droplets in the ECHAM GCM, *J. Geophys. Res.*, *104*, 24,557-24,563.

Lucht, W., C. B. Schaaf, and A. H. Strahler (2000), An Algorithm for the retrieval of albedo from space using semiempirical BRDF models, *IEEE Trans. Geosci. Remote Sens.*, *38*, 977-998.

Lyapustin, A.W., D. L., Markham, B., Irons, J., Holben, B. and Wang, Y (2004), A Method for Unbiased High-Resolution Aerosol Retrieval from Landsat, *J. Atmos. Sci*., *61*(11), 1233-1244.

Magi, B. I., P. V. Hobbs, T. W. Kirchstetter, T. Novakov, D. A. Hegg, S. Gao, J. Redemann, and B. Schmid (2005), Aerosol properties and chemical apportionment of aerosol optical depth at locations off the United States east coast in July and August 2001. *J. Atmos. Sci*., *62*, 919-933.

Maring, H., D. L. Savoie, M. A. Izaguirre, L. Custals, and J. S. Reid (2003a), Mineral dust aerosol size distribution change during atmospheric transport, *J. Geophys. Res., 108*(D19), 8592, doi:10.1029/2002JD002536.

Maring, H., D. L. Savioe, M. A. Izaguirre, L. Custals, and J. S. Reid (2003b), Vertical distributions of dust and sea-salt aerosols over Puerto Rico during PRIDE measured from a light aircraft, *J. Geophys. Res., 108*(D19), 8587, doi:10.1029/2002JD002544.

Markowicz, K. M., P. J. Flatau, P. K. Quinn, C. M. Carrico, M. K. Flatau, A. M. Vogelmann, D. Bates, M. Liu, and M. J. Rood (2003a), Influence of relative humidity on aerosol radiative forcing: An ACE-Asia experiment perspective, *J. Geophys. Res., 108*(D23), 8662, doi:10.1029/2002JD003066.

Markowicz, K. M., P. J. Flatau, A. M. Vogelmann, P. K. Quinn, and E. J. Welton (2003b), Clear-sky infrared aerosol radiative forcing at the surface and the top of the atmosphere, *Q. J. R. Meteorol. Soc*., *129*(594), 2927-2947, doi:10.1256/003590003769682110.

Martins, J. V., P. V. Hobbs, R. E. Weiss and P. Artaxo (1998), Sphericity and morphology of smoke particles from biomass burning in Brazil. *J. Geophys. Res., 103*(D24), 32,051-32,057.

Martonchik, J.V., D.J. Diner, R. Kahn, M.M. Verstraete, B. Pinty, H.R. Gordon, and T.P. Ackerman (1998), Techniques for the Retrieval of aerosol properties over land ocean using multiangle data, *IEEE Trans. Geosci. Remt. Sens. 36*, 1212-1227.

Martonchik, J. V., D. J. Diner, K. A. Crean, and M. A. Bull (2002), Regional aerosol retrieval results from MISR, *IEEE Trans. Geosci. Remt. Sens., 40*(7), 1520-1531.

Matthews, E., and W.B. Rossow (1987), Global, seasonal maps of surface visible reflectivity from satellite observations. *J. Clim. Appl. Meteor., 26*, 170-202.

Matthis, I., A. Ansmann, D. Müller, U. Wandinger, and D. Althausen (2004), Multiyear aerosol observations with dual wavelength Raman lidar in the framework of EARLINET, *J. Geophys. Res.*, *109, D13203,*doi:10.1029/2004JD004600.

McFarquhar, G.M., and A.J. Heymsfield (2001), Parameterizations of INDOEX microphysical measurements and calculations of cloud susceptibility: applications for climate studies. *J. Geophys. Res., 106*(D22), 28675-28698.

Meador, W. E., and W. R. Weaver (1980), Two-stream approximations to radiative transfer in planetary atmospheres: A unified description of existing methods and a new improvement. *J. Atmos. Sci., 37*, 630–643.

Michalsky, J., E. Dutton, M. Rubes, D. Nelson, T. Stoffel, M. Wesely, M. Splitt, and J. DeLuisi (1999), Optimal measurement of Surface Shortwave Irradiance Using Current Instrumentation. *J. Atmos. Oceanic. Technol, 16*, 55-69.

Mie, G. (1908), Betirage zur optik Truber Medien, spexiell Killoidaler Metalasungen. Ann.Physik, 25, 377-445.

Minshchenko, M. I., I. V. Geogdzhayev, B. Cairns, W. B. Rossow, and A. A. Lacis (1999), Aerosol retrievals over the ocean by use of channel 1 and 2 AVHRR data: Sensitivity analysis and preliminary results, *Appl. Opt., 38(36),* 7325-7341.

Mishchenko M. I., J. W. Hovenier, and L. D. Travis (2000), *Ligh Scattering by Nonspherical Particles: Theory, Measurements and Applications,* Acad. Press, San Diego, 690pp.

Moore, K., II, et al. (2004), A comparison of similar aerosol measurements made on the NASA P3-B, DC-8, and NSF C-130 aircraft during TRACE-P and ACE-Asia, *J. Geophys. Res., 109*, doi:10.1029/2003JD003543.

Moser, W., and E. Raschke (1984), Incident solar radiation over Europe estimated from Meteosat data, *J. Climate Appl. Meteor.*, *23*, 166-170.

Myhre, G., T.K. Berntsen, J.M. Haywood, J.K. Sundet, B.N. Holben, M. Johnsrud, and F. Stordal (2003a), Modelling the solar radiative impact of aerosols from biomass burning during the Southern African Regional Science Initiative (SAFARI-2000) experiment, *J. Geophys. Res.,108*, 8501, doi:10.1029/2002JD002313.

Myhre, G., A. Grini, J. M. Haywood, F. Stordal, B. Chatenet, D. Tanré, J. K. Sundet, and I. S. A. Isaksen (2003b), Modelling the radiative impact of mineral dust during the SHADE campaign, *J. Geophys. Res*. 108(D18), 8579, doi:10.1029/2002JD002566.

Nakajima, T., M. Tanaka, and T. Yamauchi (1983), Retrieval of the optical properties of aerosols from aureole and extinction data, *Appl. Opt., 22*, 2951-2959.

Nakajima, T., G. Tonna, R. Rao, P. Boi, Y. Kaufman, and B. Holben (1996), Use of sky brightness measurements from ground for remote sensing of particulate polydispersions, *Appl. Opt., 35,* 2672-2686.

Nakajima, T. Y., T. Nakajima, M. Nakajima, H. Fukushima, M. Kuji, A. Uchiyama, and M. Kishino (1998), Optimization of the Advanced Earth Observing Satellite II global imager channels by use of radiative transfer calculations, *Appl. Opt.*, *37*, 3149–3163.

Nakajima T., A. Higurashi, K. Aoki, T. Endoh, H. Fukushima, M. Toratani, Y. Mitomi, B. G. Mitchell, and R. Frouin (1999), Early phase emphasis of OCTS radiance data for aerosol remotesensing, *IEEE Trans. Geosci. Remote Sens*. *37*, 1575–1585.

Nakajima, T. et al. (2003), Significance of direct and indirect radiative forcings of aerosols in the East China Sea region, *J. Geophys. Res.*, *108*(D23), 8658, doi:10.1029/2002JD003261.

Ohmura, A., and Coauthors (1998), Baseline surface radiation network (BSRN/WCRP): New precision radiometry for climate research. *Bull. Amer. Meteor. Soc., 79,* 2115–2136.

O'Neill, N. T., T. F. Eck, B. N. Holben, A. Smirnov and O. Dubovik (2001), Bimodal size distribution influences on the variation of Angstrom derivatives in spectral and optical depth space, *J. Geophys. Res*., *106*, 9787-9806.
Oort, A. H., and E. M. Rasmusson (1971), Atmospheric Circulation Statistics, *NOAA Prof. Paper No. 5,* 323 PP.
Pandithurai, G., R. T. Pinker, T. Takamura, and P. C. S. Devara (2004), Aerosol radiative forcing over a tropical urban site in India, *Geophys. Res. Lett.*, *31*, L12107, doi:10.1029/2004GL019702.
Patterson, E. M., D. A. Gillette, and B. Stockton (1977), Complex index of refraction between 300 and 700 nm for Saharan aerosols, *J. Geophys. Res., 82*, 3153–3160.
Penner, J.E., R. E. Dickinson, C.A. O'Neill (1992), Effects of aerosol from biomass burning on the global radiation budget, *Science,* 256, 1432-1434.
Penner, J. E., S. Y. Zhang, M. Chin, C. C. Chuang, J. Feichter, Y. Feng, I. V. Geogdzhayev, P. Ginoux, M. Herzog, A. Higurashi, D. Koch, C. Land, U. Lohmann, M. Mishchenko, T. Nakajima, G. Pitari, B. Soden, I. Tegen, and L. Stowe (2002), A comparison of model- and satellite-derived aerosol optical depth and reflectivity, *J. Atmos. Sci*., *59*, 441-460.
Philipona, R. (2002), Underestimation of solar global and diffuse radiation measured at Earth's surface, *J. Geophys. Res., 107*(D22), 4654, doi:10.1029/2002JD002396.
Pierluissi J. H. and C. E. Maragoudakis (1986), Molecular transmission band models for LOWTRAN, AFGL-TR-86-0272, AD A180655.
Pilewskie, P., and F. P. Valero (1995), Direct observations of excess solar absorption by clouds, *Science, 267*, 1626– 1629.
Pinker, R. T. and L. A. Corio (1984), Surface Radiation Budget from satellites, *Monthly Weather Review, 112,* 209-215.
Pinker, R. T., J. A. Ewing and J. D. Tarpley (1985), The Relationship between the Planetary and Surface Net Radiation, *J. Clim. and Appl. Meteorol., 24*, 1262-1267.
Pinker, R. T. and I. Laszlo (1992), Modeling surface solar irradiance for satellite applications on global scale, *J. Appl. Meteor., 31*, 194-211.
Pinker, R. T, R. Frouin, and Z. Li (1995), A review of satellite methods to derive surface shortwave radiative fluxes, *Remote Sens. Environ., 51*, 108-124.
Pitari, G., E. Mancini, A. Bregman, H. L. Rogers, J. K. Sundet, V. Grewe, and O. Dessens, (2001), Sulphate particles from subsonic aviation: Impact on upper tropospheric and lower stratospheric ozone, *Phys. Chem. of Earth*, 26/8, 563-569.
Pitari, G., E. Mancini, V. Rizi, and D. T. Shindell (2002), Impact of future climate and emission changes on stratospheric aerosols and ozone, *J. Atmos. Sci.*, *59*, 414– 440.
Putaud, J.-P., R. Van Dingenen, M. Mangoni, A. Virkkula, F. Raes, H. Maring, J. M. Prospero, E. Swietlicki, O. Berg, R. Hillamo and T. Makela (2000), Chemical mass closure and assessment of the origin of the submicron aerosol in the marine boundary layer and the free troposphere at Tenerife during ACE-2. *Tellus 52B*, 141–168.
Quinn, P. K.; D. J. Coffman, V. N. Kapustin, T. S. Bates and D. S. Covert (1998), Aerosol optical properties in the marine boundary layer during the First Aerosol

Characterization Experiment (ACE 1) and the underlying chemical and physical aerosol properties, *J. Geophys. Res., 103*(D13), 16,547-16563.
Quinn, P. K.and D. J. Coffman, D. J. (1998), Local closure during the First Aerosol Characterization Experiment (ACE 1): Aerosol mass concentration and scattering and backscattering coefficients, *J. Geophys. Res., 103*(D13), 16,575-16,596.
Quinn, P. K., T. S. Bates, D. J. Coffman, T. L. Miller, J. E. Johnson and D. S. Covert (2000), A comparison of aerosol chemical and optical properties from the first and second aerosol characterization experiments. *Tellus 52B*, 239–257.
Quinn, P.K., D.J. Coffman, T.S. Bates, T.L. Miller, J.E. Johnson, K. Voss, E.J. Welton, and C. Neusüb (2001), Dominant aerosol chemical components and their contribution to extinction during the Aerosols99 cruise across the Atlantic, *J. Geophys. Res.*, *106*(D18), 20,783-20,810.
Ramanatha, V. (1986), Scientific use of surface radiation budget data for climate studies, *Surface Radiation Budget for Climate Studies*: J. T. Suttles and G. Ohring, Eds., NASA Ref. Publ. 1169, 132pp.
Ramanathan, V., B. Subasilar, G. J. Zhang, W. Conant, R. D. Cess, J. T. Kiehl, H. Grassl, and L. Shi (1995), Warm pool heat budget and shortwave cloud forcing: A missing physics?, *Science, 267*, 499– 503.
Ramanathan, V., P. J. Crutzen, J. T. Kiehl, and D. Rosenfeld (2001a), Aerosols, climate, and the hydrological cycle, *Science, 294*, 2119-2124.
Ramanathan, V., Crutzen, P. J., Lelieveld, J., Althausen, D., Anderson, J., Andreae, M. O., Cantrell, W., Cass, G. and Chung, C. E. (2001b), The Indian Ocean Experiment: an integrated assessment of the climate forcing and effects of the great Indo-Asian haze, *J. Geophys. Res. 106*, 28,371-28,398.
Ramon D. and R. Santer (2001), Operational Remote Sensing of Aerosols over Land to Account for Directional Effects, *Applied Optics-LP*, 40, 3060-3075.
Rao. C. R. N., E. P. McClain, and L. L. Stowe (1989), Remote-sensing of aerosols over the oceans using AVHRR data theory, practice and applications, *Int. J. Remote Sens*., *10,* 743-749.
Redemann, J., R. P. Turco, K. N. Liou, P. V. Hobbs, W. S. Hartley, R. W. Bergstrom, E. V. Browell, and P. B. Russell (2000), Case studies of the vertical structure of the direct shortwave aerosol radiative forcing during TARFOX. *J. Geophys. Res. 105*, 9971-9979.
Redemann, J., S. J. Masonis, B. Schmid, T. L. Anderson, P. B. Russell, J. M. Livingston, O. Dubovik, and A. D. Clarke (2003), Clear-column closure studies of aerosols and water vapor aboard the NCAR C-130 during ACE-Asia, 2001, *J. Geophys. Res., 108*(D23), 8655, doi:10.1029/2003JD003442.
Reid, J. S. and P. V. Hobbs (1998), Physical and optical properties of young smoke from individual biomass fires in Brazil.*J. Geophys. Res., 103*(D24), 32,013-32,030.
Reid, J. S., P. V. Hobbs, R. J. Ferek, D. R. Blake, J. V. Martins, M. R. Dunlap and C. Liousse (1998a), Physical, chemical, and optical properties of regional hazes dominated by smoke in Brazil. *J. Geophys. Res., 103*(D24), 32,059-32,080.
Reid, J. S., P. V. Hobbs, C. Liousse, J. V. Martins, R. E. Weiss and T. F. Eck (1998b) Comparisons of techniques for measuring shortwave absorption and black carbon

content of aerosols from biomass burning in Brazil, *J. Geophys. Res., 103*(D24), 32,031-32,040.
Reid, J. S., et al. (2003a), Comparison of size and morphological measurements of coarse mode dust particles from Africa, *J. Geophys. Res., 108*(D19), 8593, doi:10.1029/2002JD002485.
Reid, J. S., et al. (2003b), Analysis of measurements of Saharan dust by airborne and ground-based remote sensing methods during the Puerto Rico Dust Experiment (PRIDE), *J. Geophys. Res., 108*(D19), 8586, doi:10.1029/2002JD002493.
Remer, L. A., S. Gasso, D. A. Hegg, Y. J. Kaufman, and B. N. Holben (1997), Urban/industrial aerosol: Ground-based sun/sky radiometer and airborne in situ measurements. *J. Geophys. Res., 102*, 16849–16859.
Remer, L. A., and Y. J. Kaufman (1998), Dynamic aerosol model: Urban/industrial aerosol. *J. Geophys. Res., 103*, 13,859–13,871.
Remer, L. A., Y. J. Kaufman, B. N. Holben, A. M. Thompson and D. McNamara (1998), Biomass burning aerosol size distribution and modeled optical properties. *J. Geophys. Res., 103*(D24), 31,879-31,891.
Remer, L. A., Y. J. Kaufman and B. N. Holben (1999), Interannual variation of ambient aerosol characteristics on the east coast of the United States. *J. Geophys. Res., 104*(D2), 2223–2231.
Remer, L. A., Y. J. Kaufman, D. Tanré, S. Mattoo, D. A. Chu, J. V. Martins, R.-R. Li, C. Ichoku, R. C. Levy, R. G. Kleidman, T. F. Eck, E. Vermote, and B. N. Holben (2005), The MODIS aerosol algorithm, products and validation. *J. Atmos. Sci., 62(4)*, 947-973.
Reynolds, R. W. (1988), A real-time global sea surface temperature analysis, *J. Climate, 1*, 75-86.
Ricchiazzi P., S. Yang, C. Gautier, and D. Sowle (1998), SBDART: A research and teaching software tool for plane-parallel radiative transfer in the earth's atmosphere. *Bull. of Amer. Meteor. Soc.*, 79(10), 2101-2114.
Roeckner, E. and coauthors (1996), The atmospheric general circulation model ECHAM-4: Model description and simulation of present-day climate, *Tech. Rep. 218*, Max-Planck-Inst. Fur Meteorol., Hamburg, Germany.
Ross, J. L., P. V. Hobbs and B. N. Holben (1998), Radiative characteristics of regional hazes dominated by smoke from biomass burning in Brazil: Closure tests and direct radiative forcing. *J. Geophys. Res., 103*(D24), 31,925-31,941.
Rossow, W. B., E. Kinsella, A. Wolf, and L. Garder (1987), International Satellite Cloud Climatology Project (ISCCP) Description of Reduced Resolution Radiance Data. In, *WMO/TD No. 58*. (eds.), World Meteorological Organization, Geneva, 143 pp.
Rossow, W. B., and R. A. Schiffer (1991), ISCCP Cloud Data Products. *Bull. Amer. Meteor. Soc.*, *72*, 2-20.
Rossow, W.B., and L.C. Garder (1993), Cloud detection using satellite measurements of infrared and visible radiances for ISCCP. *J. Climate, 6*, 2370-2393.
Rossow, W. B., A. W. Walker, D. E. Beuschel, and M. D. Roiter (1996), International Satellite Cloud Climatology Project (ISCCP) Documentation of New Cloud Datasets. WMO/TD-No. 737, World Meteorological Organization, 115 pp.

Russell, P. B., S. Kinne, and R. Bergstrom (1997), Aerosol climate effects: Local radiative forcing and column closure experiments, *J. Geophys. Res. 102*, 9397-9407.

Russell, P. B., J. M. Livingston, P. Hignett, S. Kinne, J. Wong, A. Chien, R. Bergstrom, P. Durkee, and P. V. Hobbs (1999), Aerosol-induced radiative flux changes off the United States Mid-Atlantic coast: Comparison of values calculated from sunphotometer and in situ data with those measured by airborne pyranometer, *J. Geophys. Res*., *104*(D2), 2289-2307.

Satheesh, S.K. and Ramanathan, V. (2000), Large differences in tropical aerosol forcing at the top of the atmosphere and Earth's surface, *Nature, 405*, 60-63.

Satheesh S. K. and J. Srinivasan (2005), A method to infer short wave absorption due to aerosols using satellite remote sensing, *Geophys. Res. Lett., 32*, L13814, doi:10.1029/2005GL023064.

Schaaf, C. B., F. Gao, A. H. Strahler, W. Lucht, X. Li, T. Tsang, N. C. Strugnell, X. Zhang, Y. Jin, J.-P. Muller, P. Lewis, M. Barnsley, P. Hobson, M. Disney, G. Roberts, M. Dunderdale, C. Doll, R. d'Entremont, B. Hu, S. Liang, and J. L. Privette (2002), First Operational BRDF, Albedo and Nadir Reflectance Products from MODIS, *Remote Sens. Environ., 83*, 135-148.

Schiffer, R.A., and Rossow, W.B. (1983), The International Satellite Cloud Climatology Project (ISCCP): The first project of the World Climate Research Programme, *Bull. Amer. Meteor. Soc., 64*, 779-984.

Schiffer, R.A., and Rossow, W.B. (1985), ISCCP global radiance data set: A new resource for climate research. *Bull. Amer. Meteor. Soc., 66*, 1498-1505.

Schmetz, J. (1993), Relationship between Solar Net Radiative Fluxes at the Top of the Atmosphere and at the Surface, *Journal of Atmos. Sci., 50*, 1122-1132.

Schwartz, S. E. (1996), The Whitehouse effect-Short-wave radiative forcing of climate by anthropogenic aerosols: An overview*, J. Aerosol Sci., 27*, 359-382.

Shettle, E. P. and R. W. Fenn (1979), Models of aerosols of lowertroposphere and the effect of humidity variations on their optical properties. AFCRL Tech. Rep. 79 0214, Air Force Cambridge Research Laboratory, Hanscom Air Force Base, MA, 100 pp.

Shuttles, J. T., R. N. Green, P. Minnis, G. L. Smith, W. F. Staylor, B. A. Wielicki, I. J. Walker, d. f. Young, V. R. Taylor and L. L. Stowe (1988), Angular radiation models for Earth Atmosphere system. NASA reference publication 1184, 143pp.

Smith, T. M., R. W. Reynolds, R. E. Livezey, and D. C. Stokes (1996), Reconstruction of historical sea surface temperatures using Empirical Othogonal Functions, *J. Climate, 9,* 1403-1420.

Sokolik, I. N. and O. B. Toon (1999), Incorporation of mineralogical composition into models of the radiative properties of mineral aerosol from UV to IR wavelengths. *J. Geophys. Res.*, *104*, 9423-9444.

Stamnes K., S. C. Tsay, W. Wiscombe, and K. Jayaweera (1998), A Numerically Stable Algorithm for Discrete-Ordinate-Method Radiative Transfer in Multiple Scattering and Emitting Layered Media. *Applied Optics*, *27*, 2502-2509.

Stephens, G. L. (1996), How much solar radiation do clouds absorb? *Science, 271*,1131–1133.

Stier, P., J. Feichter, S. Kinne, S. Kloster, E. Vignati, J. Wilson, Y. Balkanski, M. Schulz, L. Ganzeveld, M. Werner, I.Tegen, O. Boucher, A. Minikin, A. Petzold (2005), The aerosol-climate model ECHAM5-HAM, *Atmos. Chem. Phys*., *5*, 1125-1156.

Stowe, L. L., A. M. Ignatov, and R. R. Singh (1997), Development, validation and potential enhancement to the second generation operational aerosol product at the National Environmental Satellite, Data and Information Service of the National Oceanic and Atmospheric Administration, *J. Geophy. Res.*, *102,* 16,923-16,934.

Stowe L. L., H. Jacobowitz, G. Ohring, K. Knapp, and N. Nalli (2002), The AVHRR Pathfinder Atmosphere (PATMOS) climate dataset: Initial analyses and evaluation. *J. Climate, 15*, 1243–1260.

Stuhlmann, R., Rieland, M., Raschke, E (1990), An improvement of the IGMK model to derive total and diffuse solar radiation at the surface from satellite data, *J. Appli. Meteor.* vol.29:586-603.

Suttles, J. T., and G. Ohring (1986), Surface Radiation Budget for Climate Applications, NASA Ref. Publ. 1169, 132pp.

Tahnk, W. R., and J. A. Coakley Jr. (2002), Aerosol optical depth and direct radiative forcing for INDOEX derived from AVHRR Observations, January–March 1996–2000, *J. Geophys. Res.*, *107*(D19), 8010, doi:10.1029/2000JD000183.

Takemura, T., H. Okamoto, Y. Maruyama, A. Numaguti, A. Hiragushi, and T. Nakajima (2000), Global three dimensional simulation of aerosol optical thickness distribution of various origins, *J. Geophy. Res.*, *105,* 17,853-17,873.

Takemura, T., T. Nakajima, O. Dubovik, B. N. Holben, and S. Kinne (2002), Single scattering albedo and radiative forcing of various aerosol species with a global three-dimensional model, *Journal of Climate*, 15, 333-352.

Takemura, T., T. Nakajima, A. Higurashi, S. Ohta, and N. Sugimoto (2003), Aerosol distributions and radiative forcing over the Asian-Pacific region simulated by Spectral Radiation-Transport Model for Aerosol Species (SPRINTARS). *J. Geophys. Res.*, *108*(D23), 8659, doi:10.1029/2002JD003210.

Tanré, D., M. Herman, and Y. J. Kaufman (1996), Information on aerosol size distribution contained in solar reflected spectral radiances, *J.Geophys.Res., 101*(D14), 19,043-19,060.

Tanré, D., Y. J. Kaufman, M. Herman, and S. Mattoo (1997), Remote sensing of aerosol properties over oceans using the MODIS/EOS spectral radiances, *J. Geophy. Res.*, *102,* 16,971-16,988.

Tarpley, J. D. (1979), Estimating incident solar radiation at the surface from geostationary satellite data, *J. Appl. Meteor. 18:*1172-1181.

Tegen, I., P. Hollrig, M. Chin, I. Fung, D. Jacob, and J. Penner (1997), Contribution of different aerosol species to the global aerosol extinction optical thickness: Estimates from model results, *J. Geophys. Res. 102*, 23895-23915.

Tegen, I., and R.L. Miller (1998), A general circulation model study on the interannual variability of soil dust aerosol. *J. Geophys. Res. 103*, 25975-25995.

Torres, O., P. K. Bhartia, J. R. Herman, Z. Ahmad, and J. Gleason (1998), Derivation of aerosol properties from satellite measurements of backscattered ultraviolet radiation: Theoretical basis, *J. Geophy. Res.*, *103,* 17,099-17,110.

Torres, O., P. K. Bhartia, J. R. Herman, A. Sinyuk, P. Ginoux, and B. Holben (2002), A long-term record of aerosol optical depth from TOMS observations and comparison to ARONET measurements, *J. Atmos. Sci., 59*, 398-413.

Torres, O., R. Decae, P. Veefkind, and G. de Leeuw (2003), OMI aerosol retrieval algorithm, in *OMI Algorithms Theoretical Basis Document*, vol. 3, *Clouds, Aerosols and Surface UV Irradiance*, edited by P. Stammes, pp. 46–71, Neth. R. Meteorol. Inst., Utrecht.

Torres, O., P. K. Bhartia, A. Sinyuk, E. J. Welton, and B. Holben (2005), Total Ozone Mapping Spectrometer measurements of aerosol absorption from space: Comparison to SAFARI 2000 ground-based observations, *J. Geophys. Res.*, *110*, D10S18, doi:10.1029/2004JD004611.

Twomey, S.A. (1997), The Influence of Pollution on the Shortwave Albedo of Clouds, *J. Atmos. Sci.* 34, 1149-1152.

Valero, F. P. J., S. K. Pope, R. G. Ellingson, A. W. Strawa, and J. Vitko (1996), Determination of clear-sky radiative flux profiles, heating rates, and optical depths using unmanned aerospace vehicles as a platform, *J. Atmos. Oceanic Technol., 5*, 1024– 1030.

Van De Hulst, H. C. (1957), *Light Scattering by Small Particles*. Wiley, 414-418.

Van Dingenen, R., Virkkula A. O., Raes, F., Bates, T. S. and Wiedensohler, A. (2000), A simple non-linear analytical relationship between aerosol accumulation number and sub-micron volume, explaining their observed ratio in the clean and polluted marine boundary layer. *Tellus 52B*, 439–451.

Veefkind, J. P., G. de Leeuw, and P. A. Durkee (1998), Retrieval of aerosol optical depth over land using two-angle satellite radiometry during TARFOX, *Geophys. Res. Lett.*, 25, 3135– 3138.

Veefkind, J.P., G. de Leeuw, P.A. Durkee, P.B. Russell, P.V. Hobbs and J.M. Livingston (1999), Aerosol optical depth retrieval using ASTR-2 and AFHRR data during TARFOX, *J. Geophys. Res., 104*, 2253-2260.

Vinoj, V., S. S. Babu, S. K. Satheesh, K. K. Moorthy, and Y. J. Kaufman (2004), Radiative forcing by aerosols over the Bay of Bengal region derived from shipborne, island-based, and satellite (Moderate-Resolution Imaging Spectroradiometer) observations, *J. Geophys. Res.*, *109*, D05203, doi:10.1029/2003JD004329.

Voss, K. J., E. J. Welton, P. K. Quinn, R. Frouin, M. Miller, and R. M. Reynolds (2001a), Aerosol Optical Depth measurements during the Aerosols99 experiment. *J. Geophys. Res.*, *106*(D18), 20811 – 20820.

Voss, K. J., E. J. Welton, P. K. Quinn, J. Johnson, A. Thompson, and H. R. Gordon (2001b), Lidar measurements during Aerosols99, *J. Geophys. Res., 106*(D18), 20821–20832.

Wallace, J. M., C. Smith, and C. S. Bretherton (1992), Singular value decomposition of wintertime sea surface temperature and 500-mp height anomalies, *J. Clim., 5,* 561-576.

Wandinger U., D. Mu¨ller, C. Bo¨ckmann, D. Althausen, V. Matthias, J. Bo¨senberg, V. Weiß, M. Fiebig, M. Wendisch, A. Stohl, and A. Ansmann (2002), Optical and microphysical characterization of biomass-burning and industrial-pollution

aerosols from multiwavelength lidar and aircraft measurements, *J. Geophys. Res.*, *107*(D21), 8125, doi:10.1029/2000JD000202.
Wang, H., and M. F. Ting (2000), Covariability of winter U.S. precipitation and Pacific Sea surface temperatures, *J. Clim., 15*, 3711-3719.
Wang, J., S. A. Christopher, J. S. Reid, H. Maring, D. Savoie, B. N. Holben, J. M. Livingston, P. B. Russell, and S.-K. Yang (2003a), GOES 8 retrieval of dust aerosol optical thickness over the Atlantic Ocean during PRIDE, *J. Geophys. Res., 108*(D19), 8595, doi:10.1029/2002JD002494.
Wang, J., S. A. Christopher, F. Brechtel, J. Kim, B. Schmid, J. Redemann, P. B. Russell, P. Quinn, and B. N. Holben (2003b), Geostationary satellite retrievals of aerosol optical thickness during ACE-Asia, *J. Geophys. Res.*, *108*(D23), 8657, doi:10.1029/2003JD003580.
Wanner, W., A. H. Strahler, B. Hu, P. Lewis, J.-P Muller, X. Li, C. Schaaf, and M. J. Barnsley (1997), Global retrieval of bidirectional reflectance and albedo over land from EOS MODIS and MISR data: Theory and algorithm, *J. Geophys. Res., 102*, 17143-17161.
WCP-55 (1983), Report of WMO (CAS)/Radiation commission of IAMAP meeting of experts on aerosols and their climatic effects. Williamsburg, VA, A. Deepak and H.E. Gerber, Eds., 107pp.
Welton, E. J., J. R. Campbell, J. D. Spinhirne, and V. S. Scott (2001), Global monitoring of clouds and aerosols using a network of micro-pulse lidar systems, in *Lidar Remote Sensing for Industry and Environmental Monitoring, U. N. Singh, T. Itabe, N. Sugimoto, (eds.), Proc. SPIE, 4153,* 151-158.
Wendling, P., et al. (2002), Aerosol–radiation interaction in the cloudless atmosphere during LACE 98, 2, Aerosol-induced solar irradiance changes determined from airborne pyranometer measurements and calculations, *J. Geophys. Res., 107*(D21), 8131, doi:10.1029/2000JD000288.
Wex, H., C. Neusuß, M. Wendisch, F. Stratmann, C. Koziar, A. Keil, A. Wiedensohler, and M. Ebert (2002), Particle scattering, backscattering, and absorption coefficients: An in situ closure and sensitivity study, *J. Geophys. Res., 107*(D21), 8122, doi:10.1029/2000JD000234.
Whitby K. T. (1978), The physical characteristics of sulphur aerosols. *Atmos. Environ.*, *12*, 135-159.
Whitby K. T. and B. Cantrell (1975), Atmospheric aerosols—characteristics and measurements, in *The International Conference on Environmental Sensing and Assessment, Las Vegas,Nevada, September 14–19,* Institute of Electrical and Electronics Engineers, New York.
Whitlock, C. H., T. P. Charlock, W. F. Staylor, R. T. Pinker, I. Laszlo, A. Ohmura, H. Gilgen, T. Konzelman, R. C. DiPasquale, C. D. Moats, S. R. LeCroy and N. A. Ritchey (1995), First Global WCRP Shortwave surface Radiation Budget Data Set, *Bull. Amer. Meteor. Soc., 76, No. 6,* 905-922.
Wielicki, B.A., B.R. Barkstrom, E.F. Harrison, R.B. Lee III, G.L. Smith, and J.E. Cooper, (1996), Clouds and the Earth's Radiant Energy System (CERES): An Earth Ob-serving System Experiment. *Bull. Amer. Meteor. Soc., 77*, 853-868.
Winker, D., J. Pelon, and M. P. McCormick (2002), The CALIPSO mission: Aerosol and cloud observations from space, in *21th International Lidar Radar*

Conference, pp. 735– 738, Int. Coord., Gr. on Laser Atmos. Stud., Québec, 8 – 10 July 2002.

Wiscombe, W. and G. Grams (1976), The backscattered fraction in Two-Stream Approximations. *J. Atmos. Sci.*, *33*, 2440-2451.

Wood, R., Johnson, D., Osborne, S., Andreae, M. O., Bandy, B., Bates, T. S., O'Dowd, C., Glantz, P., Noone, K., Quinn, P., Rudolph, J. and Suhre, K. (2000), Boundary layer and aerosol evolution duringthe Lagrangian experiment of ACE-2. *Tellus 52B*, 401–422.

Xie, P. and P. A. Arkin (1996), Analyses of global monthly precipitation using gauge observations, satellite estimates and numerical model predictions. *J. Climate, 9*, 840-858.

Yu, H., R. E. Dickinson, M. Chin, Y. J. Kaufman, M. Zhou, L. Zhou, Y. Tian, O. Dubovik, and B. N. Holben (2004), The direct radiative effect of aerosols as determined from a combination of MODIS retrievals and GOCART simulations, *J. Geophys. Res.*, 109, D03206, doi:10.1029/2003JD003914.

Yu, H., Y. J. Kaufman, M. Chin, G. Feingold, L. A. Remer, T. L. Anderson, Y. Balkanski, N. Bellouin, O. Boucher, S. Christopher, P. DeCola, R. Kahn, D. Koch, N. Loeb, M. S. Reddy, M. Schulz, T. Takemura, M. Zhou (2005) A review of measurement-based assessment of aerosol direct radiative effect and forcing, *Atmos. Chem. Phys.*, *5*, 7647-7768.